VILNIUS UNIVERSITY

CENTER FOR PHYSICAL SCIENCES AND TECHNOLOGY

Aurimas Uleckas

CONTACTLESS SPECTROSCOPY OF NATIVE AND TECHNOLOGICAL DEFECTS IN Si, Ge, AND GaN STRUCTURES

Doctoral dissertation

Technological Sciences, Material Engineering (08T)

Vilnius, 2012

Doctoral dissertation was prepared during period of 2008–2012 years at Vilnius University Faculty of Physics and Institute of Applied Research.

Supervisor:

Dr. Sc. Eugenijus Gaubas (Vilnius University, Technological Sciences, Material Engineering – 08 T).

VILNIAUS UNIVERSITETAS

FIZINIŲ IR TECHNOLOGIJOS MOKSLŲ CENTRAS

Aurimas Uleckas

NESĄLYTINĖ SAVITŲJŲ IR TECHNOLOGINIŲ DEFEKTŲ SPEKTROSKOPIJA Si, Ge IR GaN DARINIUOSE

Daktaro disertacija

Technologijos mokslai, medžiagų inžinerija (08T)

Vilnius, 2012

Disertacija rengta 2008 – 2012 metais Vilniaus universiteto, Fizikos fakulteto ir Taikomųjų mokslų institute.

Mokslinis vadovas:
habil. dr. Eugenijus Gaubas (Vilniaus universitetas, technologijos mokslai, medžiagų inžinerija – 08T).

Acknowledgements

I would like to express my great appreciation to supervisor Dr. Sc. E. Gaubas for involving me into scientific work and considerable influence on my evolution.

I am grateful to Prof. A. F. Orliukas and Dr. R. Aleksiejūnas for a careful pre-examination of this thesis and valuable suggestions in improving of the manuscript.

I would like to thank to all the members of our laboratory for creative and friendly atmosphere, especially to T. Čeponis for fruitful and harmonious cooperation.

Finally, I would like to thank my parents and friends for their permanent support throughout my studies.

This work was supported by the Lithuanian State Science and Studies Foundation.

Contents

I. Introduction

Research problem. Electrically active defects are one of the main obstacles to produce high efficiency semiconductor based devices. Deep levels determine the non-radiative recombination processes and deteriorate efficiency of light emitting diodes, charge collection efficiency of radiation detectors and determine high power dissipation of the power devices. Technology of complementary metal-oxide-semiconductor based on shrinking of the geometrical parameters is facing with fundamental limits of the silicon properties. An integration material with different lattice constant is a new trend for Si based technology development. The necessity of materials with higher dielectric constant to replace SiO_2 as gate insulator [1] implies opportunity to incorporate semiconductors with higher carrier mobility, such as Ge, on Si wafers. Generation of misfit and unwanted threading dislocations is inevitable while growing materials with different lattice constant one on the other. Different attempts to improve the quality of Ge layers on Si had been done, such as: thermal cyclic annealing [2], structured substrate application for defects trapping [3], or nano-heteroepitaxy, where partial elastic relaxation of Si substrate is achieved by the preparation of sufficiently small and high Si island structures [4].

Dislocations network also plays an essential role in performance of GaN based optoelectronic and electronic devices. GaN and III-V compounds related wide band-gap semiconductors are usually grown on sapphire or on silicon carbide substrates, therefore threading, edge and screw dislocations are hardly avoidable due to mismatch of materials lattices and thermal coefficients [5]. The same problem is facing while integrating GaN on Si substrates, therefore complex buffer layers as $Sc_2O_3/Y_2O_3/Si$ are exploited [6]. Dislocations introduce electronic states in forbidden energy gap and act as the non-radiative recombination or charge trapping centres which deteriorate parameters such as luminescence efficiency or breakdown voltage of the devices [7]. Therefore,

identification of the defects is essential to develop and to modify the conditions of layers growth and to improve the quality of these layers.

Semiconductor radiation detectors are widely applied in Large Hadron Collider (LHC) experiments for detection and tracking of particles. Standard Si based *pin* diodes operate reliably at fluences < 10^{15} particle/cm^2, while detector hardness up to fluences of >10^{16} cm^{-2} is required for the up-grade of LHC. Density of the defects increases together with irradiation fluence, and this determines degradation of the main detector parameters, as a diminishing of charge collection efficiency and increasing of leakage current. Several technologies are employed to improve radiation tolerance of Si sensors, namely the material growth, doping, defects engineering and device structure engineering [8]. Magnetic Czochralski grown silicon (MCz) is a promising material relatively to other traditional Cz and float zone (FZ) Si materials for high energy physics applications. Introduction of isovalent Ge atoms into Si material can be a promising technique for suppression of radiation defects formation. Radius of the Ge atom is larger comparing with Si, therefore incorporation of Ge atoms into Si lattice induces the elastic strains which are released by capturing vacancies [9]. Also development of material fabrication technology provides possibility to apply the wide band-gap materials like diamond, GaN and SiC, with attractive features such as low leakage current, excellent mechanical characteristics for radiation hard environment [10].

Conventional Si based detectors with thickness of the base region ~300 μm maintain ~10^{15} cm^{-2} irradiation fluence, however the charge collection efficiency drastically decreases due to large radiation defects concentration [11]. 3D Si detectors have been developed to decrease carrier drift length and at the same time sustain rather large detector thickness. 3D detectors consist of periodically arranged vertical n^+ and p^+ electrode columns through the entire detector thickness with distance between electrodes of 20 – 50 μm. This technology allows reducing full depletion voltage, carrier drift distance, and at the same time ensures the high charge collection efficiency.

To improve understanding of the influence of modern material growth and doping techniques and to develop advanced modes in defects and device structure engineering, the deeper insight should be reached concerning introduction and interactions of defects. Also their role in modifications of the most important characteristics of material, as carrier recombination and transport parameters, should be better understood. To improve instrumentation of defects detection resolution, the contactless techniques for comprehensive characterization of defects containing materials are desirable, despite large variety of existing defects control methods. Deeper understanding is necessary in the fields of radiation defects creation, migration, evolution and transforms during irradiation in order to clarify their role in detector operation features. Development of new methods is desirable for advanced control of defects within material. The multifunctional instruments are required for fast contactless evaluation of the most important parameters characterizing defects and defects containing materials. The methodologies of combined and synchronous measurements may be a basis for advanced, fast and comprehensive evaluation of material characteristics in real time during device operating and processing of new device structures.

Objectives of research. The aim of this work is addressed to material science and development of new measurement technologies for defects characterization and identification within modern structures of Si, Ge and GaN by developing the non-destructive techniques.

The main objectives were concentrated on:

- development of contactless time resolved spectroscopy of deep levels at room temperature;
- development of microwave probed contactless technique and instrumentation for lateral and cross-sectional scans of carrier lifetime profiles within inhomogeneous and irradiated structures;

- the *in situ* control of recombination lifetime in Si structures during penetrative and stopped protons irradiation, and examination of evolution of radiation defects;
- separation and examination of recombination parameters attributed to different layers within strained thin-layered SiGe structures;
- study of doping, metal implantation and irradiation dependent characteristics in Ge structures;
- study of growth and radiation induced defects within epitaxial GaN structures.

Relevance and scientific novelty of these investigations consist of development of contactless time resolved techniques for deep levels spectroscopy. This technique has been approved for evaluation of defects parameters within irradiated Si and implanted Ge structures. The methodology and instrumentation for the *in situ* control of recombination parameters during irradiations by penetrative and stopped protons have been proposed, designed and approved. Evolution of densities and of species of the radiation defects during irradiation has been examined and models for fluence dependent variations of density of extended defects are proposed. An impact of dislocation networks ascribed disorder on recombination properties has been revealed within strained thin-layered SiGe structures and epitaxial GaN layers. The models for explanation of the interplay of defects in these structures have been proposed. The methodologies and experimental arrangements for the combined time and spectral resolved measurements, based on photo-ionization, photo-luminescence, free-carrier absorption and photoconductivity transient effects have been proposed and approved.

Practical importance. Fast and contactless time resolved spectroscopy techniques suitable for identification of deep levels parameters at room temperature have been designed. These techniques allow identifying of traps activation energy and of carrier recombination lifetime changes synchronously.

The instruments for contactless microwave probed photoconductivity transients direct control have been designed, fabricated and calibrated for monitoring of the material recombination characteristics within research laboratory and industrial facilities, for the evaluation of quality of the technological procedures. The remote measurement arrangements for the *in situ* control of radiation induced changes of the material and radiation detector characteristics have been proposed, designed, fabricated, approved and installed for operation within harsh areas of the tandem-type particle accelerators. The revealed linear dependence of carrier lifetime in silicon on penetrative hadrons irradiation fluence, irrespective of Si material growth technology and particles energy, is prospective to be applied for the design of Si based sensors for irradiation dosimetry.

Statements in defence. The main statements in defence of this thesis are as follows:

1. The linear dependence of carrier lifetime in silicon on penetrative hadrons irradiation fluence, irrespective of Si material growth technology and particles energy, exists due to formation of extended radiation cluster-type defects, while point radiation defects are responsible for carrier trapping lifetime temperature and anneal dependent variations.
2. The time and spectrum resolved contactless spectroscopy techniques based on synchronous measurements of photo-ionization cross-section and photo-emitted carrier lifetime probed by microwave detected photoconductivity transients is a sensitive tool, approved on Si and Ge materials, for identification of deep levels associated with technological and radiation defects within temperature scale close to device operation environment.
3. The measurement arrangement implemented by using the designed portable instruments for carrier recombination lifetime remote monitoring during irradiation by hadrons allows controlling of

radiation defects creation and evolution in Si materials and particle detectors.

4. The dislocation networks ascribed disorder formed during growth and technological processing of Si-Ge and GaN thin layers leads to multi-componential carrier decay transients. Fast initial decay correlate with duration of photo-emission processes due to irradiative recombination within micro-crystalline volumes of GaN and asymptotic stretched-exponential carrier density relaxation constituent is determined by carrier trapping limited, random-walk type diffusion within dislocation-rich areas of material.

Author`s contribution. Over this study author performed contactless carrier lifetime measurements in Si, Ge, GaN and SiGe structures. Author contributed to creation of contactless measurement instrumentation for carrier lifetime lateral and in-depth profiling. The author participated in experiments of transient photoconductivity spectroscopy probed by microwaves and the *in situ* carrier lifetime measurements, which results are presented in this dissertation, as well. Author created software for data analysis and for the remote experiment control, implemented within *in situ* experiments. Author contributed in publication of results by preparing several drafts of manuscripts and by presenting the main results of dissertation at the GADEST, E-MRS, LNFK 36-39 conferences.

Mathematical description of the stretched–exponential decay due to the random-walk type trapping limited diffusion was derived by J. Kusakovskij. Steady-state GaN photoluminescence spectroscopy measurements were performed by dr. K. Kazlauskas and dr. J. Mickevicius. GaN samples of varying thickness were MOCVD grown by E. Jelmakas. All the investigations, data analysis and preparation of manuscripts were made under supervision of Dr. Sc. E. Gaubas.

The *in situ* experiments using tandem-type accelerators were performed at Helsinki University Accelerator Laboratory and at State Research Institute Center for Physical Sciences and Technology, Vilnius. The neutron irradiated Si *pin* detectors and wafer samples were prepared within CERN RD50 project, using Ljubljana TRIGA reactor. Irradiated detectors and wafers samples were provided by prof. J.Vaitkus, by dr. J.Harkonen and dr. E.Tuominen.

Publications. The main results of this study are published within 20 scientific articles [A1- A20] and the research results have been approved within 30 oral and poster presentations [P1-P30] at conferences.

Articles:

A1. E. Gaubas, P. Pobedinskas, J. Vaitkus, **A. Uleckas**, A. Žukauskas, A. Blue, M. Rahman, K.M. Smith, E. Aujol, B. Beaumont, J.-P. Faurie, and P. Gibart. *Defect attributed variations of the photoconductivity and photoluminescence in the HVPE and MOCVD as-grown and irradiated GaN structures.* Nuclear Instruments and Methods in Physics Research Section A **552** (2005) 82.

A2. E. Gaubas, A. Aleknavičius, M. Bauža, and **A. Uleckas**. *Excess carrier decay peculiarities caused by disorder in dislocation-rich SiGe and GaN layered structures.* Lithuanian Journal of Physics **45** (2005) 497.

A3. E. Gaubas, **A. Uleckas**, and E. Simoen. *Excess carrier dynamics in SiGe ultra-thin layers*. Lithuanian Journal of Physics **45** (2005) 377.

A4. E. Gaubas, M. Bauža, **A. Uleckas**, and J. Vanhellemont. *Carrier lifetime studies in Ge using microwave and infrared light techniques*. Materials Science in Semiconductor Processing **9** (2006) 781.

A5. M. Bauža, E. Gaubas, J. Vaitkus, **A. Uleckas**. *Carrier recombination and trapping characteristics in the heavy irradiated high resistivity silicon*. Proc. International conference "Radiation interaction with material and its use in technologies 2006", Kaunas (2006) 126.

A6. **A. Uleckas**, M. Bauža, E. Gaubas, J. Grant, K. Kazlauskas, and J. Vaitkus. *Recombination characteristics in the proton and neutron irradiated GaN structures*. Proc. International conference "Radiation interaction with material and its use in technologies 2006", Kaunas (2006) 228.

A7. E. Gaubas, **A. Uleckas**, J. Vanhellemont, and A. Theuwis. *Recombination peculiarities in doped Ge*. Lithuanian Journal of Physics **47** (2007) 303.

A8. E. Gaubas, **A. Uleckas**, and J. Vishniakov. *Dose dependent variations of carrier recombination in silicon irradiated by high energy electrons*. Lithuanian Journal of Physics **47** (2007) 457.

A9. E. Gaubas, A. Kadys, **A. Uleckas**, and J. Vaitkus. *Investigation of carrier recombination in Si heavily irradiated by neutrons*. Acta Phys. Polonica A **113** (2008) 829.

A10. E. Gaubas, **A. Uleckas**, R. Grigonis, V. Sirutkaitis, and J. Vanhellemont. *Microwave probed photoconductivity spectroscopy of deep levels in Ni doped Ge*. Applied Physics Letters **92** (2008) 222102.

A11. E. Gaubas, **A. Uleckas**, R. Grigonis, V. Sirutkaitis, and J. Vanhellemont. *Spectroscopy of metal related levels in Ge by transient infrared and microwave absorption techniques*. Materials Science and Engineering B **154-155** (2008) 172.

A12. E. Gaubas, **A. Uleckas**, J. Vanhellemont, and W. Geens. *Metal implants dependent carrier recombination characteristics in Ge*. Materials Science in Semiconductor Processing **11** Iss. 5-6 (2008) 291.

A13. E. Gaubas, **A. Uleckas**, J. Vanhellemont. *Pulsed photo-conductivity and carrier recombination lifetime spectroscopy of metal doped germanium*. Superlattices and Microstructures **45** Iss. 4-5 (2009) 256.

A14. E. Gaubas, **A. Uleckas**, and J. Vaitkus. *Spectroscopy of neutron irradiation induced deep levels in silicon by microwave probed photoconductivity transients*. Nuclear Instruments and Methods in Physics Research Section A **607** (2009) 92.

A15. E. Gaubas, T. Čeponis, **A. Uleckas**, and J. Vaitkus. *Anneal dependent variations of recombination and generation lifetime in neutron irradiated MCZ Si*. Nuclear Instruments and Methods in Physics Research Section A **612** (2010) 563.

A16. E. Gaubas, **A. Uleckas**, J. Vaitkus, J. Raisanen, and P. Tikkanen. *Instrumentation for the in situ control of carrier recombination characteristics during irradiation by protons*. Review of Scientific Instruments **81** (2010) 053303.

A17. E. Gaubas, T. Čeponis, **A. Uleckas**, J. Vaitkus, K. Žilinskas, V. Kovalevskij, M. Gaspariūnas, and V. Remeikis. *In situ analysis of the carrier lifetime in silicon during implantation of 1.5 MeV protons*. Lithuanian Journal of Physics **50** (2010) 427.

A18. **A. Uleckas**, E. Gaubas, T. Čeponis, K. Žilinskas, R. Grigonis, V.Sirutkaitis, and J. Vanhellemont. *Analysis of Auger recombination characteristics in high resistivity Si and Ge*. Solid State Phenomena **178-179** (2011) 427.

A19. **A. Uleckas**, E. Gaubas, J.M. Rafi, J. Chen, D. Yang, H. Ohyama, E. Simoen, and J. Vanhellemont. *Carrier lifetime studies in diode structures on Si substrates with and without Ge doping*. Solid State Phenomena **178-179** (2011) 347.

A20. E. Gaubas, **A. Uleckas**, J.M. Rafi, J. Chen, D. Yang, and J. Vanhellemont. *Study of irradiation induced changes of electrical and functional characteristics in Ge doped Si diodes*. Physica B **407** (2012) 2998.

Articles **which results are not included** in the dissertation:

A21. E. Gaubas, T. Čeponis, D. Šalucha, I. Šimkienė, **A. Uleckas**. *Characteristics of surface recombination in silicon diode isolation grooves*. Lithuanian Journal of Physics **47** (2007) 461.

A22. J. Višniakov, E. Gaubas, T. Čeponis, **A. Uleckas**, J. Raisanen, and S. Vayrynen. *Comparative investigation of recombination characteristics in*

proton and electron irradiated Si structures. Lithuanian Journal of Physics **48** (2008) 137.

A23. J. Višniakov, T. Čeponis, E. Gaubas, and **A. Uleckas**. *Anneal-induced variations of the recombination characteristics in 2 MeV proton irradiated Si structures*. Lithuanian Journal of Physics **48** (2008) 325.

A24. J. Višniakov, T. Čeponis, E. Gaubas, and **A. Uleckas**. *Study of recombination characteristics in 2 MeV protons irradiated and annealed Si structures.* Nuclear Instruments and Methods in Physics Research Section A **607** (2009) 95.

A25. E. Gaubas, T. Čeponis, **A. Uleckas**, J. Vaitkus, and J. Raisanen. *Recombination characteristics in 2–3 MeV protons irradiated FZ Si*. Nuclear Instruments and Methods in Physics Research Section A **612** (2010) 559.

A26. **A. Uleckas**, T. Čeponis, A. Dzimidavičius, E. Gaubas, J. Pavlovas, and K. Žilinskas. *Investigation of the switching and carrier recombination characteristics in the proton irradiated and thermally annealed Si PIN diodes*. Lithuanian Journal of Physics **50** (2010) 225.

A27. E. Gaubas, T. Čeponis, S. Sakalauskas, **A. Uleckas**, and A. Velička. *Fluence dependent variations of barrier charging and generation currents in neutron and proton irradiated Si particle detectors*. Lithuanian Journal of Physics **51** (2011) 227.

A28. T. Čeponis, E. Gaubas, V. Kalendra, **A. Uleckas**, J. Vaitkus, K. Žilinskas, V. Kovalevskij, M. Gaspariūnas, and V. Remeikis. *In situ analysis of carrier lifetime and barrier capacitance variations in silicon during 1.5 MeV protons implantation*. Journal of Instrumentation **6** (2011) P09002.

A29. E. Gaubas, T. Čeponis, J. Kusakovskij, and **A. Uleckas**. *Barrier evaluation by linearly increasing voltage technique applied to Si solar cells and irradiated pin diodes*. ISRN Materials Science (2012) ID 543790.

A30. E. Gaubas, T. Čeponis, **A. Uleckas**, and R. Grigonis. *Room temperature spectroscopy of deep levels in junction structures using barrier capacitance charging current transients*. Journal of Instrumentation **7** (2012) P01003.

Presentations at conferences:

P1. E. Gaubas, **A. Uleckas**. *Excess carrier dynamics in SiGe ultra-thin layers*. Lithuanian National Conference of Physics 36, Vilnius, 2005.

P2. E. Gaubas, A. Aleknavičius, M. Bauža, **A. Uleckas**. *Excess carrier decay peculiarities caused by disorder in dislocation-rich SiGe and GaN layered structure*. Lithuanian National Conference of Physics 36, Vilnius, 2005

P3. **A. Uleckas**, M. Bauža, E. Gaubas, J. Grant, K. Kazlauskas, J. Vaitkus. *Recombination characteristics in the proton and neutron irradiated GaN structures*. International conference "Radiation interaction with material and its use in technologies", Kaunas, 2006.

P4. E. Gaubas, M. Bauža, **A. Uleckas**, J. Vanhellemont. *Cartier lifetime studies in Ge using microwave and infrared light techniques*. The European Materials Research Society (E-MRS) 2006.

P5. E. Gaubas, A. Kadys, **A. Uleckas**, J. Vaitkus. *Investigation of carrier recombination in Si heavily irradiated by neutrons*. 13th the International Symposium on Ultrafast Phenomena in Semiconductors, 2007.

P6. E. Gaubas, D. Šalucha, T. Čeponis, I. Šimkienė, **A. Uleckas**. *Characteristics of surface recombination in silicon diode isolation grooves*. Lithuanian National Conference of Physics 37, Vilnius, 2007.

P7. E. Gaubas, **A. Uleckas**, J. Višniakov. *Electron irradiation induced variations of recombination parameters in silicon*. Lithuanian National Conference of Physics 37, Vilnius, 2007.

P8. E. Gaubas, **A. Uleckas**, J. Vanhellemont, A. Theuwis. *Recombination peculiarities in doped Ge*. Lithuanian National Conference of Physics 37, Vilnius, 2007.

P9. E. Gaubas, J. Vaitkus, T. Čeponis, **A. Uleckas**, J.Raisanen, S. Vayrynen, E. Fretwurst. *Fluence dependent recombination lifetime in neutron and proton irradiated MCz, FZ and epi-Si structures*. 11th CERN RD50 Workshop, Geneva, 2007.

P10. E. Gaubas, A. Kadys, **A. Uleckas**, J. Vaitkus. *Investigation of fluence-dependent lifetime variations in proton and neutron highly irradiated Si*. 10th CERN RD50 Workshop, Vilnius, 2007.

P11. E. Gaubas, A. Kadys, **A. Uleckas**, J. Vaitkus. *Fluence-dependent lifetime variations in neutron irradiated MCZ Si measured by microwave probed photoconductivity and dynamic grating techniques*. 2nd Workshop of Defects Analysis in Silicon Detectors, Vilnius, 2007.

P12. E. Gaubas, **A. Uleckas**, R. Grigonis, V. Sirutkaitis, J. Vanhellemont. *Spectroscopy of metal related levels in Ge by transient infrared and microwave techniques*. The European Materials Research Society (E-MRS) 2008.

P13. E. Gaubas, **A. Uleckas**, J. Vanhellemont, W. Geens. *Metal implants dependent carrier recombination characteristics in Ge*. The European Materials Research Society (E-MRS) 2008.

P14. E. Gaubas, J. Vaitkus, T. Čeponis, **A. Uleckas**, E. Fretwurst, G. Lindstrom. *Fluence dependent variations of recombination and deep level spectral characteristics in neutron and proton irradiated MCz, FZ and epi-Si structures*. 3rd Workshop of Defects Analysis in Silicon Detectors, Hamburg, 2008.

P15. J. Vaitkus, T. Čeponis, E. Gaubas, **A. Uleckas**, J. Višniakov, J. Raisanen. *Fluence and isochronal anneal dependent variations of recombination and DLTS characteristics in neutron and proton irradiated MCz, FZ and epi-Si structures*. 12th CERN RD50 Workshop, Ljubljana, 2008.

P16. E. Gaubas, **A. Uleckas**, J.V. Vaitkus. *Spectroscopy of neutron irradiation induced deep levels in silicon by microwave probed photoconductivity*. 10th International Workshop on Radiation Imaging Detectors, Helsinki, Finland, 2008.

P17. E. Gaubas, **A. Uleckas**, J. Vanhellemont. *Pulsed photo-conductivity and carrier recombination lifetime spectroscopy of metal doped germanium*. 9th International Workshop on Beam Injection Assessment of Microstructure in Semiconductors, Toledo, Spain, 2009.

P18. **A. Uleckas**, T. Čeponis, E.Gaubas, K. Žilinskas. *Peculiarities of carrier recombination and transport in neutron irradiated Si particle detectors*. Lithuanian National Conference of Physics 38, Vilnius, 2009.

P19. E. Gaubas, **A. Uleckas**, J.V. Vaitkus, J. Raisanen. *Evolution of radiation defects during protons irradiation.* Lithuanian National Conference of Physics 38, Vilnius, 2009.

P20. **A. Uleckas**, E. Gaubas, T. Čeponis, and A. Balčytis. *In situ study of carriers recombination characteristics during proton irradiation*. International conference "Radiation interaction with material and its use in technologies", Kaunas, 2010.

P21**. A. Uleckas**, E. Gaubas, J. Vaitkus, and T. Čeponis. *In situ control of carrier trap characteristics in Si structures during irradiation by penetrative protons.* 12th International Conference-School "Advanced materials and technologies", Palanga, 2010.

P22. E. Gaubas, T. Čeponis, **A. Uleckas**, S. Sakalauskas, and J.V. Vaitkus. *Evaluation of fluence dependent variations of capacitance and generation current parameters by transient technique*. 16th CERN RD50 Workshop, Barcelona, 2010.

P23. E. Gaubas, T. Čeponis, **A. Uleckas**, J.V. Vaitkus, E. Žąsinas, and J.Raisanen. *Study of dominant recombination defects by fluence dependent variations of carrier lifetimes and drift parameters in MCZ Si*. 16th CERN RD50 Workshop, Barcelona, 2010.

P24. **A. Uleckas**, E. Gaubas, T.Čeponis, K. Žilinskas, R. Grigonis, V.Sirutkaitis, and J. Vanhellemont. *Analysis of Auger Recombination Characteristics in High Resistivity Si and Ge*. Gettering and Defect Engineering in Semiconductor Technology, Austria, 2011.

P25. **A. Uleckas**, E. Gaubas, J.M. Rafi, J. Chen, D. Yang, H. Ohyama, E. Simoen, and J. Vanhellemont. *Carrier Lifetime Studies in Diode Structures on Si Substrates with and without Ge Doping*. Gettering and Defect Engineering in Semiconductor Technology, Austria, 2011.

P26. E. Gaubas, **A. Uleckas**, J.M. Rafi, J. Chen, D. Yang, and J. Vanhellemont. *Study of irradiation induced changes of electrical and functional characteristics in Ge doped Si diodes*. 26th International conference on defects in semiconductors, New Zealand, 2011.

P27. **A. Uleckas**, E. Gaubas, T. Čeponis, and R. Grigonis. *Generation current and photoconductivity spectroscopy in Si pin diodes by employing barrier capacitance probing technique*. 13th International Conference-School "Advanced materials and technologies", Palanga, 2011.

P28. **A. Uleckas**, E. Gaubas, T. Čeponis, A. Tekorius, V. Kovalevskij, V. Remeikis. *Analysis of barrier charging current variations in Si particle detectors during 1.5 MeV proton irradiation*. Lithuanian National Conference of Physics 39, Vilnius, 2011.

P29. A. Velička, T. Čeponis, E. Gaubas, **A. Uleckas**, A. Tekorius. *Investigation of the technological defects anneal in Si thyristor structures by capacitance and deep level spectroscopy techniques*. Lithuanian National Conference of Physics 39, Vilnius, 2011.

P30. E. Gaubas, J. Vaitkus, T. Čeponis, **A. Uleckas**, *Prototype instrument for fluence monitoring based on carrier lifetime control by microwave probed photoconductivity transients*. AIDA 1st Annual Meeting, DESY, Hamburg, 2012.

Structure of dissertation. The dissertation consists of eight chapters as introduction, survey on common experimental techniques, description of principles of the developed techniques, results and analysis of the time resolved photo-ionization spectroscopy of Si and Ge materials, examination of lifetime variations in SiGe structures, spectroscopy of radiation defects in Si, defect evolution study during irradiations, doping and implantation dependent carrier lifetime variations in Ge structures, growth and irradiation induced changes of carrier recombination characteristics in GaN epi-layers. Description is concluded by summary of the main results. List of references is provided at the end of the dissertation.

II. Survey on techniques for characterization of defects

Identification of the defects in semiconductor materials and evaluation of their parameters is one of the main subjects which are closely related with progress in technology development. There is a huge variety of techniques to explore microscopic and macroscopic characteristics of the defects. Electrical and optical properties of the materials are determined by existence of the native and technological defects, therefore non-invasion and contact methods are combined for defects characterization. Electrodes or even structure of the *p-n* junction are required in order to apply contact methods. Unfortunately additional contamination could be introduced into the material during contacts formation process. As a result contactless methods are preferable to observe defects during technological processes of structures formation as well as for evaluation of the electrical and optical parameters of new materials. Mean while observation of the defects in the finished device structures is usually performed employing contact techniques which are more sensitive comparing with non-invasive methods.

2.1. Contact techniques for defects spectroscopy and profiling

Deep level transient spectroscopy (DLTS) is a standard method based on measurements of variations of capacitance transients with temperature, when depletion width of a diode is harmonically modulated by external test voltage [12]. Capacitance of a diode depends on doping concentration (N_d), on density of deep levels (N_t) and on occupancy of traps by carriers (n_t) for donor like majority carrier traps.

Emission rate of carriers from the trap depends on temperature, deep level activation energy and capture cross-section ($\sigma_{p,n}$), and it is expressed as – $e_{p,n}(T)=\gamma_{p,n}T^2\sigma_{p,n}exp[\pm(E_t-E_{c,v})/kT]$ for holes and electrons, respectively. Parameters of majority and minority carrier traps could be evaluated in *p-n* diode structures varying initial condition i.e. applying reverse or forward voltage. Minority carrier traps could be filled in *p-n* structures by forward

voltage, while optical injection of minority carriers is necessary in Schottky diodes. Capacitance transients of a diode could then be determined. Taking into account that one process (carrier capture or emission) is dominated and approach of small defect concentration relatively to dopants ($N_d >> N_t, n_t$) should be maintained, for simple analysis of DLTS transients and capacitance changes. Then proper regimes for registration of thermal emission rates are arranged.

Measurements of capacitance variation transients enable one to evaluate thermal emission rate and to extract deep level activation energy, values of capture cross-section and of density of the deep levels. The lower limit of the detectable traps concentration is determined by capacitance bridge sensitivity when density of traps is lower comparing with doping concentration by four orders of magnitude. Evaluation of electrically active defects in highly compensated semiconductors, where density of the trapping centres is comparable to dopants concentration ($N_t \approx N_d$), is difficult. Shallow trap levels can not be identified due to freeze out of free carriers, when the junction barrier capacitance of a diode falls down to its geometrical value. Carrier emission from the deep level with relatively high concentration results in a non-exponential capacitance transient, and this reason significantly changes the free carrier concentration. Also, evaluation of the parameters of deep levels by using conventional DLTS arrangement for the wide band-gap materials, where thermal emission from deep levels is small in experimentally available temperature range, is complicated [13, 14]. Therefore deep level optical spectroscopy (DLOS) could be applied for evaluation of trap activation energy by photo-ionization spectroscopy techniques [13, 15]. The techniques based on photocurrent measurements are then suitable for deep levels detection, as well. However, evaluation of traps concentration, by using dc photoconductivity spectroscopy regimes, is difficult, as the dc photocurrent is a complex function of the optical emission rate and the carrier population in the deep levels [16].

Capacitance techniques are employed for profiling of the electrically active defects. Distribution of electrically active defects within the depletion width can be evaluated by varying bias voltage. Double correlated deep level transient spectroscopy (DDLTS) based on applying two bias voltage pulses with different amplitudes, instead of one employed in the standard C-DLTS. The DDLTS allows precisely control the depth-probing width [17]. Specific traps distribution profiles can be measured by stabilizing temperature at the particular DLTS peak and by varying bias voltage, to perform the scanning.

Temperature stimulated current technique (TSC) is based on measurements of current changes due to charge emission from the traps as a function of temperature, while heating sample at constant rate. TSC overcomes limiting factor of DLTS, requiring that traps concentration should be less comparing with dopants [18]. Therefore TSC is applied for spectroscopy of deep levels in highly irradiated semiconductors detectors [19]. For example, the reliable DLTS results could be obtained till $\approx 10^{13}$ cm^{-2} fluence of hadrons irradiation, when dopants density of the detector base region is of 10^{12} cm^{-3}, and taking into account defects introduction rate of 0.01 cm^{-1} [20]. Therefore TSC technique is more applicable for research of radiation hardness of semiconductor detectors, when irradiation fluence reaches value of about 3×10^{16} cm^{-2} for CERN large hadron collider purposes. However, necessity of the large depletion voltage is a limiting factor for precise evaluation of traps concentration and activation energy. Also detection of deep levels is complicated at elevated temperatures due to increase of the intrinsic generation of carriers.

Recombination and generation lifetime in *p-n* structures can be evaluated by combining measurements of current-voltage (I-V) characteristics with capacitance-voltage (C-V) characteristics [21, 22]. However, the on-state I-V characteristics depend on minority carrier lifetime while leakage current is governed by carrier generation within depleted region of a diode base. Straightforward calculation of the lifetimes can yield a difference by several

orders of magnitude relatively to values measured by other techniques. This discrepancy is related to the high electric field and the shallow junction effect within the reverse and forward I-V characteristics, respectively [23]. To overcome this problem, the steady-state current-voltage characteristics are measured on diodes of different geometry. This allows separating the bulk current density and accurate evaluation of carrier lifetimes [23, 24]. The C-V measurements on diodes performed using LRC meters enable one to extract values of doping concentration and of full depletion voltage of detectors. But measurements of C-V characteristics become complicated in heavily irradiated detectors, when defects concentration is large [25]. Reliable capacitance measurement can be implemented when quality factor (Q) is higher than 5, otherwise capacitance values in parallel and serial modes (C_p, C_s) are different. The quality factor might be small due to large conductance and serial resistance. The decrease of Q in heavily irradiated diodes is related with radiation induced traps which are responsible for generation current within the depletion region. Barrier evaluation by linearly increasing voltage technique (BELIV) enables to separate and to extract the components of barrier charging current and of generation current. Experiments applying this technique revealed that the barrier capacitance decreases with enhancement of irradiation fluence and the leakage current component dominates within BELIV transients for fluence values above 10^{16} proton/cm^2 [26]. Symmetrical forward and reverse current branches within I-V characteristics as well as small values of barrier capacitance indicate that a diode after heavy irradiations behaves like a poor resistor.

Semiconductor device performance strongly depends on the distribution of carriers and defects within the device structure, therefore profiling of these quantities is desirable. Spreading resistance measurements allow analyzing distribution of the carriers within depth of semiconductor layered structures. Concentration of the carriers varying up to ten orders of magnitude can be evaluated from the resistivity profiling measurements [27, 28]. Capacitance

scanning microscopy is a surface probing technique when capacitance between the surface and the probe is measured. Capacitance signal is modulated periodically by the tip-probe motion within the atomic force microscopy [29]. The latter technique is sensitive to charge variation on the sample and, thus charge profiles can be mapped with 10 nm spatial resolution [30]. Spreading resistance measurements are widely applied for dopants profiling in semiconductor devices as well as for quantum structure investigations. Alternative method for evaluation of the elemental composition of the structures is secondary ion mass spectrometry (SIMS). While spreading resistance is limited to silicon, germanium and a few other semiconductors, SIMS can be implemented for profiling of the atomic concentration almost without any restrictions for materials. SIMS technique is applicable for spatial resolution of ultra-shallow depth-profiles (< 0.1 micrometre), while spreading resistance technique is more convenient for deeper profiling of layered structures.

DLTS, TSC, I-V, C-V and other techniques based on capacitance or current measurements allow evaluating only integral parameters of the electrical active traps. Therefore microscopic techniques such as EPR, FTIR and Raman spectroscopy, which are sensitive to the defects of crystal lattice, are desirable to comprehensively examine the microscopic structure and symmetry of the defects for identification the nature of defects.

2.2. Contactless techniques for spectroscopy of the deep traps

Vibrational modes are as a finger print of each defect in the crystal lattice. Infrared absorption technique is devoted for identification of defects structure and symmetry. More sensitive and containing the higher spectral resolution is a Fourier transform infrared spectroscopy (FTIR). Contrary to electrical methods, FTIR is sensitive to both the electrically active and non-active defects. However, the lowest detectable density exceeds that of measured using contact methods by several orders of magnitude [31]. Nevertheless, spectroscopy of local vibrational modes plays important role among the large number of

semiconductor characterization techniques. This technique allows, in many cases, the precise identification of impurity species and their location within crystal lattice cells with rather high sensitivity. Also, FTIR spectroscopy, applied together with manipulation of other external factors such as polarization of the probe light, hydrostatic stress, and isotope substitution, is successfully employed for identifying of the structure and composition of various species of defect complexes [32].

Electron paramagnetic resonance spectroscopy is a technique for studying defects that have one or more unpaired electrons, such as transition metals impurities, vacancies and complex defects. The other requirement is that static magnetic field and a microwave field can penetrate into the crystal in order to induce magnetic resonance transitions. Therefore only non-metallic crystals and low conductivity semiconductors can be investigated by EPR. Symmetry of defects is identified using variations of EPR lines with rotating magnetic field within any of the crystal plane [33]. Electron paramagnetic resonance effect can be observed by measuring optical absorption or emission from bands of the defects. This EPR regime is based on EPR signal changes due to optical absorption or optical emission from bands of the defects [34].

A positron annihilation lifetime spectroscopy is a sensitive tool for detection of vacancy related defects in materials containing extended void type defects [35]. Positron annihilation time in bulk silicon depending on sample conductivity is ~218 ps, while lifetime of the positrons increases to 270 – 275 ps when positrons are trapped at neutral mono-vacancy. Positron annihilation spectroscopy is desirable technique for clusters identification is silicon. The theoretical evaluations show that positron lifetime is expressed as $\tau(n)= 220+230[1-exp(-n/5)]$ for the most compact clusters, containing n vacancies, while this lifetime is predicted to be independent of n for the linear vacancy chains [36].

Photoluminescence spectroscopy (PL) can be also applied to detect impurities which are involved into radiative recombination. Time resolved PL

spectroscopy enable to extract and to evaluate dynamic parameters of the carriers, when these measurements are performed at preferable PL peaks. PL spectroscopy is a powerful technique for investigation of quantum confinement effects, for characterization of defect complexes and for reveal of the peculiarities of carriers dynamic in the direct band-gap semiconductors. But this technique does not provide full information about excess carrier decay process in the material, therefore concerted measurements of time-resolved PL together with photoconductivity transients would give a more comprehensive understanding of carrier recombination mechanisms. Photoluminescence technique has been successfully applied for radiation defects investigation in silicon [37]. Only emission from the phosphorus donors above 1100 meV and a weak free-exciton emission have been detected in luminescence spectra of high purity silicon before Si irradiation by high energy protons. After irradiation, the high-energy photons luminescence spectrum wing is quenched, and broadband PL signal in the range from 750 to 1000 meV is observed [37], when additional weak *W* band emission at 1018 meV is detected. In the oxygenated Si samples, the carbon interstitials are trapped at oxygen forming *C* centres, those are responsible for PL at 789 meV while, for non-oxygenated Si material samples, the substitutional carbon is identified as *G* centre, exhibiting a PL spectral line at 969 meV. It should be mentioned that control of photoluminescence signals to identify defects and to control their density is only possible when the amplitude of the PL peaks is proportional to the concentration of the defects. It is possible that luminescence is quenched by divacancies which are produced by hadrons irradiation [37].

Semiconductor wafer surface flatness, homogeneity and cleanliness are essential requirement before performing technological operations for manufacturing of semiconductor devices or ultra-large-scale-integrated-circuits. Most Czochralski grown silicon for micro-electronics application contains a low density (of the order of 10^6 cm^{-3}) of about 150 nm octahedral voids which are formed by homogeneous precipitation of supersaturated lattice

vacancies during crystal growth [38]. Visible light scattering techniques can be used with great success to detect and to resolve surface defects on polished semiconductor wafers [39]. It was established that the ramp rate plays a key role in the formation of the ring-like structures of defects distribution. Dendrite-like islands containing N, O, Si, and traces of C were revealed in these structures. Formation of the precipitate rings strongly depends on the growing conditions and is a result of fast temperature ramping while on the Si wafers annealed at slow ramp conditions the ring like structures do not prevail [40]. Near infrared light scattering technique allows determining of bulk defect size distributions in Si and GaAs wafers [40]. While surface defects can be also detected by optical microscopy, SEM, AFM, or TEM techniques.

2.3. Contactless control of the defects determined dynamic characteristics

The widely employed light-induced dynamic grating technique is based on probing of grating decay kinetics at various grating periods. Interference pattern in the sample is created by two strongly absorbed laser beams which modulate free-carriers distribution $N(x) = N_0[1+\cos(2\pi x/\Lambda)]$ with the period Λ. The grating decay transient is probed by measuring the intensity of weakly absorbed beam [42, 41]. Kinetics of the grating decay at various grating periods provide values of the coefficient of ambipolar carrier diffusion D and of carrier lifetime τ_R according to the relationship $1/\tau_G = 1/\tau_R + 1/\tau_D$, where $\tau_D = \Lambda^2/4\pi^2 D$ is the diffusive grating decay time. Bimolecular recombination coefficient could be also evaluated performing measurements at different temperature and taking into account the diffusion coefficient temperature dependence [41]. Application of different wavelengths light for excess carrier generation makes it possible to vary the depth of the excited region. Thus diffusion and carrier recombination properties of the different layers can be evaluated [43]. Also this technique allows analysing variation of the ion implantation induced electrical parameters within near-surface thin layers. This regime is important for control the formation of the shallow junctions in

nanoscale electronic. Measurements of the diffraction efficiency variation with excitation density in GaAs with high density of the defects enable to reveal the screening effects [44]. The possibility to study material properties at high excitation conditions which are close to operation of lasing or power devices is especially attractive. The non-exponential/non-linear features of diffraction efficiency are inherent for these characteristics at high excitation condition. This behaviour might be a manifestation of the nonlinear effects in the sample, such as two-photon absorption, nonlinear refraction, saturation of absorption, and thermal effects. However, these non-linear effects should be clearly separated from the in-built non-linear behaviour of the diffraction characteristics for dynamic gratings.

Popular technique for the examination of the nonlinear properties is the so-called Z-scan, which allows evaluate magnitude of the higher order optical nonlinearities and to determine a sign of the nonlinear refraction index [45].

Evaluation of carrier recombination parameters is desirable within a broad interval of excess carrier densities to reveal prevailing traps for majority and minority carriers, to extract values of capture cross-section. Non-destructive techniques are highly attractive for controlling carrier lifetime values measured in between of technological procedures. There are several setups for measurements of quasi-steady-state (QSSPC) and transient (PCD) conductivity probing [39]. The QSSPC technique is based on sample conductivity probing with radio frequency range (RF) radiation after excess carrier modulation with flash lamp. Other technique is microwave detected photo-induced current transient spectroscopy (MD-PICTS) which is basically the same as microwave probed photoconductivity transient techniques, in literature known as μ-PCD. For implementation of latter technique, a semiconductor laser light modulated at the rate of 100 kHz is employed, and photoconductivity signal is recorded by using a conventional lock-in filtering technique [46]. However, long duration of excitation pulse is a limiting factor for a detail evaluation of excess carrier recombination processes when QSSPC and MD-PICTS techniques are applied.

Therefore examination of the two- or multi- componential carrier decay transients as well as measurements of short decay lifetimes, relatively to excitation pulse duration, are complicated. However, absorption or reflection of microwaves and of radio-frequency waves strongly depends on the sample conductivity. Therefore reflected photo-response signals can be saturated at high excitation conditions. Linearity of the signal can be controlled by monitoring the shape and the initial amplitude of the kinetics. However, these characteristics are complicated in quasi-steady-state excitation setup.

Summary of the chapter

Despite large variety of existing defects control methods, the contactless techniques for comprehensive characterization of defects containing materials are desirable.

The multifunctional instruments for contactless evaluation of the most important parameters characterizing defects and defects containing materials are also required to be developed, especially for evaluation of new materials and of advanced thin, as usually nano-scale, layered structures. Also, the portable instrumentation for remote and on-line control of defects production and for examination of their evolution within harsh areas of irradiations is necessary. Such instruments are also necessary for control of technological procedures based on irradiations.

The methodologies of combined and synchronous measurements may be a basis for advanced, fast and comprehensive evaluation of material characteristics within processing of new device structures and on-line during device operating. A few of the mentioned items comprise motivation of the aim and tasks for this research.

III. Principles of extraction of carrier recombination parameters

Carrier lifetime is one of the most important parameters in detection and evaluation of the structure of native and radiation induced defects within semiconductor materials, as this parameter is the most sensitive to changes of the electrical and recombination activity of defects. Examination of the carrier recombination/trapping characteristics unveil competition of recombination channels in redistribution of carrier capture flows, those determine electrical, optical and functional parameters of semiconductor materials and devices. Measurements of recombination characteristics by contact techniques is rather sensitive tool to reveal prevailing recombination defects, however, requirement of high quality of contacts is often limiting issue in precise evaluation of recombination parameters. Contactless techniques are free of such a problem of quality of electrodes, and these methods are preferential if detection sensitivity is sufficient. Most of contactless techniques are based on interaction of different probing radiations with a system of free carriers, decay of which is examined to extract carrier recombination parameters directly by measuring carrier decay rate. However, sensitivity of probing techniques depends on interaction (radiation-free carriers) cross-section, and the detectable signals are only obtained at high excitation levels for probing radiations with wavelengths in the range of far and near infrared light. For radio frequency (RF) wavelengths range, temporal resolution is insufficient to probe fast recombination events. Therefore, different probing radiations should be exploited to cover wide range of excitation levels and of carrier decay rates. Thus, principles of various probing regimes are discussed in this chapter to present basics of techniques designed in this work for analysis of recombination processes, determined by native and radiation induced carrier capture centres, and for profiling of defects distribution as well as for spectroscopy of defects activation energy.

3.1. Microwave probed photoconductivity transients at low excitation

Sensitivity of the microwave probing can be estimated by using an expression of the coefficient of free-carrier absorption $\alpha_0 = (4\pi/c)\sigma_{dc}$, with dc conductivity σ_{dc} independent of microwave (MW) frequency, estimated using Drude model [47] or quantum interaction models [48]. It have been proved [47] that values of α_0 significantly exceed those of $\alpha_{pl}(\omega_{pl})$ due to free carriers plasma ω_{pl} oscillations ascribed to $\alpha_{pl}(\omega_{pl})$ dispersion, i.e. $\alpha_0 >> \alpha_{pl}(\omega_{pl})$.

The latter dispersion ranges within near or middle infrared (IR) light frequencies spectrum. Thus, relatively large values of α_0 lead to limitations of a linear response of microwave absorption signals. The approaches of plane-waves [39, 48-51] or relations exploited in theory of microwaves propagation within waveguide systems, using reflection/transmission parameters, e.g. [52], are often employed for analysis of microwave response, modulated by photoexcited semiconductor, when different measurement regimes of external or intra-cavity sample mountings are applied, respectively.

For extra-cavity (relatively to waveguide) microwave probing regime, the response function (U) of the (MW) absorption by free carriers, is expressed as $U = k[I_p\ \Delta K - I_n]$, using the plane-waves approximation [49]. Here, I_p is intensity of the probe radiation, I_n – noise intensity, k – is the transfer function of MW to electrical signal, and ΔK – is conductivity dependent on MW transmission function. The steady-state transmission K is governed by the conductivity of material, wafer thickness and MW frequency. Thus the maximum amplitude of MW response is registered at local resonance condition, adjusted by slide short of MW bridge or frequency. The transient response of the light induced photoconductivity ($\Delta\sigma$) is determined by difference of the transmission functions for the dark $\sigma = \sigma_0$ and for photo-excited $\sigma = \sigma_0 + \Delta\sigma$ conditions, i.e. $\Delta K = K(\sigma_0) - K(\sigma_0 + \Delta\sigma)$. Linearity of the MW response is ensured just at $\Delta\sigma/\sigma_o << 1$ and $\Delta K/K << 1$ conditions, when ΔK is expressed as in [51]:

$$\Delta K = \frac{\Delta\sigma d\left[\sqrt{\frac{\mu_0}{\varepsilon_0}} + \frac{\mu_0}{2\varepsilon_0}\sigma_0 d + \frac{\mu_0}{4\varepsilon_0}\Delta\sigma d\right]}{\left[1+\left(\frac{1}{2}\sigma_0 d\sqrt{\frac{\mu_0}{\varepsilon_0}}\right)\right]^2\left[1+\left(\frac{1}{2}(\sigma_0+\Delta\sigma)d\sqrt{\frac{\mu_0}{\varepsilon_0}}\right)\right]^2} . \quad (3.1)$$

MW response function is proportional to conductivity ($U \sim \Delta\sigma \sim \Delta n$) and, thereby, to the excess carrier concentration, for low conductivity modulation conditions. While at high excitation levels, the amplitude of MW response deviates from linearity [51].

For extra-cavity microwave probing implementations, the photo-excited area of the sample under test is usually monitored by using antennas either of a slit made within waveguide wall or a needle-tip of the coaxial cable. Slit shape or coaxial needle-tip antenna operates as transmitter and receiver of reflected MW signals from the sample. The latter signal is transmitted to the MW detector through the same microwave waveguide, therefore circulator is installed to direct reflected MW signal towards the detector and to separate it from the MW generator chamber.

One of the promising tools for control of material properties with nano-scale resolution is near-field probing, based on detection of MW response signals of the material-radiation interaction when radiation wavelength λ significantly exceeds dimensions of an aperture of antennas D and of probing depth z, i.e. using regime of $\lambda >> D >> z$. Methods of the microwave near-field probing are the most prospective ones in characterization of the nanostructures [53], and these regimes are implemented in this work. Actually, the spatial resolution is additionally varied by excitation beam spot, as transient signal is only sensitive to the photo-induced conductivity changes.

Near field mode is realized, when slit or needle-tip antenna is exploited, as wavelengths of 10 – 26 GHz microwaves ($\lambda \sim 3 - 2.5$ cm) are much longer comparing with diameter of antenna tip (D) and distance between sample and antenna (z). The imaging resolution of a near-field microwave probing is typically governed by the probe smallest feature size such as a curvature of

needle-tip antenna. To take full advantage of small antenna sizes, the tip must be kept as close as possible to the sample surface in order to concentrate the electrical field of MW radiation, i.e. to achieve the highest resolution and strong signal, which decreases reciprocally to square function of distance ($1/z^2$). The reflection coefficient for the concentrated microwaves is expressed as in [54]

$$\Delta R = (G/2Z_0\sigma_0)(\Delta n(t)/n_0). \quad (3.2)$$

Here, G is a geometry factor, Z_0 – characteristic impedance of the microwave circuit, σ_0 is sample conductivity in the dark, n_0 is thermal equilibrium electron concentration and $\Delta n(t)$ is the photo-generated excess carrier concentration [54-56]. Thereby carrier lifetime planar variations of semiconductor wafer samples and of non-metallized device structures can be mapped with spatial resolution even better than geometrical size of slit and needle-tip antennas when G factor of probing system is of appropriate value.

To keep the linear response regime in all the microwave probing regimes, it is necessary to restrict excitation, and, thereby, the excess carrier concentration, at low conductivity modulation conditions:

$$\Delta \sigma/\sigma_0 \sim \Delta n(t)/n_0 < 1. \quad (3.3)$$

A schematic diagram of the experimental setup for implementation of the microwave probing measurements is illustrated in Fig. 3.1. Lasers with different wavelength and short pulses in the range of 10 ns to 40 fs are commonly applied for excess carrier generation. Microwaves of frequency of 10 – 22 GHz with power of 100 – 200 mW generated by Gunn oscillator serve as a probe source. Amplitude of MW response signal depends on quality factor (Q) of the whole microwave circuit together with the sample. Thus sample parameters as conductivity, thickness and structure are important for resonance conditioning [49, 51, 52]. Therefore, a MW adjustment system, by incorporating a MW bridge, is installed in order to achieve local resonance and to increase a ratio of the signal to noise, matched to samples of various equilibrium conductivity.

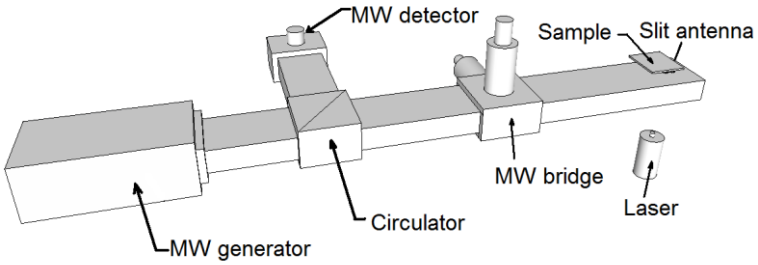

Fig. 3.1. Sketch of microwave probed photoconductivity transient setup.

Investigation of recombination parameters as function of excitation level, sample thickness, wavelength of excitation pulses and other external factors provide the opportunity for comprehensive investigation and detail consideration of the manifestation of several recombination centres at the same time. As a rule, recombination characteristics are nonlinear if several processes or complicated deep levels system manifest after excess carrier excitation. Therefore combined experiments are performed to minimize the number of uncertain parameters. Additional steady-state illumination is often employed to modify deep levels filling/emptying conditions when complex structure of deep levels system must be resolved. Measurements of the temperature dependent carrier lifetime variations enable spectroscopy of the activation energies of deep centres and identification of the defects. Then, carrier density variations caused by carrier capture/emission processes should be recognized and their parameters evaluated.

3.2. Free carrier absorption transients at high excitation levels

As mentioned, the cross-section $\kappa_{e\text{-}IR}$ of free carrier absorption $\alpha_{FC}=\kappa_{e\text{-}IR}n_e$ by infrared light (FCIRA) is decreased relatively to that α_0 for MW radiation. Values of this $\kappa_{e\text{-}IR}$ cross-section are in the range of $\kappa_{e\text{-}IR}\sim 10^{-18}$ cm^2, and densities of excess carriers n_e should be in the range of 10^{18} cm^{-3} to have detectable signals for examination of the free carrier absorption relaxation curves. For most moderately doped semiconductors ($n_{dop}\leq 10^{16}$ cm^{-3}), the

needed excess carrier densities to detect carrier decay transients lead to the high excitation level conditions: $n_e / n_{dop} >> 1$.

A linear relation between the measured FCIRA response and the time dependent changes in density of excess carriers $n_e(t)$ is essential to reveal peculiarities within a carrier decay transient caused by the non-linear recombination process. There are several obstacles to get this linear dependence. The limitations are caused by the nonlinearity of the FCIRA transfer function and the inhomogeneity of the initial distribution of excess carriers.

The FCIRA response is a differential signal that can be expressed as

$$\Delta I_{FC}(t) = k(1-R_{\lambda,pr})I_0 \exp(-\alpha_{\lambda,pr} d)(1-\exp(-\Delta\alpha_{FC}(t)d) \ , \qquad (3.4)$$

and, whereby, the time dependent changes of free carrier absorption for the probing light wavelength (λ_{pr}) are taken into account by the coefficient $\Delta\alpha_{FC}(t)$. Here, other symbols represent: $R_{\lambda,pr}$ – the reflection coefficient, $\alpha_{\lambda,\mathrm{pr}}$ – the coefficient of linear absorption, I_0 the intensity of the probe light beam incident on the sample surface, d the thickness of the sample, and k a coefficient expressing the optical-electrical signal transfer in the photo-detector. A linear relation between the measured FCIRA response $\Delta I_{FC}(t) \sim \Delta\alpha_{FC}(t)$ and the density of the excess carriers $\Delta\alpha_{FC}(t) = \kappa_{e\text{-}IR} n_e(t)$ is obtained when $\Delta\alpha_{FC}(t)d << 1$. The FCIRA transient technique is preferably used to examine large carrier density changes.

The non-linear recombination processes are specific for heavily doped materials and devices operating at high injection levels. Radiative and Auger (impact) recombination processes are the most significant processes that limit carrier lifetime with enhancement of excitation density, and extraction of their parameters is thereby important. Excess carrier densities of $n_0 > 10^{18}$ cm^{-3} are needed to highlight the Auger recombination processes and to extract reliably its parameters. Therefore, the condition $\Delta\alpha_{FC}(t)d << 1$ can not always be fulfilled, causing a deviation from the linear relation $\Delta I_{FC}(t) \sim \Delta\alpha_{FC}(t)$. This

non-linearity can be circumvented by an analysis of the FCIRA response normalized to the transmitted probe beam intensity $I_{tr,pr}$ on a logarithmic scale:

$$\Delta\alpha_{FC}(t) = \frac{1}{d}\ln\frac{1}{[1-\frac{\Delta I_{FC}(t)}{I_{tr,pr}(\Delta\alpha=0)}]} . \qquad (3.5)$$

The non-linearity of the function $\Delta\alpha_{FC}(t) = f[\Delta I_{FC}(t)]$ is mostly pronounced within initial stages of the recorded transient. Thus, independent registration of the FCIRA transient and measurements of $I_{tr,pr}=k(1-R_{\lambda,pr})I_0\exp(-\alpha_{\lambda,pr}d)$ for the same sample enable to exclude non-linearities within the FCIRA transmission function. Then, values of $\Delta\alpha_{FC}(t=0)$ are necessary to adjust to the independently determined n_0. The latter is based on the combined measurements of the spectral variations of the light intensity within the excitation pulse, of the excitation area and of the reflection characteristics of the sample under test. Hereby, α_{FC} (the cross-section of the photon-electron interaction for band carriers at the light wavelength of the probe) can be determined by using $\Delta\alpha_{FC}(t=0)$ and with n_0 obtained independently. Equations 3.4 and 3.5 are valid for homogeneous excitation of excess carriers. Actually, for an inhomogeneous initial profile of excess carriers, the integral determines the attenuation decrement for the probe beam intensity due to its time dependent modulation by excess carrier absorption.

The impact of inhomogeneous excitation on the initial carrier generation profile can be roughly estimated by the ratio $\kappa_{e\text{-}IR}\, n_0/\alpha_{\lambda,ex}$, and this quantity can be involved into the normalization procedure by comparing transients measured at different excitation wavelengths $\lambda_{,ex}$. Excess carrier density time dependent changes due to Auger recombination are included by the averaging procedure, implemented using excitation depth integrated light attenuation factor, as

$$\int_0^d \Delta\alpha_{FC}(x,t)dx \cong \frac{\sigma_{FC}n_0}{\alpha}\int_0^{\alpha d}\frac{n(x,t)}{n_0}\alpha dx \quad . \qquad (3.6)$$

Then, evaluation of the Auger recombination is implemented by averaging the data obtained by varying the excitation wavelength, in this work. It is clear that

the impact of inhomogeneity becomes important for times $t>1/\alpha^2 D$. Therefore, examination of the Auger processes is performed by studying the excess carrier density variations within the time range $(1/\gamma_{A,Ge} n_0^2) \leq t < 1/\alpha^2 D$.

For transients, either obtained for homogeneous excitation or after normalization, the analysis can be made using the exact analytical solution of the synchronous linear and Auger recombination rate equation $dn/dt=-(n/\tau_R+\gamma_A n^3)$ with $n=n_0$ at $t=0$, which is given by

$$n(t) = \frac{n_0 e^{-t/\tau_R}}{\sqrt{1+\frac{1}{2}\gamma n_0^2 \tau_R (1-e^{-2t/\tau_R})}}. \qquad (3.7)$$

A hyperbolic-like decay strongly dependent on n_0 should be observed in the first stages of the decay, for times shorter than the linear decay lifetime τ_R. Thereby, fitting of the latter transient enables to extract the value of the Auger coefficient γ.

The typical setup exploited in this work for FCIRA measurements is shown in Fig. 3.2. The probing of FCIRA transients is carried out using steady-state radiation of a halogen lamp. The spectral band of 2.2 – 2.5 μm of this radiation is separated by spectral filters and the light is then focused onto the sample under investigation within the optical parametric oscillator (OPO) excitation beam spot and directed to the detector by using mirrors and lenses adjusted to the IR spectral range. The focused and additionally filtered beam of the IR probe, of which the intensity is modulated by FCIRA, is eventually directed onto a photo-pin InGaAs DET10D/M detector. By this approach, the FCIRA transient is captured by the detector with a time resolution of 10 ns and then recorded using a 1 GHz Tektronix TDS-5104 oscilloscope. The energy of the excitation pulse for each excitation wavelength is controlled by a power meter to evaluate the initial density of the light pulse induced excess carriers.

The FCIRA transients are usually examined after short (~100 fs) pulse excitation using different wavelengths. A near Brewster angle geometry of the experimental configuration among the sample surface orientation, the excitation light polarization and the beam direction as well as the probe beam

direction have been arranged in order to reduce reflection from the sample and to suppress the background intensity of the scattered light. The Brewster angle geometry is also necessary to exclude dynamic interference effect which appears to be important at high densities of the phoexcited carriers due to modulation of the material refraction index.

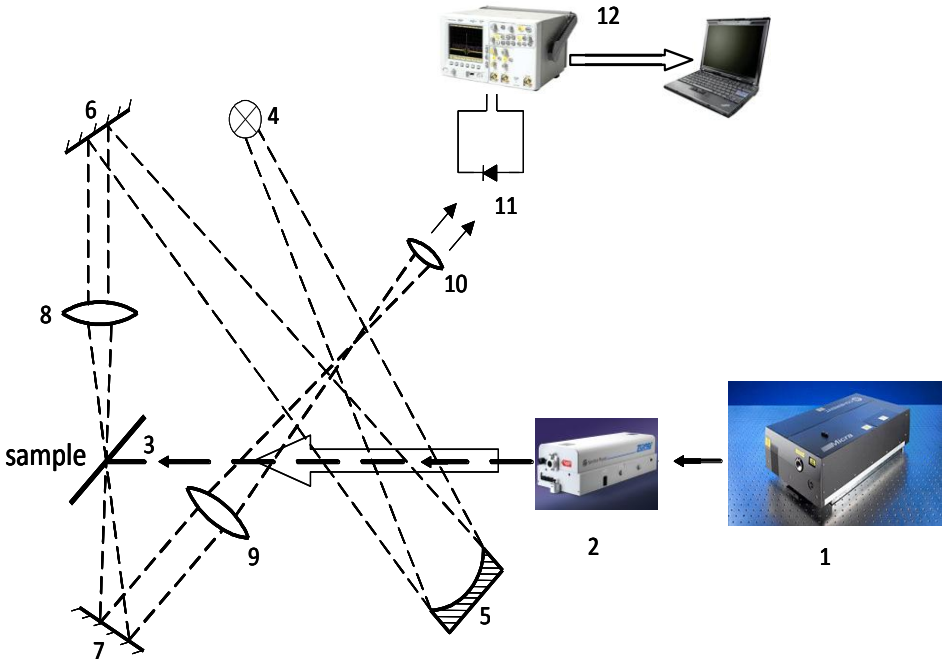

Fig. 3.2. Setup for measurements of the free carrier absorption transients using varied spectrum of excitation. 1,2 – excitation source employing ~40 fs laser (1) and OPO/DFG system (λ_{ex}= 1.2 – 3 μm, 100 – 400 μJ/pulse), 3 – sample, 4 – continuous wave IR probe light source, 5-10 optical elements for light beam orienting, focusing and filtering, 11 – photo-detector, 12 – digital oscilloscope and personal computer.

The light pulses of large intensity, generated by Nd laser with a ns pulses or by an optical parametric oscillator (OPO), are employed in the investigations of the non-linear recombination processes. Additionally, FCIRA transients at excitations with light pulses in the spectral range between 1.2 and 2.5 μm are examined to separate the impact of surface recombination.

3.3. Separation of carrier trapping and recombination parameters

For prevailing bulk recombination, several excess carrier decay processes may compete, thus their impact should be separated. The sum of reciprocal characteristic lifetimes is commonly assumed [21] to be the measured effective decay time, when the interplay of different carrier capture processes can be ignored. The effective carrier decay lifetime is then expresses as

$$\frac{1}{\tau_{eff}} = \frac{1}{\tau_R} + \frac{1}{\tau_{rad}} + \frac{1}{\tau_A}, \tag{3.8}$$

Here, τ_R is carrier lifetime ascribed to nonradiative recombination, τ_{rad} – radiative recombination lifetime, $\tau_A = 1/\gamma_A n^2$ – the instantaneous lifetime associated with Auger recombination.

The non-radiative recombination is governed by defects attributed levels in forbidden band gap. The most widely used model for description of non-radiative recombination is based on Shockley-Read-Hall (S-R-H) recombination statistics approach. This model describes decay lifetime ascribed to a pair of electron and hole, when annihilation of excess carriers happens through deep levels. The S-R-H model is valid just for one type of recombination centres and has several limitations [57, 58]. First limitation concerns to concentration of deep levels (M), which should be small comparing with density of dopants. The second assumption is based on invariant filling of recombination centres by majority carriers ($dm/dt=0$). The third assumption is based on electrical neutrality of the system, i.e. $\Delta n = \Delta p$. Then, the carrier pair lifetime obtained within S-R-H statistic is expressed as

$$\tau_{S-R-H} = \frac{\tau_{n0}(p_0 + P_{VM} + \Delta p) + \tau_{p0}(n_0 + N_{CM} + \Delta n)}{n_0 + p_0 + \Delta n},$$
$$\tau_{n0} = \frac{1}{\gamma_n M} \qquad and \qquad \tau_{p0} = \frac{1}{\gamma_p M} \tag{3.9}$$

Here, γ_n and γ_p represent carrier capture coefficients for electrons and holes respectively; N_{CM} and P_{VM} are effective densities of band states for electron and hole thermal activation from the level M; τ_{n0} and τ_{p0} are the microscopic lifetimes of electrons and holes, respectively; n_0 and p_0 as well as Δn and Δp

denote equilibrium and excess densities of electrons and holes, respectively. The $\tau_{S\text{-}R\text{-}H}$ is asymmetric in respect to minority and majority carrier microscopic lifetimes (Eq. 3.9), and $\tau_{S\text{-}R\text{-}H}$ at low excitation level ($\Delta n << n_0$) is determined by the minority carrier lifetime.

Value of $\tau_{S\text{-}R\text{-}H}$ also depends on the excess carrier concentration, and, for *n*-type conductivity semiconductor, carrier lifetime, including excitation level index $k=\Delta n/n_0$, can be re-written as

$$\tau_{S-R-H} \approx \tau_{n0}\left[\frac{p_0 + P_{VM}}{(k+1)n_0} + \frac{k}{k+1}\right] + \tau_{p0}\left[\frac{N_{CM}}{n_0(k+1)} + 1\right] \tag{3.10}$$

Variation of $\tau_{S\text{-}R\text{-}H}$ with excitation level depends on the activation energy of the dominant recombination level. Thereby, measurements of the dependence of excess carrier lifetime on excitation level *k* may serve for separation of the trap electrical type, i.e. for determination if trap behaves as either a donor or acceptor like centre. Also deep level activation energy could be evaluated from this $\tau_{S\text{-}R\text{-}H} - k$ dependence. However, evaluation of the deep level activation energy is more reliable and precise using $\tau_{S\text{-}R\text{-}H}$ temperature dependent variations [59].

S-R-H model is convenient for simple applications but it does not enable to describe more sophisticated excess carrier decay processes when deep level density is high comparing with minority carriers or when several deep levels manifest during recombination process. The latter traps interplay processes may cause carrier trapping or multi-trapping processes. A system of two different defect levels, one of which acts as the recombination centre while another as a trapping one due to asymmetrical carrier capture cross-sections, determines the non-exponential excess carrier relaxation process. Analysis of this system is based on instantaneous decay time (τ_i), which depends on excess carrier concentration, on carrier capture ($\tau_c=1/\gamma(M-m)$) and emission ($\tau_e=1/\gamma N_{CM}$) lifetimes. Then, instantaneous carrier decay time is expressed as:

$$\tau_i(t, n_{ex}) = \tau_R\left[1 + N_{CM}\,M/\left(N_C + n_0 + \Delta n\right)^2\right] = \tau_R\left[1 + \tau_e/\tau_c\right] \approx K\tau_R \tag{3.11}$$

As can be deduced from (3.11), the trapping process elongates the characteristic recombination time, estimated by trapping factor *K*. Therefore in order to separate recombination parameters, as τ_R, trapping levels should be suppressed by broad spectra steady-state illumination or by increasing excitation intensity that reduce the ratio $N_{CM}M/\Delta n^2_{ex}$ and makes $K=1$. Trapping process leads to the two-componential, hyperbolic like carrier decay transient. The latter is similar to those transients impacted by surface or Auger recombination. Therefore, specific experiment conditions are necessary to separate and to identify the dominant process and to extract their parameters.

3.4. Recombination characteristics in the system of distributed parameters

Surface and bulk recombination acting together lead to a system of distributed parameters in the analysis of carrier decay processes. For samples of thickness *d* and with carrier diffusion length $L_D<0.1d$ the both side boundary task should be considered even within one-dimensional approximation. The one dimensional mathematical model dependent on boundary conditions is generally based on the solution of continuity equation

$$\frac{\partial n}{\partial t} = D\frac{\partial^2 n}{\partial x^2} - \frac{n}{\tau} \quad , \tag{3.12}$$

with boundary and generalized initial conditions

$$D\frac{\partial n}{\partial x}\Big|_{0,d} \pm s_{0,d} n = 0 , \tag{3.13}$$

$$n\Big|_{t=0} = f(x) .$$

The regimes actual in experiments can be approximated by such the initial conditions,

$$n\Big|_{t=0} = n_0 \tag{3.14a}$$

and

$$n\Big|_{t=0} = n_0 e^{-\alpha x} \tag{3.14b}$$

those are realized at homogeneous (3.14a) and exponential (3.14b) initial profile, respectively.

Several peculiarities appear in formulating of this problem for a system of distributed parameters, when combining boundary and initial conditions. A validity range of the possible solutions can be defined by using a theorem of extremum for parabolic equation. This leads to the statement, that a solution $n(x,t)$ exists in a closed area of $0 \le x \le d$, $0 \le t \le \infty$ with maximum at $n(x_0,0)$ defined by relation $\frac{\partial n}{\partial x}\Big|_{x=x_0} = 0$ [60]. The consequences of these considerations lead to conclusions that the solutions of continuity equation, with boundary conditions of type $n|_{0,d} = 0$ or $n|_0 = 0$, $\frac{\partial n}{\partial x}\Big|_d = 0$, are consistent with initial condition $n|_{t=0} = f(x)$ expressed by the monotonic functions only in intervals. Thus, this solution can be obtained by extrapolation, - not directly putting s values. For the symmetric boundary conditions, a maximum of carrier density is achieved at half-thickness $x_0 = d/2$ as $0 < x_0 < d$. In the case of asymmetric boundary conditions point x_0, associated with maximum of carrier density within carrier profile within sample depth, is located nearby the boundary which is ascribed to the boundary with lowest surface recombination rate.

The solution of the continuity equation is obtained as

$$n(x,t) = Ae^{-(1/\tau + D\eta^2)t} \sin(\eta x + arctg\Theta) = Ae^{-(1/\tau + D\eta^2)t} \cos(\eta(x - x_0)), \qquad (3.15)$$

with transcendental equations relating the space frequencies η, a position of maximal density point x_0 and the boundary parameters as follows:

$$\begin{aligned} \eta x_0 &= arcctg \frac{D\eta}{s_0} \\ \eta(d - x_0) &= arcctg \frac{D\eta}{s_d} \end{aligned} \qquad (3.16)$$

Extraction of recombination parameters at prevailing surface recombination is implemented by employing different methods: 1) by full decay curve simulations and adjustments with experimental data; 2) by cross-sectional profiling of excess carriers to define position of x_0 combined with subsequent consideration of asymmetry using a system of equations, as

$$n(x,t)=\sum_{m=1}^{\infty}A_m e^{-(D\eta_m^2+1/\tau)t}\sin\left(\eta_m x+arctg\,\frac{D\eta_m}{s_0}\right), \tag{3.17}$$

$$ctg\,\eta d=\frac{s_0}{s_0+s_d}\left(\frac{D\eta}{s_0}-\frac{s_d}{D\eta}\right);$$

3) by varying thickness of samples keeping the same conditions on surfaces; averaging regimes: 4) by varying initial excitation profiles.

The excitation profile can be modified by varying excitation wavelength and thereby, absorption coefficient. For the case of at $s_0 = s_d = s$, the thickness d averaged amplitudes can be evaluated for the main decay mode (for m=1) as

$$< A_m >_d = < A_m >_{d,\alpha d=0}\frac{\alpha d/2}{1+(\alpha d/\eta_m d)^2}\left(cth\frac{\alpha d}{2}+\frac{D\alpha}{s}\right). \tag{3.18}$$

This amplitude decreases with enhancement of absorption coefficient for excitation light. Value of η_1 can be then extracted comparing amplitudes for the main decay mode measured at different excitation depths and extrapolated to the initial time instant, namely, $A_1(t=0)$. For extraction of bulk recombination lifetime, an analysis of effective decay time is performed through relation

$$\tau_{eff}^{-1}=\tau_b^{-1}+\frac{D(\eta_1 d)^2}{d^2}. \tag{3.19}$$

Prevailing of surface recombination process is verified by monitoring invariance of the effective decay rate, characterized by constant τ_{eff} within the asymptotic decay curve range, by comparison of decay transients for different excitation wavelengths.

A full decay curve is expressed by time dependent excess carrier density changes as,

$$< n(t) >_d = n_0 \exp\left(-\frac{t}{\tau_R}\right)\sum_{j=1}^{\infty}\frac{8\cdot\exp\left(-\frac{\alpha d}{2}-\eta_j^2 Dt\right)\sin^2\left(\frac{\eta_j d}{2}\right)\left[\alpha\cdot sh\left(\frac{\alpha d}{2}\right)\cos\left(\frac{\eta_j d}{2}\right)+\eta_j ch\left(\frac{\alpha d}{2}\right)\sin\left(\frac{\eta_j d}{2}\right)\right]}{\left(\alpha^2+\eta_j^2\right)\left(\eta_j d+\sin\eta_j d\right)} \quad (3.20)$$

while initial carrier density averaged over sample thickness is evaluated as

$$< n(0) >_d = \frac{n_0}{d}\int_0^d \exp(-\alpha x)dx = \frac{n_0}{\alpha d}(1-\exp(-\alpha d)). \quad (3.21)$$

The latter relation is exploited to normalize amplitude of the excess carrier decay transient to the initial excess carrier density, using equations (3.18) or (3.20). Effective decay lifetime, existing within (3.19), is determined by boundary conditions and does not depend on the initial profile of excess carriers while amplitude of the higher modes strongly decreases with enhancement of absorption coefficient. Therefore surface recombination velocity and bulk recombination lifetime can be measured by changing excitation depth [61, 62].

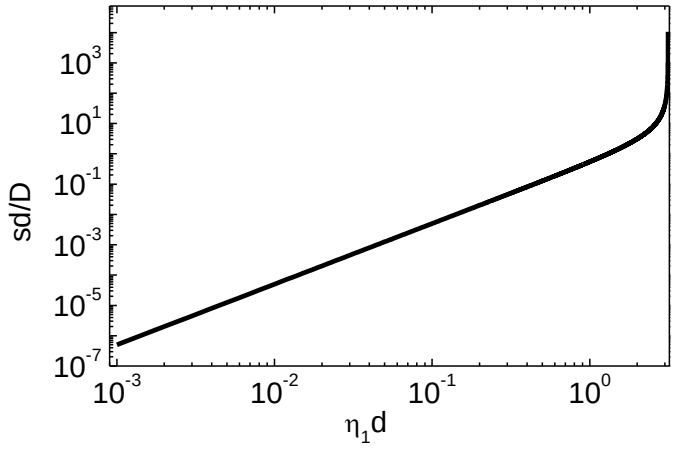

Fig. 3.3. Space frequency of the first surface recombination mode and sample thickness surface recombination.

A dimensionless surface recombination s*d/D* velocity as a function of a product of the space frequency and sample thickness, simulated using transcendental equations of type (3.16), is presented in Fig. 3.3

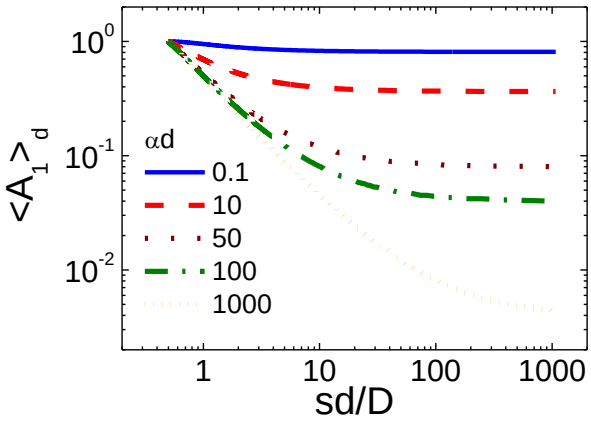

Fig. 3.4. Normalized amplitudes of the main decay mode as a function of the dimensionless surface recombination s*d/D* velocity simulated for different absorption coefficients α, denoted on graph.

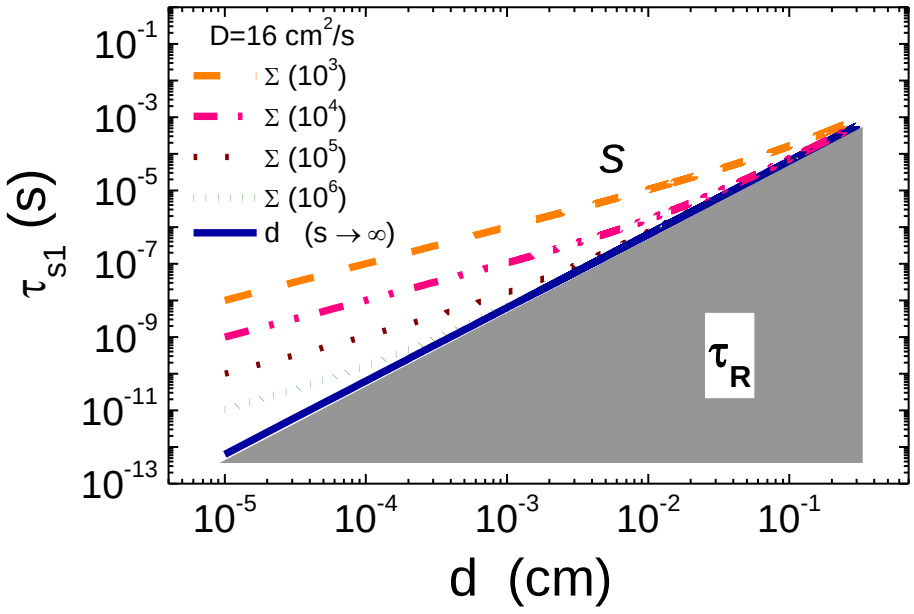

Fig. 3.5. Surface recombination lifetime variation with sample thickness and surface recombination velocity.

Similarly, the normalized amplitude of the main decay mode $A_1|_{t=0}$= $(<n(t)>_d/<n(0)>_d)$ as a function of the dimensionless surface recombination s*d/D* velocity can be simulated. These $A_1|_{t=0}=f(sd/D, \alpha)$ dependences simulated for different absorption decrements αd for the case of the same surface recombination velocity on both wafer surfaces are illustrated in Fig 3.4. The

experimentally measured normalized amplitudes $A_1|_{t=0}$ can be employed for a direct graphical extraction of the dimensionless surface recombination s*d/D*. Then values of *s* can be evaluated, if values of *D* and *d* are determined by complementary techniques or assumed as known values.

The surface recombination lifetime $\tau_s = d^2/\pi^2 D$ calculated for diffusion limited surface recombination regime as a function of sample thickness is presented in Fig. 3.5. It can be inferred that τ_s rapidly decreases with *d*. These simulated surface recombination lifetime variations with sample thickness are also shown in the Fig. 3.5 for different values of surface recombination velocity at fixed carrier diffusion parameter *D*. The surface recombination lifetime is the shortest one for the diffusion limited regime. This regime is indicated by a thick line in Fig. 3.5. The lifetime values for diffusion limited regime, being the shortest ones, determine a time scale of the excess carrier decay. Therefore, the bulk recombination lifetime values (in the area – shaded in grey in the Fig. 3.5) longer than the surface recombination lifetime cannot be extracted directly and reliably, when bulk and surface recombination processes compete [62].

3.5. Instruments for lateral and cross-sectional profiling of carrier lifetime

Several modifications of instruments for lateral and cross-sectional profiling of carrier lifetime within wafer and device samples, based on the carrier lifetime extraction models discussed above, have been designed and manufactured in our IAR laboratory.

A portable instrument VUTEG-3 has been assembled, based on analysis of transients of the microwave probed photoconductivity. This instrument, a picture of which is shown in Fig. 3.6, is designed for distant (>15 m) measurements of carrier lifetime variations associated with introduction of radiation defects. This instrument contains a micro-chip pulsed laser, an IR light beam which is transferred after attenuation by neutral filters and focusing to a measurement area by a fiber optics line. Also it is equipped with a

microwave generator, a MW bridge, with circulators and other modules to adjust and to detect microwave signals. The VUTEG-3 instrument has connectors to either a rectangular waveguide or to a MW coaxial cable, to transfer the MW signals on long lines.

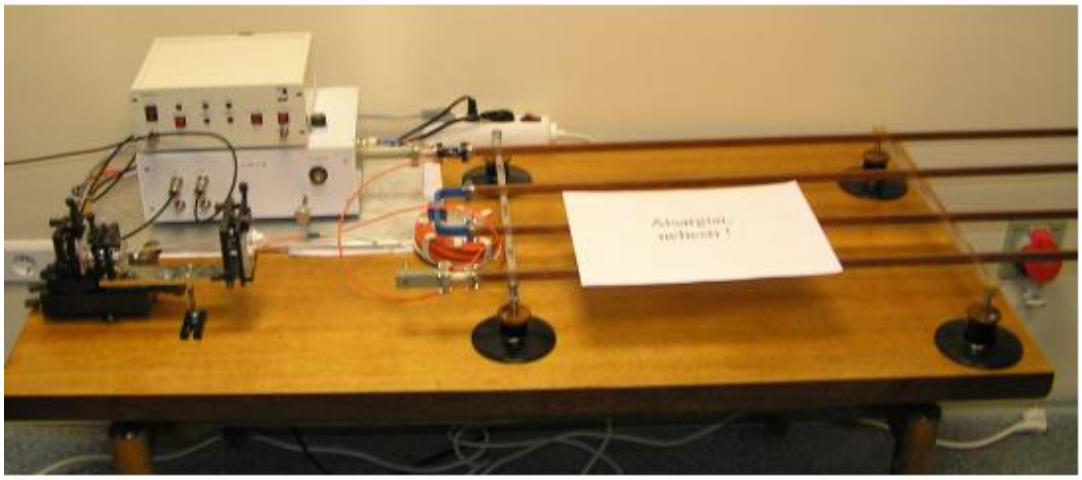

Fig. 3.6. Instrument for in-situ lifetime testing VUTEG-3.

The multifunctional instrument VUTEG-4 has been created for measurements of the planar lifetime variations, within front surface plane, and of the cross-sectional lifetime distribution, profiled on the boundary of the sample under test. Planar distribution of the lifetime within the wafer is very informative tool to control homogeneity of the technological defects distribution. Also this instrument is equipped with source of additional bias illumination. This instrument allows of temperature scans in the range of 0 – 30 ^{o}C. A picture of the VUTEG-4 instrument, where both scanning modes are installed, is illustrated in the Fig. 3.7a.

This instrument consists of several modules. The main module is devoted to measurements of the transients of MW probed photoconductivity and contains a MW signal detection circuit, similar to that installed in VUTEG-3 instrument, and pulsed light source. This module is equipped either with a slit antenna (for planar scans or measurements at fixed point under test) or coaxial needle-tip antenna (to perform boundary scans). In both cases, the near field monitoring regime is actually realized. Antennas can be connected to the MW signals measurement system by using a waveguide switcher. Excess carriers

are generated by micro-chip laser operating at 1062 nm wavelength and generating light pulses of 500 ps. The excitation light spot of dimension of a few tens of microns is directed by optical fiber line to the measurement point.

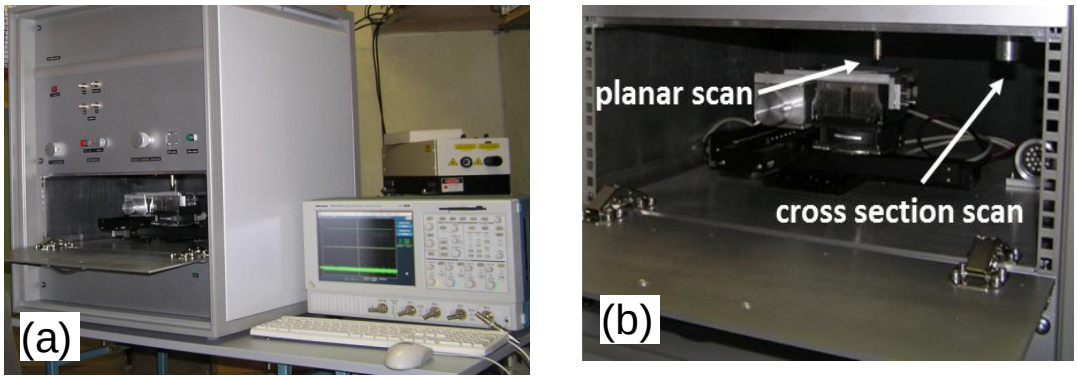

Fig. 3.7. Picture of the multifunctional instrument for planar and cross sectional scan based on MW probing.

Another important module, within VUTEG-4 instrument, is a dark chamber (Fig. 3.7b) for sample mounting, positioning and temperature stabilization. Sample holder is a Peltier cooler mounted on the step-motors driven stage. The initial position and contour of the sample under test is monitored by CCD camera and saved in notebook type computer memory for further controlled movements, when lateral scan regime is applied. Movements of the stage can be adjusted in 3D dimensions. The Peltier elements ensure the stabilized temperature of the sample mounted on polished holder. Resolution of the lateral mapping is about of 1-3 μm. Photoconductivity transients are recorded by oscilloscope and transferred to the computer. Measurement procedure, data acquisition and read out processes are controlled by computer using software created by the author of dissertation.

The cross-sectional scanning of the boundary of wafer-shape sample is implemented by using coaxial needle-tip antenna and a single-mode optical fiber probes. The sample boundary edge is lifted to probes and translated relatively to probes location by 3D stage. The sample holder, in the case of boundary scanning, is attached to the main step-motors driven stage and directed perpendicularly to its planar movements plane. Then, sample

boundary is translated with precision of 1 μm relatively to probes. Probes are mounted in plane, parallel to the sample surface. Position of sample holders and of probes is denoted in Fig. 3.7b.

It has been proved by calibration measurements [63] that carrier lifetime variations within cross-section of layered structure of the semiconductor devices can be very sensitive tool to control deep level distribution within the sample thickness, especially after material irradiations by stopped protons.

Summary of the main results described in the chapter
[A10, A13, A16, P4]

The models appropriate for extraction of carrier recombination parameters by contactless measurements of carrier decay transients using effects of the microwave and infrared absorption by free carriers have been accommodated to validate the combined measurement techniques in wide dynamic range (from 10^{11} to 10^{19} cm^{-3}) of excess carrier densities. It has been proposed and approved the methodology for extraction of bulk and surface recombination parameters, for separation of the impact of carrier recombination and trapping effects, for carrier lifetime profiling within its lateral and depth variations. The combined measurement regimes have been approved. The portable instruments VUTEG-3 and VUTEG-4, based on the designed measurement regimes, have been manufactured, calibrated and employed in multi-functional applications for monitoring of technological and radiation defects.

IV. Contactless and time resolved spectroscopy of deep levels

4.1. Principles of time resolved photo-ionization spectroscopy

Microwave probed contactless photo-conductivity and carrier lifetime spectroscopy technique allows simultaneous control of parameters of the deep levels at room temperature that is similar to condition of devices operation.

The spectroscopy of deep levels can be implemented by using photo-ionization response probed as photoconductivity transients. The transient photo-response signal $U_{\text{MW-PC}}$ probed by microwaves is proportional to the excess carrier density n_{ex} according to

$$U_{\text{MW-PC}}(t) = K(d,\mu,\kappa) * n_{\text{ex}}(t) = n_p \exp(-t/\tau_R), \tag{4.1}$$

with K a proportionality factor which is a function of the sample thickness d, of the material conductivity μ and of κ which is the transfer function of the MW power to the electrical signal of the detector. The initial (time t=0) peak density of the excess carrier concentration n_p averaged over d is evaluated by calibration measurements of K. For an excitation pulse with duration τ_L significantly shorter than the recombination lifetime τ_R, the amplitude $U_{\text{MW-PC}}(0)$ is a direct measure of the intensity of the photo-ionization of deep levels below the Fermi energy. The photoresponse signal calibrated to carrier density

$$U_{MW\text{-}PC}(0) = n_p \tag{4.2}$$

reveals the spectral variation of the absorption coefficient

$$\alpha = n_p / \Phi. \tag{4.3}$$

Light pulse duration integrated flux of photons Φ is determined from the measurement of the light energy per pulse and from the excitation area on the sample surface.

The experimental MW-PC spectrum is usually obtained as a step-like curve representing photon-electron interaction cross-section $\sigma_{ph\text{-}e}$ dependent on photon energy $h\nu$. To calibrate a magnitude of these cross-sections, the normalized to a fixed photon density photo-ionization spectrum is shifted to

intersect point with a photo-absorption spectrum for a well-known value of α. The photo absorption spectrum, taken from literature, sets a scale of the magnitudes of absorption coefficient. Intersection of curves is chosen within plateau ranges of the MW-PC and photo-absorption spectra with well defined parameters of $\alpha(h\nu)$ to eliminate significant errors. Thus, these MW-PC and photo-absorption spectra are coupled at fixed point. Then, the MW-PC signal is additionally controlled at fixed pulsed excitation density (e.g. 1062 nm wavelength), and a photo-absorption coefficient is controlled by the transmission measurements at a fixed wavelength with cw excitation adjusted to the same photon density in the range of transparency of the sample at known wavelength. Thus, the experimental MW-PC spectrum and photo-absorption coefficient are adjusted using the transform data up to the absorption edge spectra, for Si and Ge materials in the range of $0.6 < h\nu < 1.5$ eV. Hereby, a range of the MW-PC amplitudes is scaled to α value. Roughly, this procedure can be implemented graphically by shifting an experimental MW-PC spectrum to coincide the exponential constituents within the MW-PC and photo-absorption spectra. From the rescaled spectrum of MW-PC amplitude, which is proportional to absorption coefficient, a plot $\alpha - U_{MW\text{-}PC}$ as function of photon energy can be coupled with capture cross-section values by using measured n_{ex} values.

Each step in the photo-ionization spectrum, which occurs due to the spectral variation of the cross-section $\sigma_{ph\text{-}e}$ of the photon-electron coupling, is associated with a deep level. The cross-section $\sigma_i = \sigma_{ph\text{-}e}$ of the i-th deep level with activation energy E_i is given by the model of Lucovsky [64]

$$\sigma_i(h\nu) = AE_i^{1/2} (h\nu - E_i)^{3/2} / (h\nu)^3 \quad , \tag{4.4}$$

where A is a multiplicative factor. For the completely filled deep levels, one can write relations

$$\alpha(h\nu) = \sigma_i(h\nu)N_i \tag{4.5}$$

and

$$U_{MW\text{-}PC}(0) = \sigma_i(h\nu)N_i \, \Phi. \tag{4.6}$$

Extraction of values of photo-activation energy E_i is thus possible for constant N_i and Φ even if the density of deep levels is unknown. Each step in the $U_{\text{MW-PC}}$ spectrum, which is identified by a measured change in $U_{\text{MW-PC}}$ by at least a factor of two, is simulated by fitting both the shape and the amplitude of the $\sigma_i(h\nu)$ step. Based on the position of the step on the energy axis, a first estimate of the activation energy E_i is made employing Lucovsky model. Then, the height of the step is fitted by the freely adjustable parameter A. Further iterations to optimize the fit lead to a set of parameters A and E_i for which the least square deviation between the simulated and the experimental values is minimized to a pre-defined accuracy. The important electron – phonon coupling effects at RT could be simulated more precisely by using Lucovsky`s / Kopylov-Pikhtin convolution technique [64, 65] or Huang-Rhys model [66]. However, the electron-phonon coupling effects impact the shape of a step in MW-PC spectrum only within its pedestal even when simulating a single step by Lucovsky`s / Kopylov-Pikhtin convolution technique. Therefore, the multi-step structure of the measured MW-PC spectrum makes vacuous simulations by involving the more comprehensive models.

4.2. Instrumentation for the time resolved photo-ionization spectroscopy

An experimental setup is sketched in Fig 4.1. Several light sources have been combined to implement a pulsed excitation of the photo-response at low excitation level with a ratio of excess carrier density n_{ex} to the doping one n_0 as $n_{ex}/ n_0 < 1$.

In the range of the large absorption coefficients a chopper modulated pulses of 1 ms of the tungsten wide spectrum photonic lamp SI-10-300 were exploited for the wavelengths range of 0.5 – 3 μm, dispersed by a high-brightness Carl Zeiss Jena monochromator with a NaCl prism. Calibration of the photo-generated carrier density is carried out by measuring of a photo-response amplitude when using a 500 ps IR micro-chip laser beam for excitation at wavelength of 1062 nm. The peak amplitudes and carrier decay transients have

been synchronously probed by microwaves at 22 GHz and recorded by a 1 GHz digital oscilloscope TDS-5104. To increase sensitivity of the measurement system, a slit MW antenna has been exploited together with adjusted MW bridge circuit.

In the range of the small photo-absorption coefficients, a short pulse of 40 fs has been employed to eliminate a decrease of the photo-response due to recombination. In the latter experiments, spectral measurements with wavelength in the range from 2.6 – 16 μm are performed by using an optical parametric oscillator (OPO) pumped by the Spectra Physics Ti-sapphire laser. OPO operated on the differential frequencies, when beam of a signal, idle and differential quanta are separated spatially. Maximal light energy generated by OPO is kept in the range of 2 – 28 μJ per pulse to obtain a detectable photo-response signal.

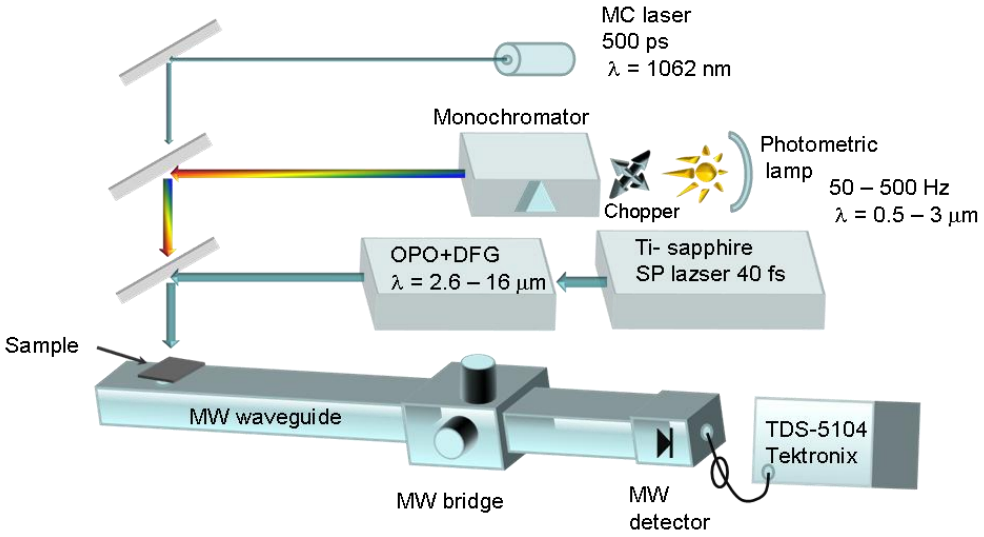

Fig. 4.1. A sketch of the setup of the transient photoresponse measurements instrumentation.

The amplitude of photo-response transient as a function of excitation wavelength has been calibrated to the same fixed light energy per pulse (using the measurements of radiation energy curves of a cw lamp as well as OPO) and, then, to a fixed photon density in the range of 5×10^{10} photon/cm^2 per pulse, by normalizing the number of photons to the maximal quanta employed. A reflection and its spectral variation are taken into account by using the

literature data, e.g. [67] for Ge, in the evaluations of the absorbed light energy by material.

The essential drawback of the photoconductivity technique is that MW-PC spectra show only the changes in free carrier density under photo-excitation with photons of different energy. To evaluate the photo-ionization cross-section, it is necessary to have absolute values of the absorption coefficient. Therefore MW-PC spectra should be rescaled by transferring MW-PC amplitudes into absorption coefficients by exploiting the published literature data. The rescaling procedure performed for Ge samples is illustrated in Fig. 4.2 using literature data [67].

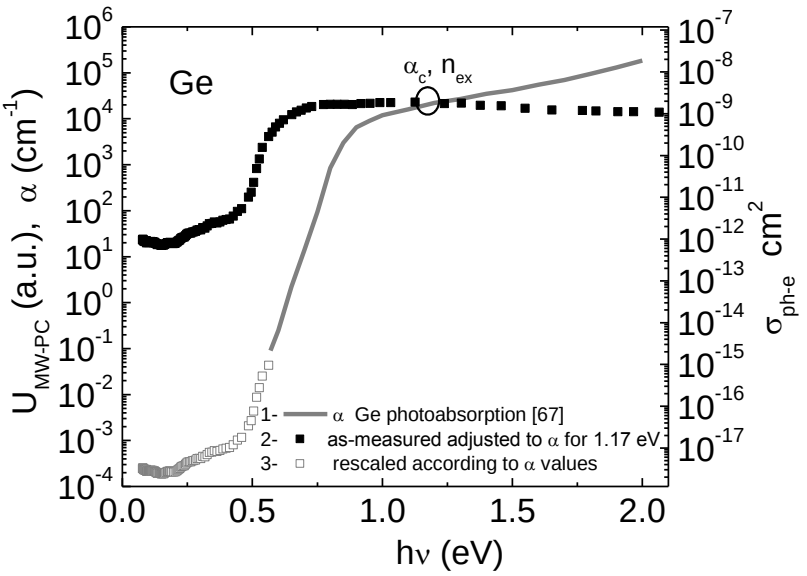

Fig. 4.2. Evaluation of the absolute values of absorption coefficients and photo-ionization cross-sections from the photoconductivity spectrum in the Ni doped samples by including literature data for light absorption spectra.

The experimental spectrum is shifted to the intersect point with a photo-absorption spectrum (curve 2 in Fig. 4.2) to a well-known value of α. The photo absorption spectrum, taken from literature, sets a scale of the magnitudes of absorption coefficient. Intersection of curves 1 and 2 in Fig. 4.2 is chosen within plateau ranges of the MW-PC and photo-absorption spectra with well defined parameters of α to eliminate significant errors. Thus, these MW-PC and photo-absorption spectra are coupled at fixed point shown by circle in Fig.

4.2. Hereby, a range of the MW-PC amplitudes is scaled to α value. The latter cross-section $\sigma_{ph\text{-}e}$ axis is shown on the right side of Fig. 4.2.

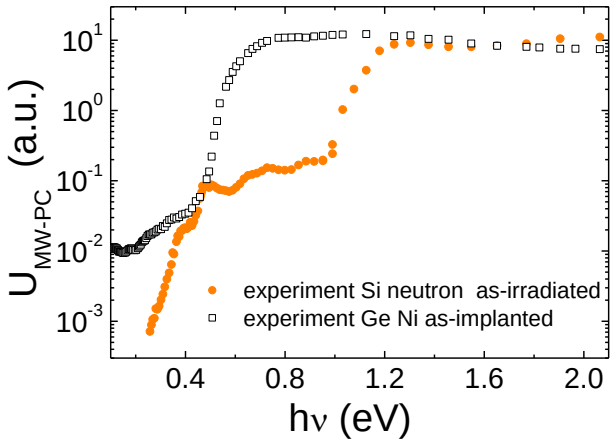

Fig. 4.3. Comparison of typical MW-PC spectra in Si and Ge.

To illustrate the sensitivity and the spectral range of the technique, a spectrum measured on a high resistivity Si sample, irradiated with reactor neutrons, is compared with spectrum obtained in Ni implanted Ge sample (Fig. 4.3). It can be noticed that the photo-response signal for Ge is detected in the complete spectral range between 0.5 and 16 μm, while the photo-response amplitude for Si drops to the detection limit at about 4 μm wavelength. The observed shift of the absorption edges in the measured MW-PC amplitude spectra for Ge and Si is in agreement with the respective band gaps E_g at room temperature. Several steps can be resolved in the both spectra and analyzed by the above described scaling and fitting procedure in detail.

4.3. Time resolved photo-ionisation spectra in the irradiated Si structures

The designed technique of time resolved photo-ionization spectroscopy has been applied for characterization of radiation induced deep levels in Si materials.

A typical photo-ionization spectrum measured for as-irradiated Si wafer sample is illustrated in Fig. 4.4a. It contains three inherent segments, namely, the range of intrinsic absorption, absorption edge and of bulk absorption due to

deep levels. The photo-conductivity amplitude spectrum in the range of intrinsic absorption is rather flat for high energy photons (Fig. 4.4a), due to well passivated sample surface. A peak photoconductivity value within all the spectrum appears for the photon energies at $\alpha d \sim 1$, i.e. for rather large absorption coefficients α, and for photon energies $h\nu$ above the band gap E_G of Si. The photo-conductivity amplitude, corrected to the same photon density, sharply drops (Fig. 4.4a) with a decrease of the photon energy below E_G in agreement with the absorption edge characteristic which is close to exponential. This narrow segment of the sharp photo-conductivity drop nearly coincides for all the investigated samples. The third segment in the photoconductivity spectrum occurs for photon energies below 0.8 eV (Fig. 4.4a). This segment contains a step-like structure of the photoconductivity amplitude, as can be observed in Fig.4.4. Absolute values of a step amplitude increase with irradiation fluence as can be noticed in Fig.4.4b.

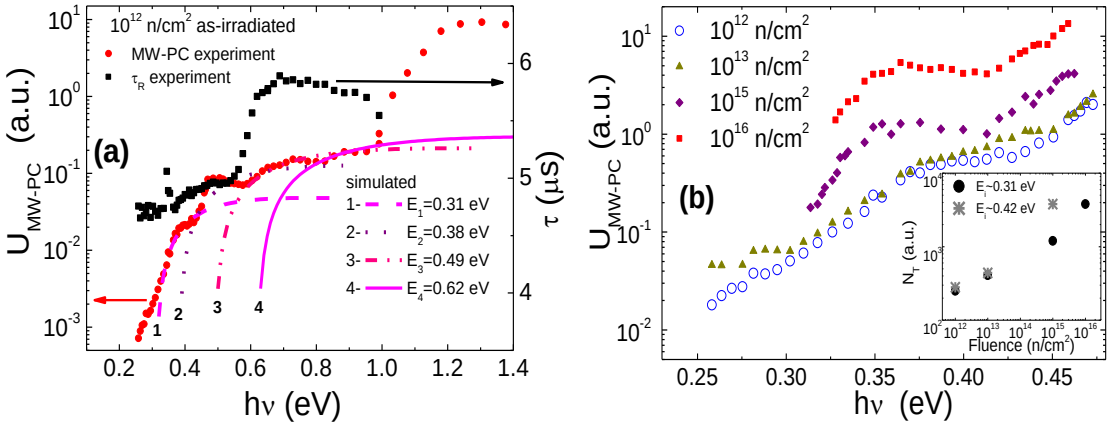

Fig. 4.4. Variations of the photo-conductivity amplitude for surface and bulk excitations of MCz Si (a). Fluence dependent variations of photoconductivity spectra steps in the range of bulk excitations (b). In the inset is relative MW-PC amplitude of the peaks attributed to different deep levels as function of neutron fluence.

Clear steps can be observed for all the irradiated samples. Therefore quantitative simulations have been performed using the model of Lucovsky in order to determine the different levels and their activation energies. Three to

four deep levels have been extracted for all investigated samples. For neutron as-irradiated Si samples, the deep levels with activation energies of 0.31 ± 0.01 (1), 0.40 ± 0.02 (2), 0.51 ± 0.02 (3) and 0.61 ± 0.02 eV (4) are resolved. The values obtained for levels 1 to 4, denoted in Fig. 4.4a, are in good agreement with those extracted by DLTS and TSC [18], i.e. E_C - 0.32, E_C - 0.42, E_C -0.55, and E_V + (0.55 – 0.66) eV [68],- i.e. (1) E_C - 0.32 eV (VOH complex, cluster), (2) E_C - 0.42 eV (di-vacancy), (3) E_C - 0.55 eV (I –centre, V_2O complex) and (4) E_V +(0.55 – 0.66) eV (I – centre, clusters), respectively. However, recombination lifetimes for spectrally resolved excitation with different energy photons slightly vary, as shown in Fig. 4.4a, and increases for the step ascribed to a deep level with activation energy of E_C -0.50 eV.

Relative values of the MW-PC spectra peaks fitted to several deep levels of nearly the same activation energy as a function of neutron irradiation fluence are shown in the inset of Fig. 4.4b. These values represent a relative density N_T of various radiation defects. It can be deduced that introduction rate for different defects increases non-linearly with enhancement of the neutron irradiation fluence. This hints on transformation of di-vacancy related defects into larger agglomerates with enhancement of the neutron irradiation fluence. While recombination lifetime, in the as- irradiated material, is determined by the dominant centre.

4.4. Photo-ionisation spectroscopy in structures of Ge implanted by metals

The time resolved photo-ionization spectroscopy technique has been also applied for identification of deep levels in high purity Ge materials, implanted by different metals as Cr, Co, Ti, Fe, and Ni.

The typical spectra obtained and spectrum steps associated lifetime variations are illustrated in Fig. 4.5.

Lifetime values are obtained to be invariable for the same sample in the range of excitation with $h\nu$>0.5 eV, but depend on implant species. The recombination lifetime is mostly determined by dominant recombination traps,

those were revealed from its dependence on excitation level [69]. Implanted layers peaked at about 42 nm depth for the as-implanted material with effective bulk density of the implanted atoms in the range of $10^{19} - 10^{20}$ cm^{-3} act also as a surface passivating factor, due to introduced surface charge and formed junction (due to metal ascribed acceptor impurities) in a rather lightly doped *n*-type material. Therefore, recombination lifetime extracted from the primary experiments shows an increase with implantation fluence [69].

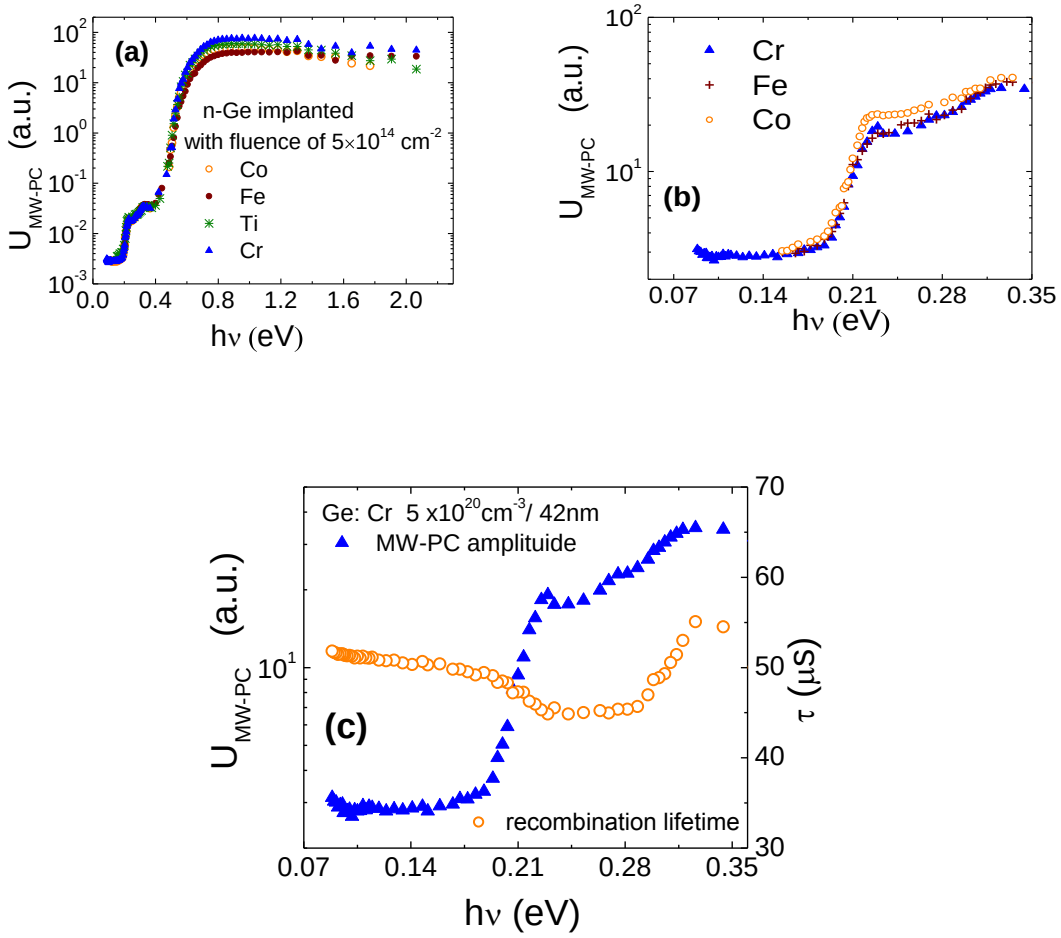

Fig. 4.5. Variations of the photoconductivity amplitude under surface and bulk excitations (a). Comparison of absorption spectra within sample bulk in different metals implanted Ge samples (b). Correlative changes of carrier decay lifetime and the photoconductivity amplitude, measured synchronously for the Cr implanted Ge as a function of a photon energy (c).

Due to mentioned reasons, the photoconductivity amplitude spectrum within a wing of high energy photons occurs to be rather flat (Fig. 4.5a), when excitation is performed on the implanted side. A most significant change of

photoconductivity amplitudes has been found for bare Ge wafers in the range of excitation above 0.5 eV. While this characteristic is nearly flat for the well passivated samples. A peak photoconductivity value within all the spectrum appears for the photon energies at $\alpha d \cong 1$ in the range of the large absorption coefficients α, for $h\nu$ above a band gap E_G of Ge.

The photoconductivity amplitude, corrected to the same photon density, sharply drops (Fig. 4.5a) with decrease of a photon energy for $h\nu < E_G$. This result is in agreement with the absorption edge characteristic which is close to exponential [67]. This narrow segment of the sharp photoconductivity drop nearly coincides for all the investigated samples.

The third segment in the photoconductivity spectrum occurs for the photon energies below 0.5 eV (Figs. 4.5a and 4.5b). This segment contains a step-like structure of the photoconductivity amplitude, as can be observed in Fig.4.5c.

The correlated steps of lifetime and photoconductivity amplitude variations have been revealed for several samples in the spectrum range below 0.5 eV. Variations of the photoconductivity amplitude and of carrier decay lifetime, measured synchronously, as a function of photon energy for the Cr implanted sample are illustrated in Fig.4.5c. This implies that photo-absorption induces a considerable filling of centres within a definite photoconductivity spectrum step-range, when correlated variations of the photoconductivity lifetime and amplitude are observed for the specific deep levels.

The clear step-like structure of the photo-ionization spectra had been observed for all the implanted samples (Figs. 4.5 and 4.6). The simulations of the spectra steps have been carried out by exploiting Lucovsky‘s [64] model to determine the content of levels and their activation energy, as illustrated in Fig.4.6.

Three-four deep levels have been extracted for all the investigated samples. It has been determined that activation energy of most of the extracted deep levels ranges from 0.16 to 0.25 eV, and a level from this range can be found for all the investigated implants. This hints that several levels could be ascribed

to the growth defects in the initial Ge material. Shallower level has been observed in Cr and Co implanted samples. The deeper levels were revealed in Cr, Fe and Ti implanted samples.

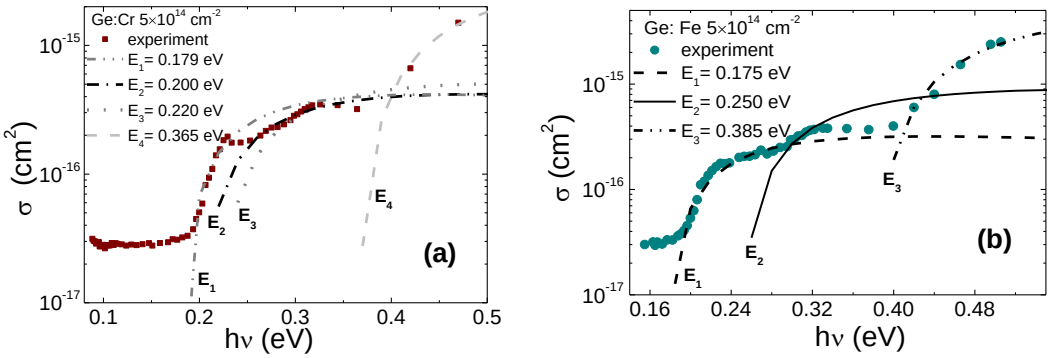

Fig. 4.6. Experimental and simulated MW-PC spectra for the Ge:Cr (a) and Ge:Fe (b). Simulated steps with different activation energy values are shown by lines.

Table 4.1. Activation energies of recombination centres extracted by simulations of the carrier lifetime excitation level dependences ΔE_R [69], from MW-PC spectroscopy (MW-PCS) are compared with DLTS values [70, 71].

Implant	$\Delta E_R = E_C - E_R$ (eV)	*MW-PCS* E_i (eV)	*DLTS* (eV)	
Fe	0.35	E_1=0.175, E_2=0.250, E_3=0.385	E_V + 0.34	E_C - 0.27 E_C - 0.36
Co	0.32	E_1=0.10, E_2=0.18, E_3=0.23	E_V + 0.09 E_V + 0.25	E_C - 0.31
Ti	0.39	E_1=0.175, E_2=0.225, E_3=0.410		E_C - 0.22
Cr	0.34	E_1 = 0.179, E_2 = 0.20, E_3 = 0.22, E_4= 0.365	E_V + 0.07 E_V + 0.12	E_C - 0.37
Ni	0.34	E_1 = 0.17, E_2 = 0.21, E_3 = 0.33, E_4= 0.42	E_V + 0.22 E_V + 0.42	E_C - 0.16 E_C - 0.30

The activation energies of deep levels extracted by fitting of MW-PC spectrum steps are compared in the Table 4.1 with activation energy of

dominant centres evaluated from lifetime dependence on excitation level by using S-R-H model [69] and DLTS results [70,71] obtained for the same implants. It can be deduced from the Table 4.1, that values of dominant S-R-H centres are close to those of the deepest levels estimated in this investigation for almost all the implants.

Excess carrier lifetime variations correlated with steps of MW-PC spectrum, as illustrated in Fig. 4.5c for Cr implanted Ge, may be an indication of the recombination activity of the specific centres. For Ge: Cr samples, it can be noticed, that E_1 and E_2 centres (Fig. 4.6a) intensify significantly carrier capture process, while in the spectral range of the level E_3, lifetime is restored and even increased. Deep level E_4 again causes a decrease of recombination lifetime in agreement with data simulated by S-R-H statistics (Table 4.1).

The MW-PC spectral technique does not enable to unambiguously bind the observed levels to the conduction or valence band. Therefore, the extracted values of activation energy in these experiments have been compared with those estimated from DLTS experiments. In Fe implanted Ge, levels E_2 and E_3 are in quantitative agreement with values determine by DLTS, keeping in mind the experimental errors and activation features of optical and thermal transitions within configurational space. For Ge:Co, agreement is also obtained, excepted the deepest level, which is missing in MW-PCS. In Ti implanted Ge, level E_2 coincides with that observed in DLTS, however additional levels have been resolved in the MW-PCS and lifetime control experiments. For Ge:Cr, an agreement has been obtained for level E_4 when wide structure of $E_1 - E_3$ levels was tentatively separated in spectrum mid-range.

The Ni implanted Ge wafers (38 Ω cm and 500 μm thick) implanted with Ni (90 keV, 5×10^{14} cm^{-2}) were additionally investigated before and after anneal for 1 h at 700 ^{o}C.

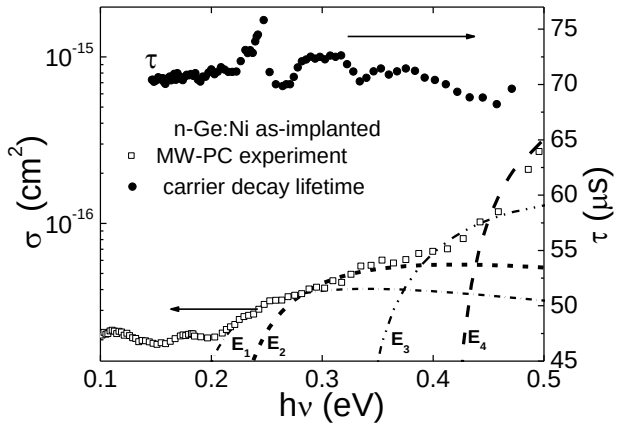

Fig. 4.7. MW-PC and lifetime spectra in as- implanted by Ni Ge sample.

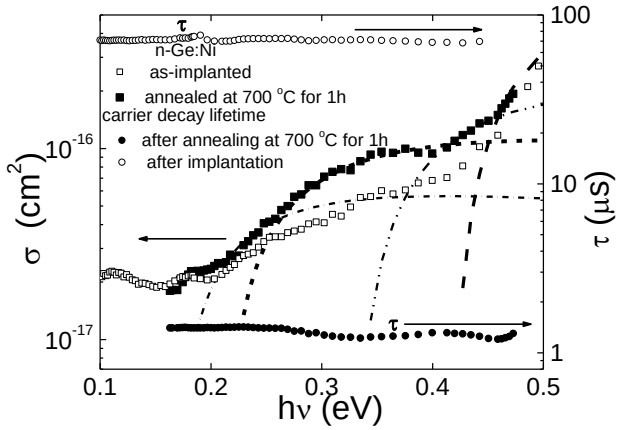

Fig. 4.8. Comparison of capture cross section and carrier lifetime spectra measured in Ni implanted Ge sample before and after annealing at 700 ^{o}C for 1h.

The heat treatment is sufficient to in-diffuse the Ni impurities throughout the whole wafer thickness. The bulk Ni impurity density is in the range of 2×10^{15} cm^{-3}, close to the limit of Ni solubility in Ge, as estimated by using the parameters of anneal exposure, atomic diffusion, source concentration within 45 – 300 nm depth and surface density of Ni implants measured by SIMS profiling [69]. The implantation induced intrinsic defects act together with the implanted metals, causing complicated recombination characteristics dependent both on excitation and annealing conditions.

A typical photo-ionization spectrum obtained for Ge:Ni is shown in Fig. 4.7. For the simultaneously measured excess carrier decay lifetime, the step-like variations are also observed. These lifetime variation steps correlate well with the observed MW-PC amplitude steps. This illustrates the different influence of each deep level in the carrier recombination process.

Thermal annealing reduces the carrier lifetime as revealed when comparing photo-ionization spectra of the as-implanted and heat treated samples (Fig. 4.8). Nearly the same levels are extracted for the as-implanted and the annealed samples by fitting the steps in spectrum. Thus, the change in amplitude of the steps reveals the change of concentration of the specific centres. Comparison of the spectra in Fig. 4.8 indicates that anneal lowers the concentration of the shallower traps, while the concentration of the deeper ones increases and an additional, deeper centre is formed. The increase of the concentration of recombination centres causes significant reductions of the recombination lifetime after anneal. However, the recombination activity of various centres appeared to be different, as revealed within carrier lifetime spectral variations (Fig. 4.8) under photo-activation of the specific defects.

4.5. Time resolved photoconductivity quenching spectra in implanted Ge

It has been determined from the photo-ionization spectroscopy investigations that the native defects act together with implantation induced impurities yielding complicated recombination characteristics in Ge, dependent both on implantation and excitation conditions. It was found that effective lifetime (τ_{eff}) of carrier decay increases with implantation fluence, while absolute τ_{eff} values significantly vary with implants species. Additionally, τ_{eff} increases after short anneal relatively to the as- implanted state. Activation energy values of dominant centres had been evaluated from lifetime dependence on excitation level by using S-R-H model and employing MW-PC for the same implants. In these structures the photoconductivity-quenching (PCQ) effect has been identified.

The PCQ effect is characterized by synchronous decrease of the pulsed photoconductivity amplitude, by appearance of the non-exponential decay, specified by the initial (τ_{in}) and asymptotic (τ_{as}) decay lifetimes, and by shortening of these lifetimes under steady-state infra-red bias illumination (IRBI), as illustrated in Figs. 4.9.

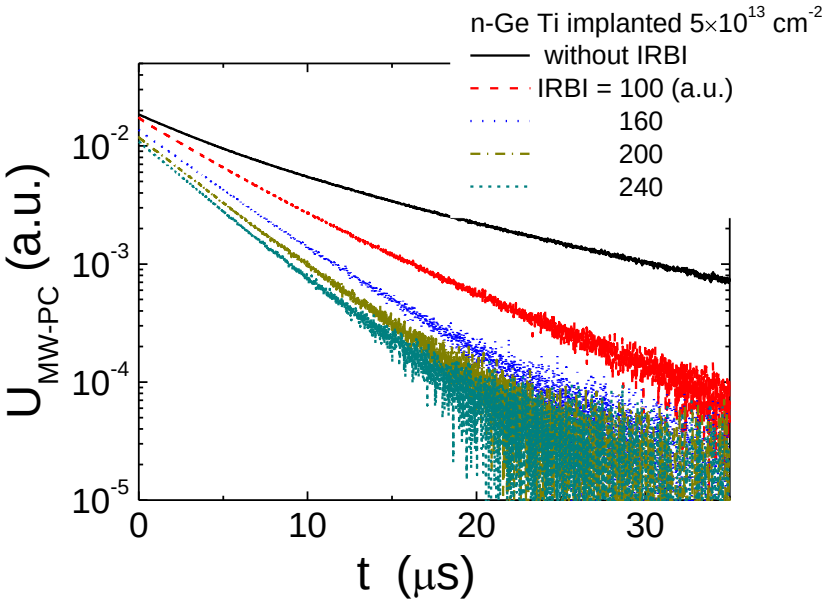

Fig. 4.9. Carrier decay transients variation with infrared bias illumination intensity in Ti implanted Ge sample.

The PCQ effect has been observed in all the metals implanted Ge samples, while its amplitude was found to be the largest in Cr implanted material (Figs. 4.10a and 4.10b). The photoconductivity quenching effect was resolvable for rather wide IRBI wavelengths band. The amplitude of the pulsed photoconductivity and $\tau_{in,as}$ show correlated drop of their values. The photoconductivity amplitude decreases significantly with enhancement of the density of spectrally integrated IRBI, as illustrated in Fig. 4.10.

The quenching (PCQ) effect can be evaluated by PCQ amplitude, as a difference between the photoconductivity signal measured with bias illumination and that obtained in dark. Thus, the PCQ amplitude has been analyzed by an absolute value $\Delta U_{PCQ} = |U_{MW\text{-}PC} - U_{MW\text{-}PC|\ IRBI=0}|$ of a differential

signal. The PCQ amplitude has been increased with implantation fluence for all species of metal implants. It has been distinguished from the decrease of MW probed steady-state conductivity as a function of the IRBI density that PCQ processes are caused by the enhanced capture of majority carriers.

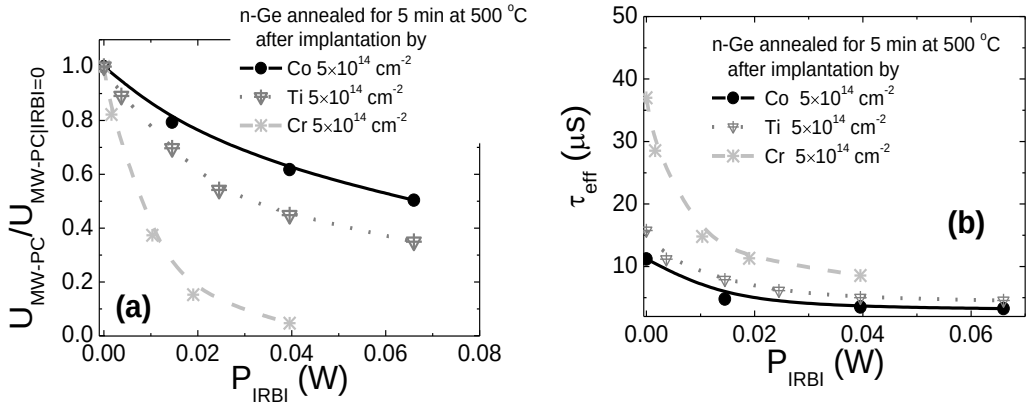

Fig. 4.10. Normalized amplitude of pulsed photoresponse (a) and effective recombination lifetime (b) as a function of infra-red bias illumination power.

Spectral characteristics of PCQ amplitude, shown in Fig. 4.11, have been measured applying spectrally resolved IRBI steady illumination, to identify parameters of deep levels, which determine manifestation of photoconductivity quenching effect. It can be noticed in Fig. 4.11b that a decrease of carrier lifetime is correlated with ΔU_{PCQ} peak, and PCQ effect is clearly observable in the spectral range between 0.4 – 1.3 eV. The spectral changes of the ΔU_{PCQ} amplitude are due to variations of the capture cross-section σ for the IRBI photons which determine the steady-state filling of a specific deep level, as shown for different implants in Fig. 4.11c. The photon energy dependent photon-electron interaction cross-section σ characteristic is simulated by using the model of Lucovsky [64] and allows of determining of the PCQ activation energy. Best fits to the experimental data are shown by the curves in Fig. 4.11d for Cr- implanted Ge. The extracted values of the PCQ activation energies for IRBI photons are listed in Table 4.2.

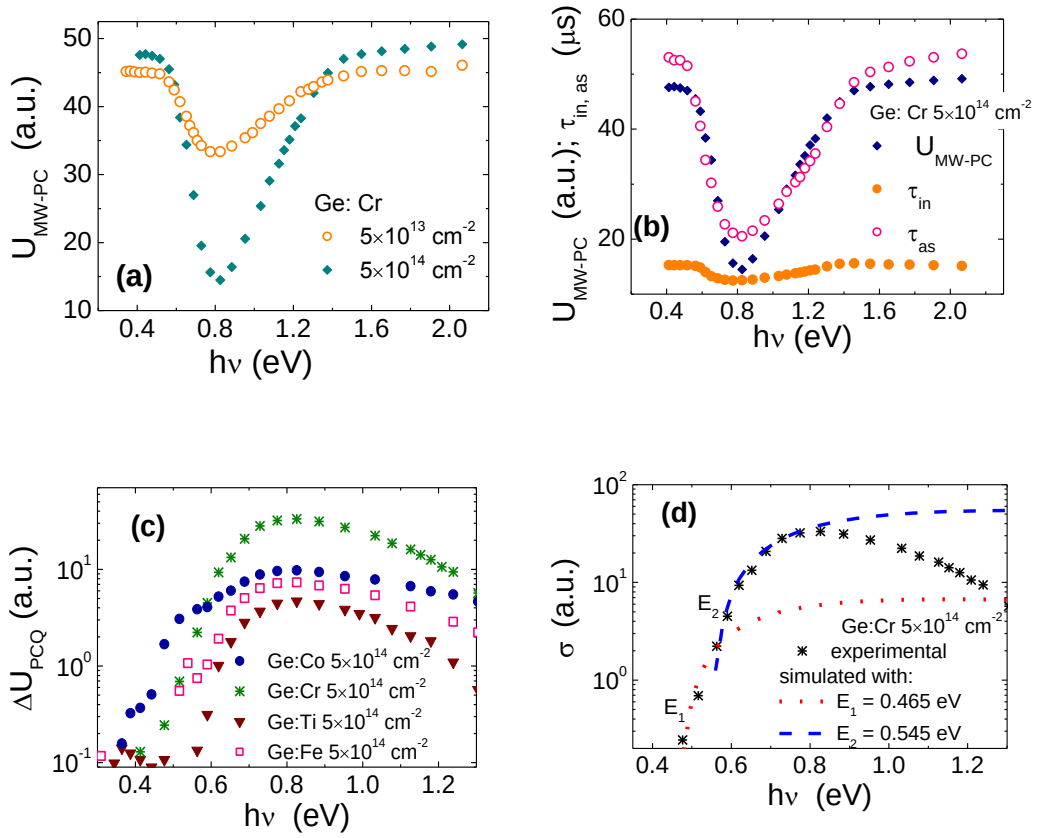

Fig. 4.11. A decrease of the MW-PC amplitude of the pulsed photoresponse in Ge implanted by Cr with different fluencies (a). Comparison of variations of the pulsed MW-PC amplitude and of recombination lifetime components with IRBI spectrum measured in Ge: Cr 5×10^{14} cm^{-2} due to PCQ (b). Differential PCQ amplitude as a function of IRBI photon energy for various implants of fluence 5×10^{14} cm^{-2} (c). Changes of relative values of the PCQ photo-ionization cross-section simulated by Lucovsky model for n-Ge, implanted by Cr with $5\times 10^{14}cm^{-2}$ fluence (d).

Table 4.2. Values of deep levels in metals implanted Ge extracted from photoconductivity quenching spectroscopy.

Co	Fe	Ti	Cr
0.330 eV 0.440 eV	0.530 eV	0.550 eV	0.465 eV 0.545 eV

Summarizing all the experimental observations of PCQ, a sketch of the combined MW-PCS, DLTS and PCQ spectra analysis can be composed for Ge implanted by Co, as shown in Fig. 4.12. The observed PCQ effect can be attributed to the two main processes and involves several deep levels. The first

process is the suppression of Shockley– Read–Hall (S–R–H) recombination by IRBI. The steady- state IRBI excites excess electrons (of density *r*) from the valence band (E_V) to the S–R–H active levels (of concentration *R*). For Co-implanted Ge e.g., the level E_C -0.31eV revealed by DLTS and photo-conductivity lifetime (PC-τ) measurements and also by photo-conductivity spectroscopy (MW-PCS) is the dominant *R* level. Excitation by IRBI drastically changes the filling of this level (*R–r*) and decreases the capture rate for majority carriers from the conduction band (E_C) due to an increased capture time $\tau_C = 1/\gamma(R-r)$, with γ the capture coefficient. The steady-state generation of electrons from valence band creates the same density of excess holes in E_V. Capture of holes by an *R* level is inactivated and balanced by IRBI. This process changes the position of quasi-Fermi levels for holes and electrons in the band gap [72].

The second process is related to the activation by IRBI of other deep levels *S* in the band gap which have a high capture rate for majority electrons. For Co-implanted Ge e.g., the level 0.23eV revealed by MW-PCS (Table 4.1) becomes an effective capture centre for IRBI-generated excess holes. As a result, the recombination flow is no longer controlled by the *R* level but by the *S* level which is activated by IRBI. For the S–R–H-dominated regime without IRBI, when the *R* centre is the more effective catcher of the minority holes, the *S* centres are only revealed as trapping centres. These capture centres do not change the excess density of majority carriers but only delay the recombination decay. With IRBI, the *S* centres decrease the density of majority equilibrium carriers and thus also the overall conductivity, to balance the IRBI- induced holes density. This is the reason for the observed decrease of the steady-state conductivity induced by IRBI.

The spectral PCQ characteristics are determined by the change of the defect configuration and of the electron energy of the centre by the optical filling/charging [73, 74]. This leads to a shift of the electron energy curve associated with a specific defect, relatively to its equilibrium state and to the

appearance of barriers for optical transitions within a configurational space. Experimental determination of these barriers provides information on electron–phonon coupling and on the microscopic structure of the defect.

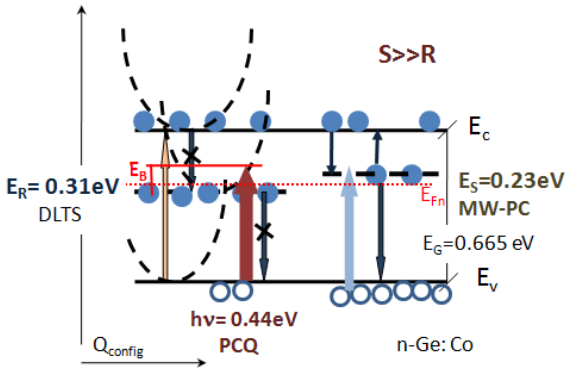

Fig. 4.12 A sketch of redistribution of recombination flows in Ge implanted by Co under cw IRBI excitations.

For Co-implanted Ge, a good agreement is obtained when the DLTS level (E_C - 0.31eV) is assumed to be the *R* centre, which is corroborated by the PC-τ analysis and agrees well with the E_3 level determined by MW-PCS, assuming barrier energy of 0.11eV. The E_2 level determined by MW-PCS for Co-implanted Ge can then be identified as the *S* centre. For Fe-implanted Ge, both DLTS centres compete as *R* centre, while the PC-τ data reveal the dominance of the E_C - 0.36 eV centre. Correlating the DLTS and PCQS results, a barrier of 0.135eV is obtained for the shallower DLTS level as *R* centre. In this case, the E_1 level determined by MW-PCS is assumed to be the *S* centre with the MW-PCS levels E_2 and E_3 close to the DLTS activation energy. For Ti-implanted Ge, the *R* centre is associated with the DLTS level with a barrier of 0.105eV, while PC- τ and E_3 of MW-PCS reveal a competing recombination centre. In that case, the E_1 and E_2 levels of MW-PCS are associated with the *S* centre. For Cr-implanted Ge, the E_C-0.37eV DLTS centre can be correlated with PC- τ and the E_4 MW-PCS level is associated with the *R* centre taking into account a barrier of 0.15eV for the smaller PCQ activation photon energy. The MW-PCS E_1–E_3 levels can in this case be assumed to be the *S* centres.

Summary of the main results described in the chapter

[A10-A14]

The techniques of time resolved spectroscopy of deep levels, based on photo-ionization and photoconductivity quenching effects, have been proposed and approved for characterization of deep levels in Si and Ge structures, ascribed to growth and radiation induced defects. It has been shown that time resolved spectroscopy technique enables one to correlate spectral steps with carrier lifetime changes, and thereby to identify the most recombination active centres. Combined analysis of the photo-ionization and photoconductivity quenching spectral characteristics allows separating of carrier capture flow redistribution in the intricate systems of interacting centres.

It has been shown that the native Ge defects act together with implantation induced impurities causing complicated recombination characteristics dependent on excitation and annealing conditions.

It has been unveiled that Fe and Co impurities implanted into Ge are the most effective lifetime killers in Ge while Cr has the least influence. Coexistence of slow and fast recombination centres, which interplay leads to appearance of the PCQ effect. The acceptor-like behaviour has been ascribed to slow centres while donor-type defects should be attributed to fast ones. The latter ones are responsible for the fast decrease of majority carrier densities under annealing and IRBI.

Several deep levels ascribed to radiation defects in Si have been identified by using time resolved photo-ionization spectroscopy. Photo-activation energy values of these defects are close to those identified by other spectral techniques such as DLTS.

V. Characterization of radiation defects in Si by the bulk lifetime control

Contactless characterization of irradiated Si materials by measuring carrier lifetime dependencies on hadrons irradiation fluence, on temperature, and on heat treatments is described in this chapter.

5.1. Samples and structures investigated

High purity silicon wafers grown by Czochralski method under magnetic field (MCz), Float Zone (FZ) and diffusion oxygenated FZ (DOFZ) techniques have been investigated. Also Si *pin* diode structures of the CERN standard particle detectors have been investigated. Wafer surfaces were passivated with thermal oxide to suppress impact of surface recombination on evaluation of bulk lifetime. Variations of excess carrier lifetime have been investigated after samples irradiation by 50 MeV– 24 GeV/c protons and reactor neutrons using different fluences in the range from 10^{12} to 3×10^{16} cm^{-2}. Carrier recombination lifetime has been measured in the as-irradiated samples, kept under 10 ^{o}C temperature. The isochronal anneals for 24h were also performed by varying heat treatment temperature in the range of 80 – 420 ^{o}C to passivate several point defect species.

5.2. Carrier lifetime dependence on fluence and irradiation type

Lifetime variations with neutron fluence obtained in the as-irradiated Si wafer samples are shown in Fig. 5.1. MW-PC transients exhibit one-componential relaxation indicating prevalence of bulk recombination process. Recombination lifetime decreases nearly linearly with enhancement of irradiation fluence implying dominance of the same radiation defects those concentration increases with fluence.

Values of recombination lifetime obtained in wafer samples nearly coincide with those measured in diode structures irradiated and kept at the same conditions, as illustrated in Fig. 5.1. Moreover, the lifetime dependence on fluence measured in neutron irradiated MCz Si based wafer and detector

structures is close to that determined for proton irradiated standard FZ and diffusion oxygenated FZ (DOFZ) Si diodes. Congruity of these dependences indicates that high energy protons and neutrons induce the same prevailing recombination centres in both MCz and FZ grown materials.

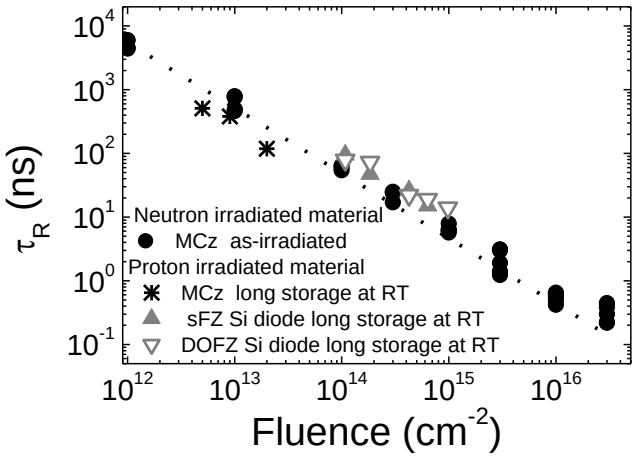

Fig. 5.1. Recombination lifetime as a function of hadrons irradiation fluence in Si wafers and structures.

Short lifetimes obtained in the range of the largest fluences and nearly linear reduction of recombination lifetime with fluence enhancement implies dominance of the recombination centres characterized by a large capture cross-section. It is well known [75], from simulations of the high-energy particle interactions with material, that hadrons, especially neutrons, introduce cluster type extended defects. The large capture cross-sections can be assumed for the extended clusters, to explain short and rather stable values of carrier recombination lifetime observed in our experiments. Existence of clusters is corroborated by combined study of more specific characteristics of these samples, such as the efficiency of diffraction on dynamic gratings [41], the amplitudes and shape of the MW-PC transients, as well as carrier scattering parameters.

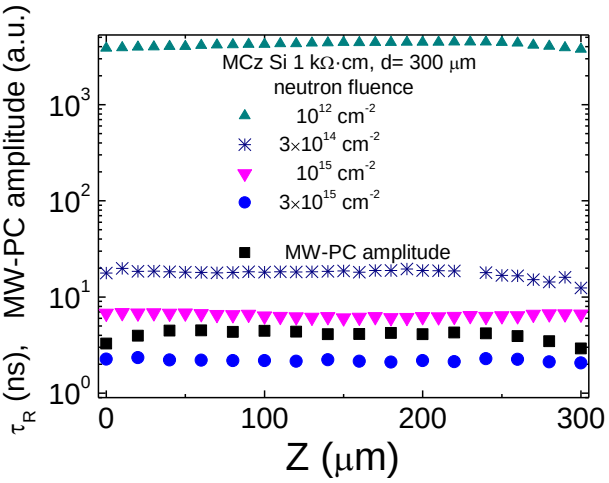

Fig. 5.2. Carrier lifetime depth-distribution profiles measured in MCz Si 300 μm-thick wafers after neutron irradiation using different fluences.

High energy neutrons introduce homogeneous distribution of recombination centres within thickness of wafer samples irrespective of irradiation fluence, as illustrated in Fig. 5.2. These lifetime profiles within wafer thickness have been controlled by lifetime cross-sectional scans performed by MW-PC technique and VUTEG-4 instrument exploiting sharply focused laser beam and near-field needle-tip MW antenna. Amplitude of the MW-PC response is more sensitive to boundary effects, when decrease of excess carrier density due to surface recombination and less excitation intensity can be observed within the photo-response profiles.

5.3. Temperature and anneal dependent recombination characteristics

The isochronal anneals for 24h were performed by varying heat treatment temperature in the range of 80–380 ^{o}C to reveal impact of radiation induced point defects.

Evolution of photoconductivity decays has been investigated after each step of heat treatment. Characteristics of the carrier recombination and trapping/generation were examined by measurements of effective bulk recombination lifetime to keep the same measurement conditions. This effective lifetime really represents the synchronous action of recombination

and trapping centres when it is measured without additional steady-state bias illumination. Existence of the trapping impact can be easily deduced from photoconductivity decay transients, illustrated in Fig. 5.3, where two-componential decays or delayed recombination kinetics can be observed. The effective bulk recombination lifetime slightly increases with isochronal annealing temperature (Fig. 5.3a) and change of carrier decay shape, dependent on fluence occurs under annealing at elevated temperature (>180 ^{o}C). Clear two componential of excess carrier transient with heat treatment shows an enhancement of impact of competition between at least two traps (Fig. 5.3b). The changes of the effective lifetimes of the initial and asymptotic decays components appear to be different for various irradiation fluencies (Fig. 5.4). This implies the complicated transformations of radiation defects under heat treatments. Two components within carrier decay transients are caused by a competition of recombination and trapping centres, induced by annealing, in redistribution of excess carrier capture flows.

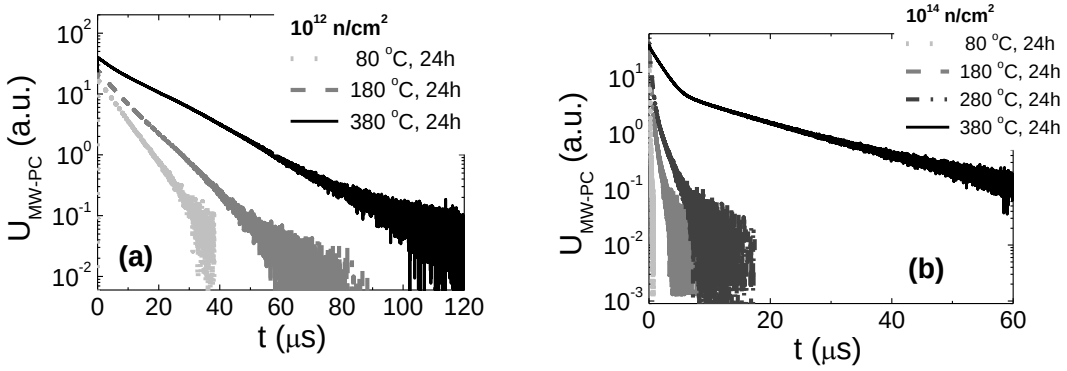

Fig. 5.3. Variations of photoconductivity transients with isochronal annealing temperature in MCz Si irradiated by 10^{12} n/cm^2 (a) and 10^{14} n/cm^2 (b) neutron fluence.

To identify variation of deep level parameters with heat treatment, deep levels photo-ionization spectroscopy has been performed. Post-irradiation heat treatment induces variation of the density of deep levels, which, although, depends on irradiation fluence, as shown in Fig. 5.5. It can be noticed that the density of the deepest levels decreases under anneal for samples irradiated with

fluence of 10^{12} n/cm^2. An opposite change of the density of traps can be deduced for sample irradiated with fluence of 10^{16} n/cm^2.

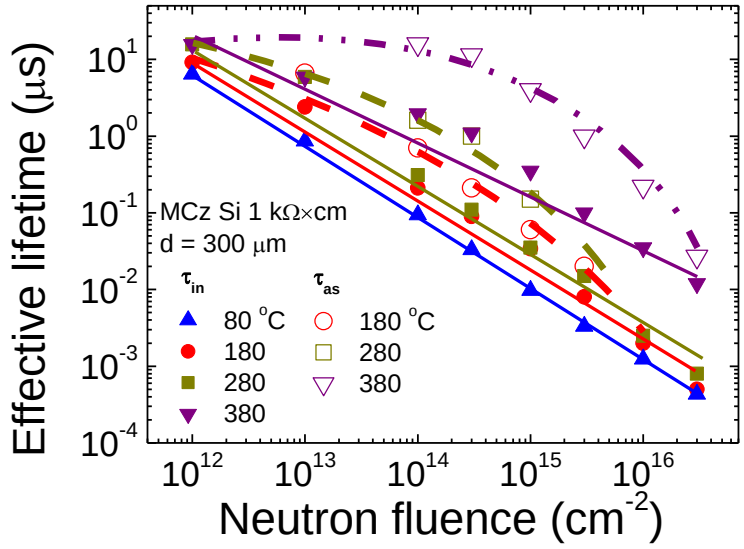

Fig. 5.4 Fluence dependent variation of carrier decay recombination (τ_{in}) and trapping (τ_{as}) components under isochronal 24h heat treatments.

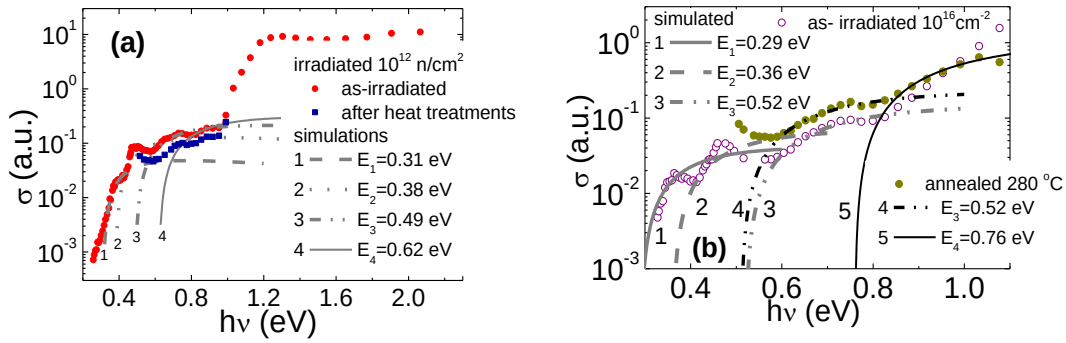

Fig. 5.5. Comparison of deep level spectra for as- irradiated and isochronally annealed at 280 °C for 24 h samples, irradiated with fluence of 10^{12} n/cm^2 (a) and of 10^{16} n/cm^2 (b).

The changes of the effective lifetimes of the initial and of asymptotic decay rates, measured at fixed 1062 nm excitation wavelength, appear to be different for various irradiation fluences. To separate activation energies in more detail, the lifetime variations, ascribed to the recombination and to trapping

constituents within photoconductivity relaxation transients, have been examined as a function of sample temperature. These characteristics are illustrated in Fig. 5.6. Activation energy of the generation traps, as determined from the asymptotic lifetime temperature variations, changes in the range of 0.17 – 0.35 eV. This indicates that different dominant carrier trapping centres are formed by anneals. Activation energy of carrier generation centres is a function of the irradiation fluence.

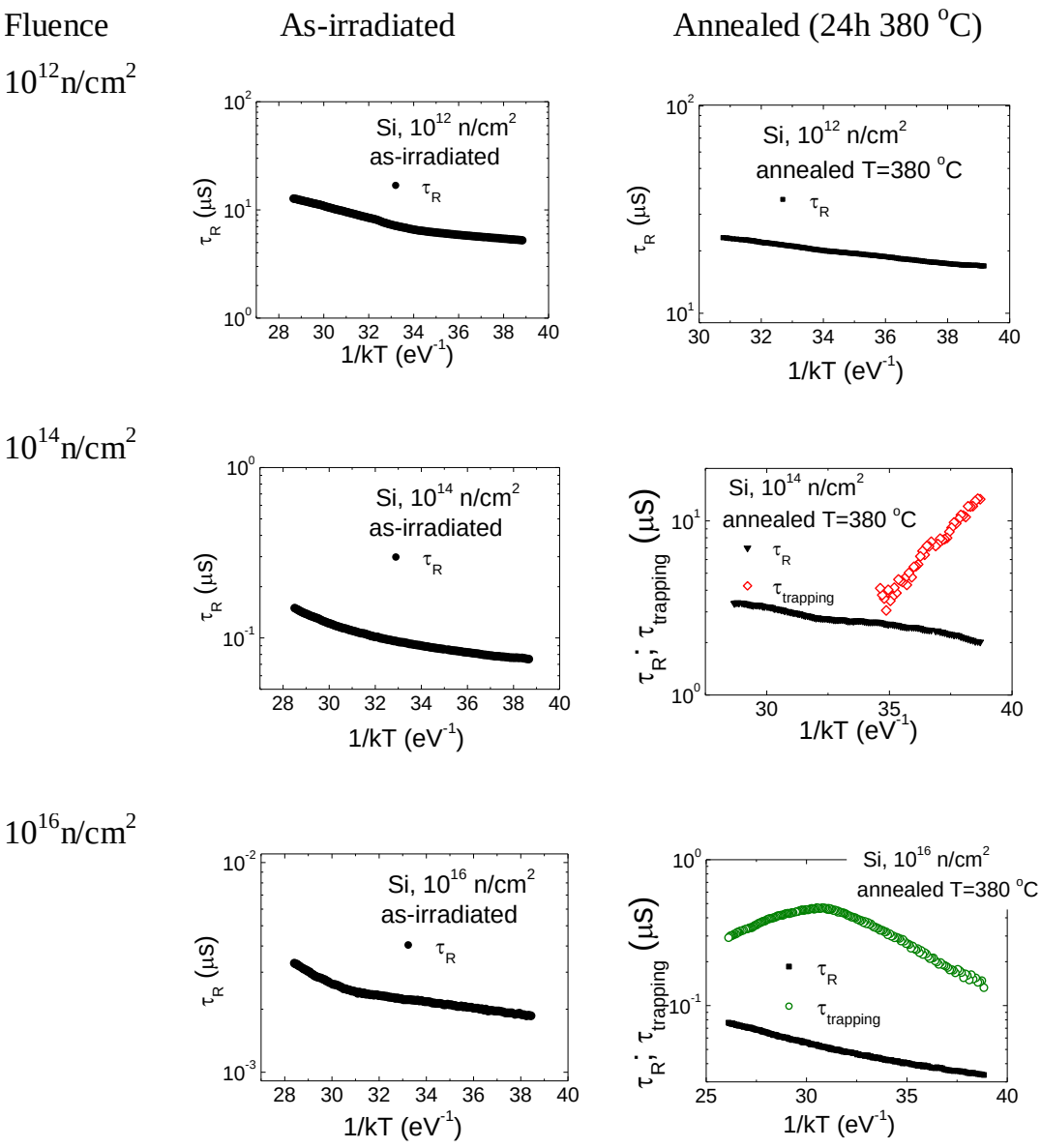

Fig. 5.6. Lifetime as a function of reciprocal thermal energy, ascribed to recombination and trapping components within carrier decay transients, obtained for the as-irradiated and annealed MCz Si samples.

In general, photoconductivity at bulk excitation depends on the contribution of both types of carriers, and amplitude of MW-PC is proportional to a product of free carrier mobility and lifetime. A mobility of holes is significantly less than that of electrons in Si, therefore, holes impact only on diffusion of excess electron-hole pairs in time scale exceeding the lifetime of holes. The excess carrier capture flows are distributed among all the electrically active defects. The single exponential decay observed in the as-irradiated material and obtained nearly linear recombination lifetime dependence on fluence in the annealed samples (Fig. 5.1) clearly indicate dominance of a single recombination centre in the as- irradiated materials. Simulations of neutron interaction with a silicon crystal [76-78] imply crystal damages of 0.1 μm dimension which is less than a Debye length. Hereby, this region acts as an extended cluster-like recombination centre. The cluster can be assumed as a volume with defects-rich boundary surface which causes carrier diffusion from crystal with a subsequent recombination at cluster boundary. The effective lifetime τ_{Reff} for infinite velocity of surface recombination is determined by the minority carrier limited diffusion time $\tau_D=\pi^2 D_m/d^2$, as $1/\tau_{Reff}=1/\tau_{Rcryst}+1/\tau_D$ [48]. Here, D_m is a diffusion coefficient of holes (minority carriers), d – is an average distance between the clusters, and τ_{Rcryst} is the bulk recombination lifetime in crystal. According to literature data [76-78], the distance d changes from 200 μm to 20 nm, when fluence increases from 10^{12} to 10^{16}cm^{-2}, respectively. Analysis of τ_R dependence on temperature, in assumption that $\tau_R \approx \tau_{Reff}$, and τ_{Reff} variations with temperature is mainly determined by a temperature characteristic for $D_m = f(T)$, gives the mentioned function $\tau_R \approx \tau_{Reff} = T^m$, with $1<m<2$. This corresponds to the proposed $D_m(T)$ and explains a rather small activation factor, in contradiction to assumption of pure recombination on cluster with deep levels ascribed.

Transforms of these regions under heat treatments change the density of trapping centres (Fig. 5.6). However, spectral characteristics of deep centres (Fig. 5.5) show that density of several levels (E_1–E_3) increases under heat

treatments for medium range of fluencies while it decreases in samples irradiated by the highest fluencies. The temperature dependences (Fig. 5.6) of the asymptotic decay lifetime also corroborate manifestation of cluster related recombination and trapping centres. The latter changes of recombination-trapping characteristics can be explained by variation of distance *d* between clusters, dependent on irradiation fluence.

Summary of the main results described in the chapter

[A9, A14, P9-P11, P14, P16, P19, P23]

The linear bulk recombination lifetime decrease with enhancement of hadrons irradiation fluence has been revealed irrespective of particles type and energy. This lifetime characteristic shows the same absolute values of carrier lifetime ascribed to definite irradiation fluence values, irrespective to material growth technology and structure, nearly the same for wafer samples and particle detectors.

It has been corroborated by depth profiling of the carrier lifetime distribution that penetrative hadrons induce homogeneous distribution of radiation defects within Si samples of thickness ≤ 300 μm. Small lifetime reduction can be only observed within boundary edges due to enhanced surface recombination or carrier leakage.

The temperature and anneal dependent variations of trapping lifetime enable us to reveal fluence governed formation of cluster defects. The clusters related recombination and trapping centres cause complicated changes of the recombination-trapping characteristics. These changes of recombination-trapping characteristics can be explained by variation of distance *d* between clusters, dependent on irradiation fluence.

VI. Examination of the evolution of radiation defects during irradiations

Direct measurements of microwave probed photoconductivity transients (MW-PCT) have been utilized for remote and *in-situ* excess carrier lifetime measurements. Lifetime of free carriers is inversely proportional to concentration of defects; therefore MW-PCT technique is beneficial to control processes of defect creation during irradiation. Simultaneously, a spectroscopy of activation energy of dominant traps can be performed before and just after irradiation by temperature scan of variations of the recombination parameters.

6.1. Measurements arrangement for in situ control of carrier lifetime

Defect creation processes have been examined through analysis of variations in the microwave probed photoconductivity transients by using instrument VUTEG-3, described in Ch3, for remote measurements. This instrument has been adjusted to the irradiation chamber of accelerator and installed in protons accelerator at Division of Materials Physics of Helsinki University. A sketch of experimental arrangement is shown in Fig. 6.1. To maintain the safety requirements, the main measurement equipments were placed in safe area at a distance of about 15 meters from the irradiation chamber, and remote measurement regime was arranged. The setup of experiment consists of three main components: measurement (VUTEG-3) and remote control components (1), lines of signals transfer (2), and irradiation chamber components.

The main measurement instrument VUTEG-3 contains a microchip laser STA-01 for pulsed photoconductivity excitation, a continuous wave microwave (MW) system for probing of photoconductivity transients, an oscilloscope for measurement of signals, and a personal notebook type computer (PC) for data processing as well as for distant control for remote positioning of probes. System for generation of excess carrier is equipped with a light intensity attenuator, a telescope to couple laser beam into the fiber core, and a fiber cable for excitation beam transfer to a sample. Also second

harmonic generator is incorporated into this system for measurement of carrier lifetime at different depth of the sample. Microwave probe system contains a MW generator (22 GHz range), a MW detector with the load matching elements, a circulator for separation of generated and reflected MW radiation, a MW bridge for adjustments of the MW lines, and a MW waveguide terminal to transfer the MWs to a sample and to collect MW probed signal. A photo-response signal is proportional to an excess carrier density. Thus, the carrier density decay transient resulted from pulsed 500 ps excitation of either 1062 or 531 nm wavelengths and registered by a MW detector, has been measured by a 1 GHz Agilent Technologies DSO6102A oscilloscope. Electrical signal from oscilloscope is transferred to PC and analyzed during and just after proton irradiation on wafer samples. Transients during irradiation are registered every tenth millisecond. To enhance precision of measurements of the recombination lifetime reduction rates as a function of fluence, a proton beam current has been varied to set small steps in values of the collected fluence.

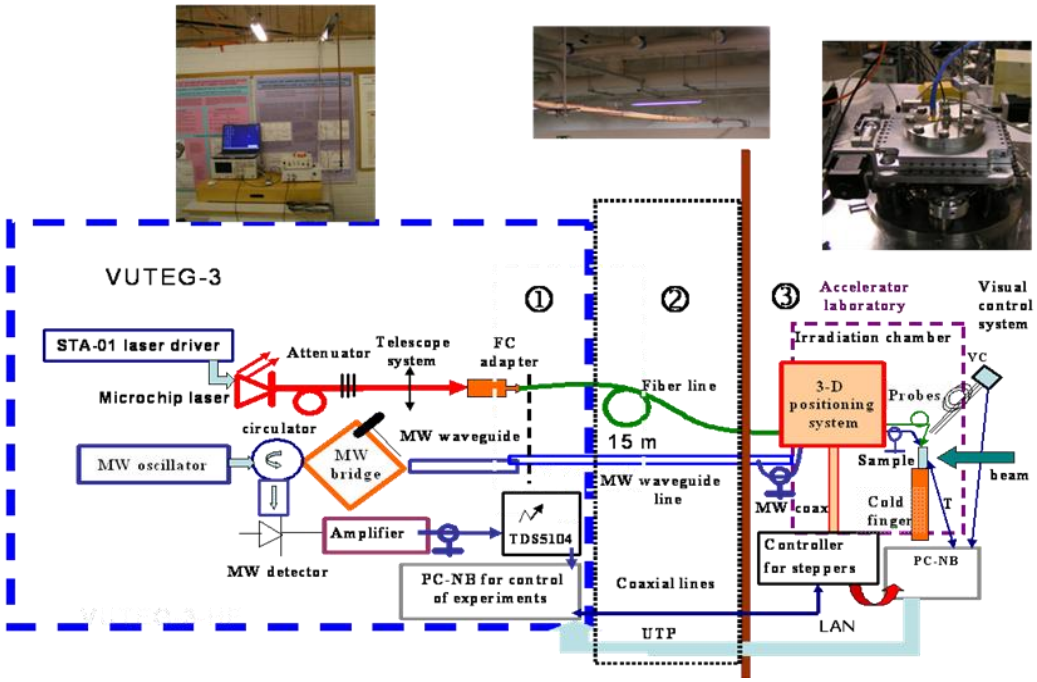

Fig. 6.1. Instrumentation for the remote in situ measurement of carrier recombination characteristics during irradiation.

Components of signal transfer at a distance of about 15m between the irradiation chamber and of the measurement instrument are (i) a waveguide line with low attenuation for long-distance transmission of MW radiation, (ii) a fiber optic cable assembly for conveyance of excitation light, (iii) the USB cables for transfer of video signals from video camera connected to fiberscope and for electrical signals of a temperature control system, for distant manipulation of step motors installed on three-dimensional (3D) stage on top flange of the vacuumed irradiation chamber. The excitation fibre lines, the multi-fibre trunk of a fiberscope for an in-chamber video control of the positioning of the probes relative to a sample boundary, are installed into irradiation chamber via top flange of a chamber by using vacuum connectors and the top flange is tightly attached to a 3D stage driven by step motors. Transition between a MW waveguide line and a short coaxial cable is arranged near the irradiation chamber to get low attenuation in transmission of MW signals. The latter MW coaxial cable is connected to a semi-rigid coaxial needle-tip MW antenna inside the irradiation chamber by using vacuum proof coaxial passage. The MW needle tip and the excitation fibre-tip of dimensions of about 10μm intersect nearby the sample boundary within a plane of wafer perpendicularly to irradiation beam and compose measurement probe, while a gap between probe tips and the sample boundary is adjusted by using the probe holders attached to a 3D stage and is controlled visually through a fiberscope system.

The irradiation chamber contains two flexible bellows connected with chamber flanges. The one at the bottom is designed for vertical positioning of the sample holder combined with a closed cycle He cooler. The top one is combined with a 3D stage positioned with precision of 3 μm by step motors to locate precisely the position of the probes relative to a sample boundary and proton beam. A sample is placed on cold finger and moved into the irradiation area of the collimated proton beam with 5 mm diameter. Temperature is either kept fixed when exposure characteristics are examined during irradiation or

varied in the range of 40–300 K during trap activation energy scans by using closed cycle He cooler attached to a sample holder within the irradiation chamber. Rather high vacuum (~10^{-6} torr pressure) is necessary within irradiation chamber containing probes which is reached by using sequence of several pumps with a turbo molecular pump as a final stage of the vacuum system.

In-situ microwave probed photoconductivity setup enable to control carrier lifetime variation, which is directly associated with defect formation. Also lifetime temperature scan reveal parameters of the dominant defects just after irradiation.

6.2. Penetrative protons irradiation dependent variations of bulk lifetime

A set of wafer fragments of dimensions 20×20 mm^2 with passivated surfaces containing thermal SiO_2 and with freshly cleaved boundaries of the same (MCz grown) Si substrate was investigated to determine a defect production rate during irradiation at different temperatures. Variations of carrier decay processes under irradiation by protons of different energy in the range of 2 – 9 MeV and of beam current in the range of 0.5 – 10 nA have been investigated. Few MCz Si samples pre-irradiated by 24 GeV protons of 10^{12} cm^{-2} fluence and kept for 3 years at room temperature were also involved into investigations to clarify peculiarities of defect nucleation.

Variations of carrier decay transients with exposure time under 8 MeV protons irradiation are illustrated in Fig. 6.2. A dynamic range for detection of the linear changes in the density of excess carries within a single transient covers more than three orders of magnitude, measured by VUTEG-3 instrument. Values of the effective lifetimes varying from milliseconds to a nanosecond under irradiation fluence have been measured.

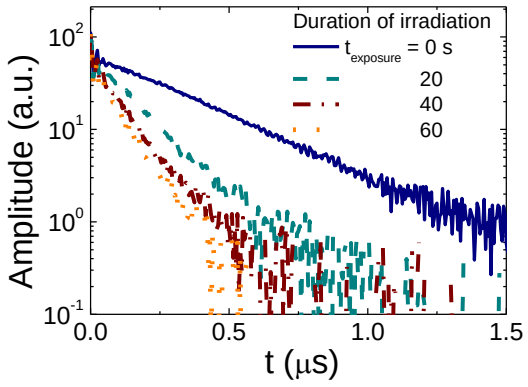

Fig.6.2. Variation of photoconductivity transients during various instants within irradiation exposure by 8 MeV protons at beam current of 4 nA.

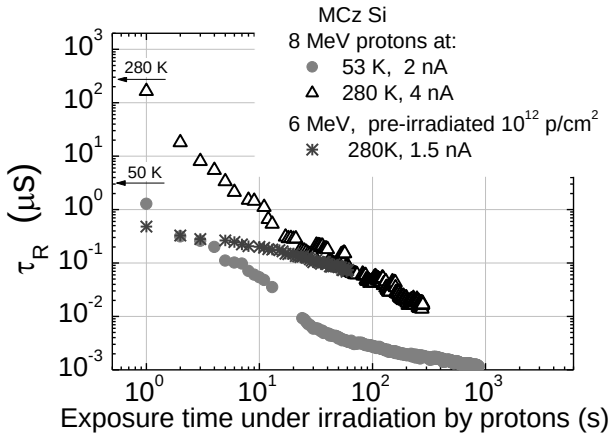

Fig. 6.3. Variation of the recombination lifetime during irradiation: by 6 MeV protons at 280K of the pre-irradiated material (star symbols), and by 8 MeV protons at 53 K (circles) and 280K (triangles) temperatures of the initial MCz Si as a function of the exposure time.

Variations of the absolute values of recombination lifetime τ_R, determined by radiation induced changes in the parameters of radiation defects (γ_R, N_R) and approximated by simple relation $\tau_R = 1/\gamma_R N_R v_T$, are illustrated in Fig. 6.3, as obtained for irradiations by penetrative 8 MeV protons. There, values of τ_R have been extracted by the analysis of the initial decay constituent, which is shorter than a partial surface recombination lifetime within well passivated wafers. Complicated changes in the recombination lifetime reduction rates with proton beam exposure duration have been revealed. This *in situ* reduction rate

depends on proton energy, on pre-irradiation of material, on temperature at which irradiation is implemented, and on other conditions. Two slopes of lifetime decreasing with irradiation time are clearly observed in Fig. 6.3, which is an indication of carrier capture cross section variation with irradiation fluence, while defects concentration is linearly dependent on irradiation time.

6.3. Spectroscopy of as-induced defects

Spectroscopy of activation energy of dominant traps has been performed before and just after irradiation. Temperature variations of the instantaneous lifetimes ascribed to the carrier trapping/generation centres are illustrated in Fig. 6.4 for the initial material samples irradiated by the 8 MeV protons. The trapping effect has been verified by asymptotic lifetime variations under additional bias illumination. There trap spectra (the $\tau_{tr\text{-}1,2}$ variations as a reciprocal function of the thermal activation energy *1/kT*) for the same material before irradiation are presented by a line for comparison.

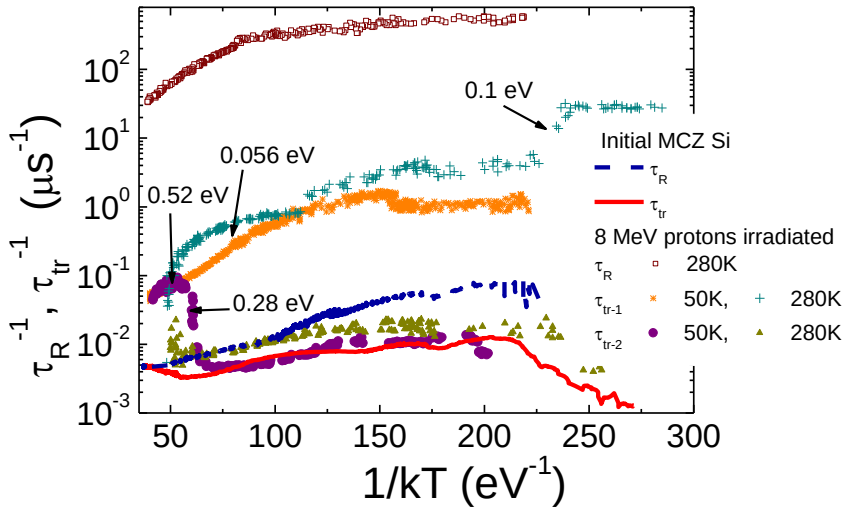

Fig. 6.4. Variation of the inverse recombination (square symbols) and trapping lifetimes of different carrier decay components as a function of the reciprocal thermal energy in MCz Si sample just irradiated with 8 MeV protons at 50 K (circles for $\tau_{r\text{-}1}$ and stars for $\tau_{r\text{-}2}$) and at 280K (triangles for $\tau_{r\text{-}1}$ and crosses for $\tau_{r\text{-}2}$) compared with trapping constituent (line) obtained in the initial material.

For material irradiated at 50 K, the activation energy of 0.056 eV for shallow trap can be separated in the spectrum (Fig. 6.4) of τ_{r-2} (ascribed to the slowest component within carrier decay transient). The intermediate decay constituent τ_{r-1} indicates a deeper trapping centre with activation energy of 0.28 eV. As it is known from the DLTS spectroscopy data in the irradiated Si [76, 79, 80], traps with activation energy of 0.28 eV are ascribed to VOH complexes or clusters. For the material irradiated at 280 K (Fig. 6.4), spectrum of τ_{r-2} approximately coincides with spectrum of traps in the initial material. In trap spectrum of the intermediate decay constituent τ_{r-1}, trapping centres with activation energy of ~ 0.1 eV and of 0.52 eV can be resolved. The first trap can be ascribed to transformed thermodonors or $C_{i,s}$ related complexes, while the deepest one (0.52 eV) is interpreted either as a cluster related trap in the nomenclature of DLTS spectroscopy [76, 80]. It is clear from a comparison of values of the trapping and recombination lifetime (Figs. 6.3 and 6.4) that the temperature scale of the observable activation of the recombination centres should be far in the range of temperatures of > 500 K. Therefore, it is nearly impossible to determine this activation energy of recombination centres from temperature scans without modification of material.

6.4. Lateral profiling of the production of radiation defects

The lateral profiling of the distribution of the hadrons as–induced radiation defects has been performed to verify homogeneity of the protons beam. Lateral variation of recombination lifetime within 20x20 mm^2 wafer fragment is illustrated in Fig. 6.5. Small part of the wafer sample area has been irradiated (as sketched in the inset of Fig. 6.5) with 5 mm spot dimension protons with fluence of $10^{13}cm^{-2}$.

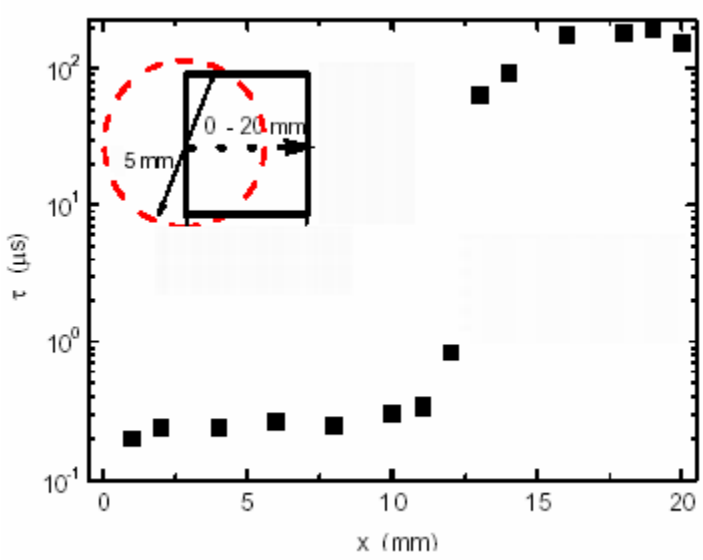

Fig. 6.5. Lateral profile of recombination lifetime distribution in MCz Si wafer irradiated by 8 MeV protons with fluence of 10^{13} cm^{-2}.

Sharp increase of recombination lifetime from 0.2-1 to 100 μs has been observed when comparing the irradiated and non-irradiated sample areas, respectively. Transitional range width between two areas is about of 1 mm as can be deduced from Fig. 6.5. A precision of sample positioning in this scanning case was of about 1 mm, due to precision of identification of the sample contour and protons beam spot location.

6.5. Modelling of the impact of radiation clusters

Variations of the recombination lifetime (τ_R), measured by the control of the initial component within carrier density decay transient, have been examined during exposure on beam of the penetrative protons. Variations of carrier lifetime during irradiation of the initial MCz Si material and pre-irradiated one (by protons with fluence of 10^{12} cm^{-2}) are compared in Fig. 6.3. Different recombination lifetime reduction rates were obtained for these samples as a function of irradiation fluence (Φ) for 6 MeV and 8 MeV protons, as can be noticed in Fig. 6.3. The more precisely measured exposure characteristic, varying the 8 MeV protons beam current, is also demonstrated in Fig. 6.6.

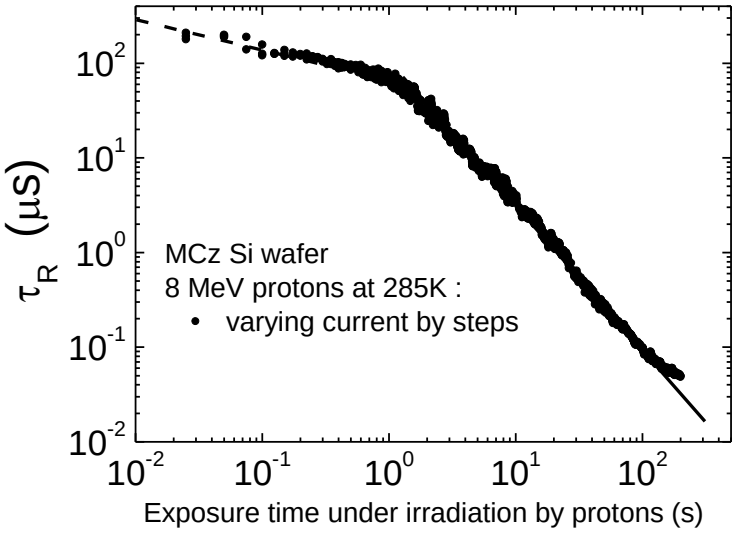

Fig. 6.6. Variation of recombination lifetime in MCz Si wafer during 8 MeV protons irradiation at 285 K temperature.

To explain the observed variations within slopes of carrier lifetime reduction rate over different samples and irradiation regimes, the impact of clusters has been modelled. Within simple approach, carrier lifetime due to recombination on clusters can be written as a function of carrier thermal velocity v_T, of geometrical cluster Cottrell sphere cross-section σ_{cl} and of the initial $N_{cl,0}$ and induced during irradiation N_{cl} density of vacancy clusters as follows:

$$\tau_{R,cluster} = \frac{1}{v_T \sigma_{cl} N_{cl}} = \frac{1}{v_T \sigma_{cl}(\Phi)(N_{cl,0} + N_{cl}(\Phi))}. \quad (6.1)$$

The cross-section σ_{cl} is assumed be fluence dependent

$$\sigma_{cl} = \sigma_0 \exp(eV_{b,cl} / kT) \quad (6.2)$$

due to barrier potential changes at cluster sphere as

$$\langle V_{b,cl}(\Phi) \rangle = \frac{kTc}{e} \ln\left[\frac{N_D}{n_i^2} \left(\sum_{n=1}^{V_n} N_A V_n \right) \right] |_{N_A \sim \Phi} = \frac{kTc}{e} \ln\left[\frac{N_D}{n_i^2} \left(\sum_{n=1}^{V_n} \frac{\partial N_{A,n}}{\partial \Phi} \Phi \right) \right]. \quad (6.3)$$

Then, density of clusters and their cross-sections are assumed to be dependent on clusters introduction rate $\partial N/\partial \Phi$ when Φ fluence is collected. For fresh samples, a slope of carrier recombination lifetime on clusters during their production can be described as a function of fluence Φ by expression:

$$\tau_{R,cluster} = \frac{1}{v_T \sigma_{cl}\left(N_{cl,0} + N_{cl}(\Phi)\right)} = \frac{1}{v_T \sigma_0 \exp\left(\ln\left[\frac{N_D}{n_i^2}\sum_{n=1}^{V_n}\frac{\partial N_{A,n}}{\partial \Phi}\Phi\right]^c\right)\left(N_{cl,0} + \frac{\partial N_{cl}(\Phi)}{\partial \Phi}\Phi\right)}$$

$$\cong \frac{1}{v_T \sigma_0 \left[\frac{N_D}{n_i^2}\sum_{n=1}^{V_n}\frac{\partial N_{A,n}}{\partial \Phi}\Phi\right]^c \left(N_{cl,0} + \frac{\partial N_{cl}(\Phi)}{\partial \Phi}\Phi\right)} \propto \frac{1}{a\Phi^c + b\Phi^{c+1}} \tag{6.4}$$

For the pre-irradiated samples, when initially radiation induced clusters may serve as nucleus for clusters growth, a slope of carrier recombination lifetime during further their production can be described by expression

$$\tau_{R,cluster} \cong \frac{1}{v_T \sigma_0 \left[\frac{N_D}{n_i^2}\sum_{n=1}^{V_n} N_{A,n}\right]^c \left(N_{cl,\,fixed\_irrad}\right)} \propto \frac{1}{b^* \Phi^1_{fixed}}. \tag{6.5}$$

These approximations (6.4) and (6.5) qualitatively fit the observed slopes (Figs. 6.3 and 6.6.) of carrier recombination lifetime changes within exposure characteristics obtained on fresh and pre-irradiated samples. The initial, close to linear, decrease of carrier recombination lifetime may be determined by prevailing of the small grown-in defects density or enhanced density of clusters, introduced by pre-irradiation of the latter samples. Also, variation of a distance L among clusters, as discussed in Ch.5.3, can be efficient.

The extended radiation defects, such as clusters along the path of particle track containing the nanometer cross-sectional dimensions, can be assumed as the inside inclusions characterized by surface recombination s_I. This s_I parameter of the inside surface recombination should depend on density of these surface states (e.g. due to dangling bonds existing at surface of nano-

pores made by multi-vacancy agglomerates), on potential barriers formed by charge neutralization in vicinity of cluster, and on activation energy of levels formed at inside surface by local destruction of crystal. Assuming that distribution of clusters is close to homogeneous in the large scale, the surface recombination lifetime $\tau_{s1} = 1/\eta_{n=1}^2 D$ is ascribed to the main surface decay mode (see Ch.3) within an one-dimensional diffusion problem with L as an averaged distance between the adjacent clusters. The invariant surface recombination velocity $s_I = const$ can be ascribed to the specific species of clusters (e.g. V_4, V_6, V_N) determined by the formation energy of nanoscopic structures. Then, an impact of the inside surface recombination on clusters is determined only by a distance $L = CN_{cl}^{-1}$ between the clusters which decreases with enhancement of density particle trajectories with exposure time $L = ct_{exp}^{-1}$ or fluence. This can be supported by TRIM simulated maps [76] of the extended defects along particle tracks, as illustrated in Fig. 6.7.

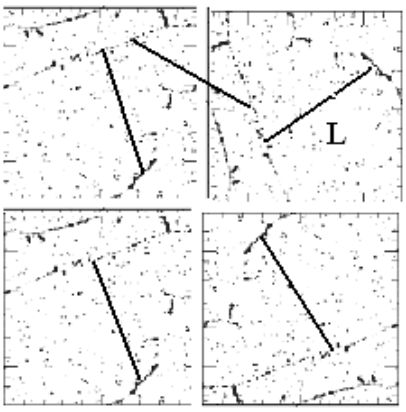

Fig. 6.7. The extended radiation defects along the path of particle tracks (after Huhtinen [76]) as the inside surfaces for recombination characterized by s_I, spaced by volume averaged distances L shown by thick lines.

The close to exponential carrier decay ($A_1 \geq 0.81$, Ch.3) appears homogeneous excitation ($\alpha d \sim 0.3$ at λ_{ex}=1062 nm) implemented in these experiments. The initial stage of excess carriers decay is characterized by the higher decay modes if surface recombination prevails. This decay component rapidly decreases with L, as $\tau_{s1} = L/s + L^2/\pi^2 D$, when density of particle paths is enhanced with exposure time or fluence of irradiation. Assuming the

$L=c_0+ct_{exp}^{-1}$ variations and by adjusting c_0 and c to get $L=d$ at t_{exp}= 0, the carrier lifetime variations as a function of L have been examined. These simulated dependences are illustrated in Fig. 6.8.

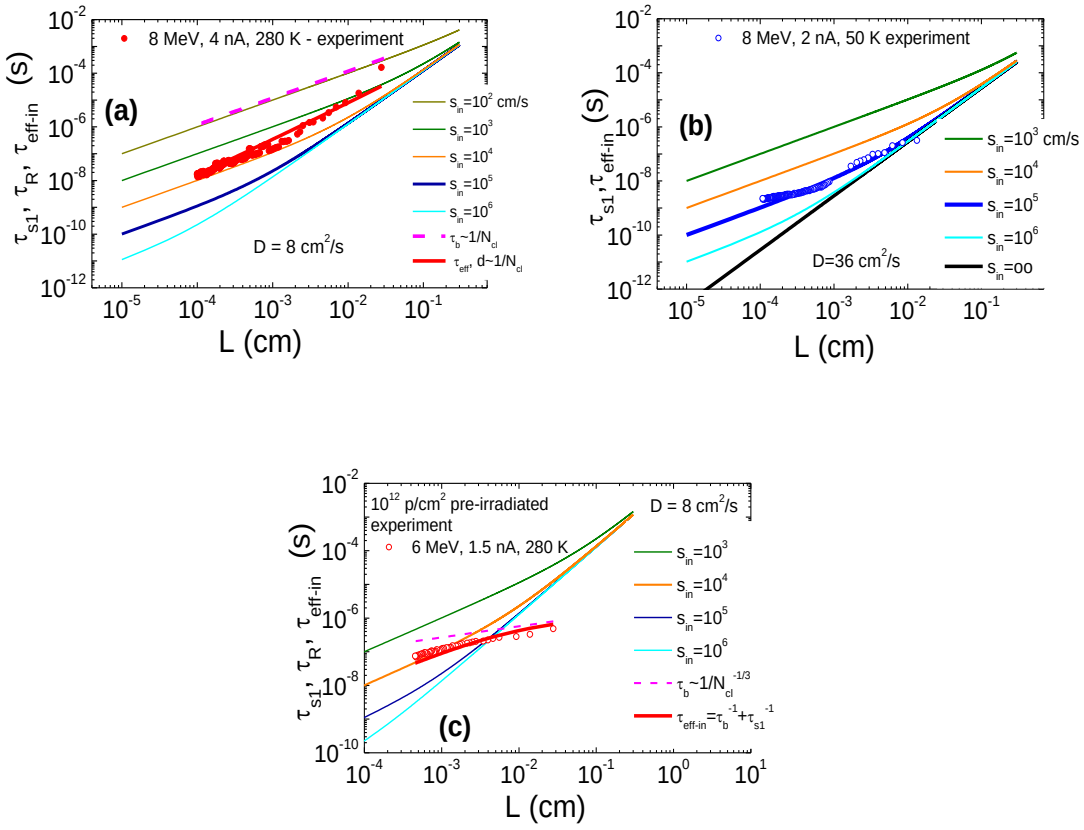

Fig. 6.8. Comparison of variations of the initial carrier decay component obtained in experiments (symbols) during irradiation by 8 MeV protons (a,b) and by 6 MeV (c) protons at temperatures of 280 K (a,c) and of 50 K (b) for the initial MCz Si (a,b) and the pre-irradiated (c) material with the simulated characteristics (lines) by using a model of simultaneous action of surface and bulk recombination and at assumption of $L\sim ct_{exp}^{-1}$.

The bulk lifetime in fresh, well surface passivated Si material (Fig. 6.8a) at elevated temperatures (280K) is longer than realistic values of surface recombination lifetimes on clusters. The measured effective lifetimes indicate a rather small surface recombination velocity s < 100 cm/s owing to surface passivation. The simulated simultaneous action of bulk (dashed line) and of surface recombination (solid lines) lifetimes are reduced with L slower than experimental values, at assumption that L and τ_b are related to exposure time by relation t_{exp}^{-1}. The minority carrier diffusion (D = 8 cm^2/s) governed

processes should be accepted to adjust these characteristics. Then, a satisfactory fit of the experimental variations of the initial decay lifetimes over the whole range of exposure for protons beam can be achieved. The most significant discrepancies are obtained within the initial stages (for the largest L) of exposure. This can be explained by the assumption that surface recombination velocity changes also, not only an averaged distance between particle tracks.

The better agreement between these measured and simulated characteristics has been obtained for data extracted at low temperature (50 K, Fig. 6.8b). Here, the main changes are governed completely by the inside surface recombination of fixed value of the surface recombination velocity. Although, the larger value of carrier diffusion coefficient (D = 36 cm^2/s) should be involved into simulations. However, an increase of carrier mobility and of diffusion coefficient can be easily predicted for low temperatures relatively to those at 280K when a phonon scattering mechanism prevails.

For the pre-irradiated samples, the fast bulk recombination processes initially dominates, with lifetimes significantly shorter than those of surface ones. Therefore, the lifetime of the carrier recombination component decreases with L during the beginning stages of irradiation exposure following of the bulk lifetime reduction (dashed line Fig. 6.8c). However, the lifetime value changes due to surface recombination after the averaged distances between particle tracks become shorter than 50 μm.

Hereby, the recombination lifetime variations during irradiation over the whole range of exposures can be simulated by the linear model of surface recombination with realistic parameters at a single assumption of $L \sim ct_{exp}^{-1}$.

The discussed above a simplified approach of a sum of the recombination probabilities can be assumed if the integral volume of the radiation induced defects can be neglected in comparison with that of the crystal. The irradiated material becomes a disordered structure when an integral volume of the radiation induced defects is comparable with that of crystal in between of the

nearest radiation defect precipitates and then, a stretched-exponent decay is specific [80, 81] due to trapping assisted diffusion / random-walk of carriers.

6.6. Evolution of near-surface recombination during protons implantation

For 300 μm thick samples 1.5 MeV protons are stopped within wafer at around of 30 μm from the face surface of the sample. The profile of 1.5 MeV protons penetration has been simulated by using the Transport of Recoils and Ions in Matter (TRIM) Monte Carlo simulation program [82]. It can be seen within simulated profile of vacancy type defects production, Fig. 6.9, that the radiation modified layer contains a pedestal and a peak at about 10% of the wafer depth. Defects distribution is inhomogeneous in the implanted sample. Therefore, a combined methodology using different excitation wavelength is applied to control both the *in situ* and post-irradiation states of the defect system, and defects evolution during implantation of protons.

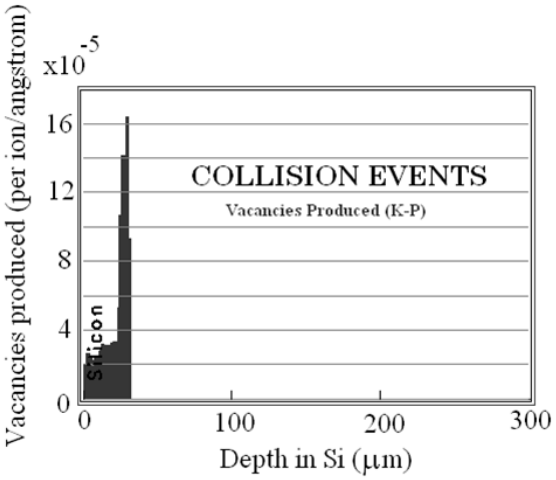

Fig. 6.9. The TRIM simulated profile of vacancy type defects depth distribution generated by 1.5 MeV protons implantation of Si 300 μm-thick wafer.

The measurements of defects evolution under protons implantation have been performed using Tandem type protons accelerator installed at the Centre of Physical and Technological Sciences in Vilnius.

To control carrier recombination lifetime within rather thin implanted layer, the *in situ* measurements were performed at surface excitation mode. This

regime was implemented by using 531 nm light pulses for which the absorption depth α^{-1} is of about of 1 μm.

Measurements are usually arranged by using several exposure steps: irradiation is stopped after certain time and measurements at bulk excitation regime (1062 nm wavelength) are then performed, to verify if surface or bulk recombination within implanted layer dominates. Also cross-sectional scans of carrier lifetime within wafer depth are performed after irradiation.

The initial steps of irradiation had been selected to be rather short. Consequently, collected fluence of protons was kept low, in order to measure the exposure characteristic more precisely. Changes of decay transients for different instants of exposure time are illustrated in Fig. 6.10. Transients measured for this implantation stage using the surface excitation regime are two componential, and amplitude of the asymptotic constituent decreases rapidly with the exposure duration. Eventually, the asymptotic constituent disappears (for t_{exp} = 750 s, Fig. 6.10c), while initial constituent of a transient becomes significantly shorter than that of the decay rate, shown in Fig. 6.10a. This result implies the formation of a two-layered structure during implantation: the asymptotic amplitude qualitatively indicates the rate of surface recombination of a single-layered structure [83, 84]. A transformation (Fig. 6.10d) of a transient to a single exponential decay shows that the bulk recombination within the front implanted layer prevails. Effective carrier lifetime measured for the homogeneous excitation regime (at 1062 nm wavelength) is affected by radiation damaged layer at the projectile range and it decreases with increasing of irradiation fluence. However, this lifetime reduction is not so fast relatively to that for the surface excitation regime.

The carrier recombination lifetime τ_{Rs} extracted from the initial carrier decay component when measured for the surface excitation regime is illustrated in Fig. 6.11, where τ_{Rs} is plotted as a function of both the irradiation exposure time t_{exp} and the proton fluence Φ. It can be seen that slower reduction rate of τ_{Rs} value with enhancement of irradiation fluence is obtained

within initial exposure episodes (t_{exp} < 10 s). The slow reduction of τ_{Rs} can be explained by the insufficient precision for the separation between the carrier decay instant lifetime and bulk recombination parameter, due to the higher surface recombination modes. The sub-linear reduction of $\tau_{Rs} \sim \Phi^{-1/2}$ has been obtained as a function of fluence Φ enhancement within a wide range (t_{exp} = 10–20000 s) of exposure times.

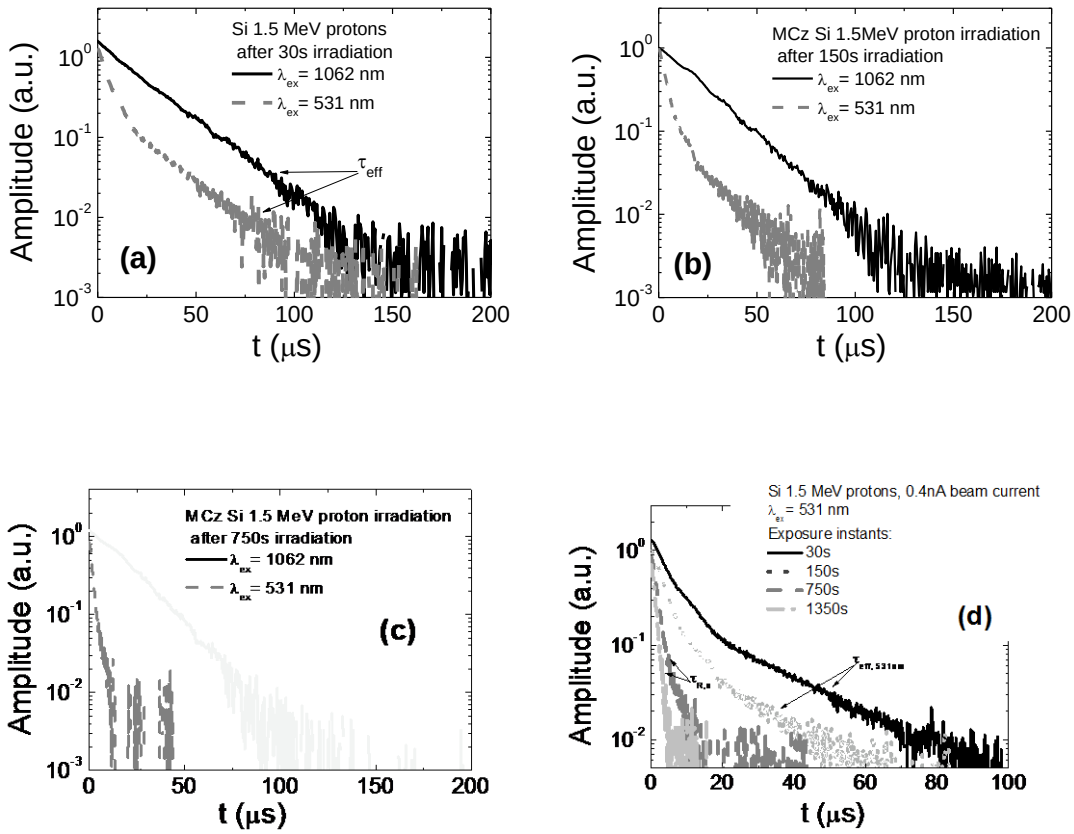

Fig. 6.10. Comparison of photoconductivity transients measured at surface and bulk excitation regime after different exposure time of protons irradiation (a) t_{exp} = 30s, (b) – 150s, (c) – 750s, and (d) – evolution of transients at surface excitation regime.

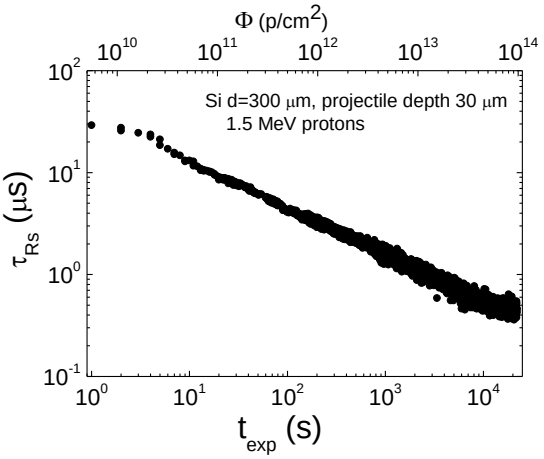

Fig. 6.11. Variation of carrier recombination lifetime during irradiation with 1.5 MeV protons, measured at surface excitation regime.

The latter fluence-dependent $\tau_{Rs}\sim \Phi^{-1/2}$ which actually averages recombination lifetime variations within the proton projectile range, can be qualitatively explained by variation of density of extended radiation defects. The increase of the radiation defect density determines a reduction of distances (L) among the defects. Due to a sharp recombination boundary for the projectile range (Fig. 6.9) of protons beam induced lateral inhomogeneity of defect density, carriers experience two directional gradients within the implanted layer. Then, the proportionality relations are derived as: $\tau_{Rs}\sim 1/N_{cl}\sim L^2\sim \Phi^{-1/2}$ under assumption that the introduction rate of the dominant defects varies linearly with fluence.

6.7. Depth-profiling of recombination defects after protons implantation

The cross-sectional scans of the carrier lifetime depth distribution were carried out after implantation to search distribution of dominant recombination centres. These measurements are performed by using VUTEG-4 instrument. The excess carriers are excited by strongly absorbed light (531 nm) pulses, to avoid the deep initial penetration of excitation light. Distribution of the evaluated carrier decay lifetime τ_{Rs} as a function of depth coordinate x, within the wafer boundary, is plotted in Fig. 6.12.

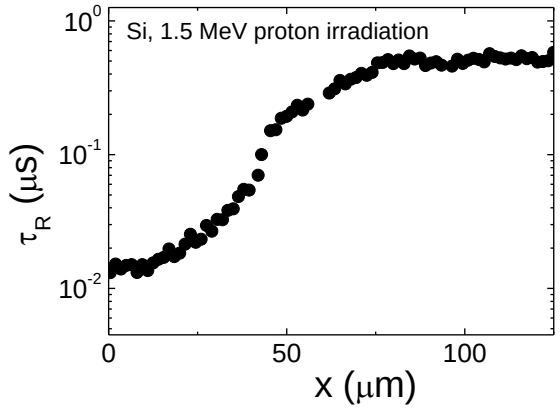

Fig. 6.12. Cross sectional profile of carrier recombination lifetime distribution within Si wafer edge after 1.5 MeV protons irradiation.

The shortest τ_{Rs} values are obtained at the front surface of the implanted wafer. These values are close or even shorter than those measured during irradiation. This result hints at the slight transformation/activation of the radiation-induced recombination centres in post-irradiation state. Actually, the narrow range of the shortest carrier decay lifetimes (τ_{Rs}) is observed at the expected position of > 30 μm within $\tau_{Rs}(x)$ profile. The discrepancy between the simulated (Fig. 6.9) and measured position (Fig. 6.12) can be explained by the experimental errors Δ due to the fibre spot diameter ($\phi \sim 6$ μm) and the defect peak dispersion (at half of its peak amplitude is ≈10 μm, Fig. 6.9), while a step of probe positioning is 2.5 μm. Thus, the maximal positioning error value is $\Delta \approx 16$ μm.

Summary of the main results described in the chapter

[A16, A17, P19-P2l]

A comprehensive instrument based on MW probed photoconductivity transients control has been designed, fabricated and approved for the remote and *in situ* monitoring of defects evolution during irradiation by protons. Various measurement regimes have been proposed and implemented in

applications of this measurement arrangement. This instrument has been installed within accelerator facilities at proton accelerators of Helsinki University and of the Centre of Physical and Technology Sciences in Vilnius.

The decrease of recombination lifetime during penetrative protons irradiation has been identified. The different rates of the production of the dominant recombination centres have been clarified. The defect production rate has been found to be dependent on irradiation temperature and on the pre-irradiation conditions of Si material. The models of cluster formation impact on the carrier lifetime reduction rate during irradiation and of surface recombination on cluster boundary have been proposed. These models have been employed to prove the prevailing of the radiation induced cluster defects, acting as the dominant carrier recombination centres, while cluster surrounding space charge sphere determines carrier trapping effects. The activation energy of carrier trapping centres has been extracted by using temperature scans of the asymptotic decay lifetimes. The changes of the effective lifetimes of the initial and asymptotic decays components imply the complicated transformations of radiation defects during irradiation.

It has been demonstrated that lateral and depth-dependent carrier lifetime profiling reproduce rather well the proton beam spot contour and stopping range of the implanted protons, respectively.

The fluence-dependent $\tau_{Rs} \sim \Phi^{-1/2}$ carrier lifetime variations have been revealed under stopped protons implantation, when τ_{Rs} actually averages carrier lifetime variations within the proton projectile range, and explained by variation of density of extended radiation defects. The increase of the radiation defect density determines a reduction of distances (L) among the defects, and it leads to the proportionality relations as: $\tau_{Rs} \sim 1/N_{cl} \sim L^2 \sim \Phi^{-1/2}$ under assumption that the introduction rate of the dominant defects varies linearly with fluence.

VII. Doping, strain and irradiations dependent characteristics in Si-Ge

Material properties in device layers strongly depend on recombination characteristic changes under technological procedures of doping, epitaxial growth, implantation etc., due to native defects formation. In this chapter, investigations of carrier recombination characteristics changes in heavily doped Si-Ge materials and layered structures are described.

7.1. Samples and structures investigated

One batch of the investigated materials comprised the Si substrates containing high mobility layers, based on strained silicon. A thin, about of 10 nm thick strain Si layer (SSi) was grown on 300 or 400 nm strain-relaxed $Si_{1-x}Ge_x$ buffer (SRB), where concentration of Ge is ~ 22 %. Also, thin carbon doped layer is formed within SRB layer to provide nucleation site for dislocations. All the composition of layers was grown on substrate of 300 μm thick Cz Si. The layered structure of samples is shown in Fig. 7.1a. An image of strained layer, made by transmission electron microscopy, is shown in Fig. 7.1b. Two sets of samples with high mobility substrate were investigated.

The first one consisted of structures with metallized shallow junction diodes, fabricated by utilizing the 8 nm strained Si (SSi) grown on SRB layer and junction of p+/n and n+/p were fabricated by standard implantations. Dopant activation was achieved by conventional spike annealing at 1000 ^{o}C. Also nickel silicidation was used to lower the contact resistance. A junction depth (d_j) of 50 nm was derived from process simulation and secondary ion mass spectrometry (SIMS). These structures were investigated by MW-PC transients technique employing three excitation wavelengths, namely 350, 532 and 1064 nm, in order to reveal the lifetime of the near-surface virtual substrate and of the strained layer.

The second set of samples consisted of the same, but non-metallized layers of SSi on SiGe SRB, containing different dislocation densities. The MW-PC transients and diffraction efficiency characteristics of dynamic light induced

refelection gratings (DRG) [85] were examined on the latter set of samples. The structure of dislocations disorder of the integrally mirror-like top layer was evaluated imaging surface of the non-metallized SSi layers.

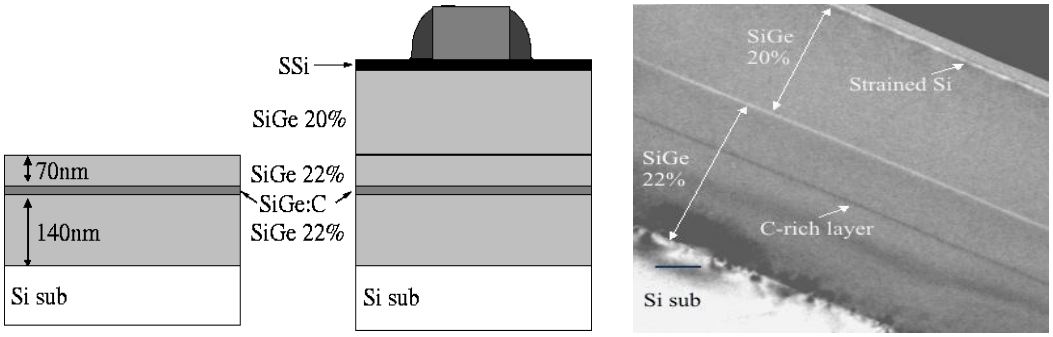

(a) (b)

Fig. 7.1. Structure of investigated samples (a), and (b) an image of strained layer made by transmission electron microscopy, after [86].

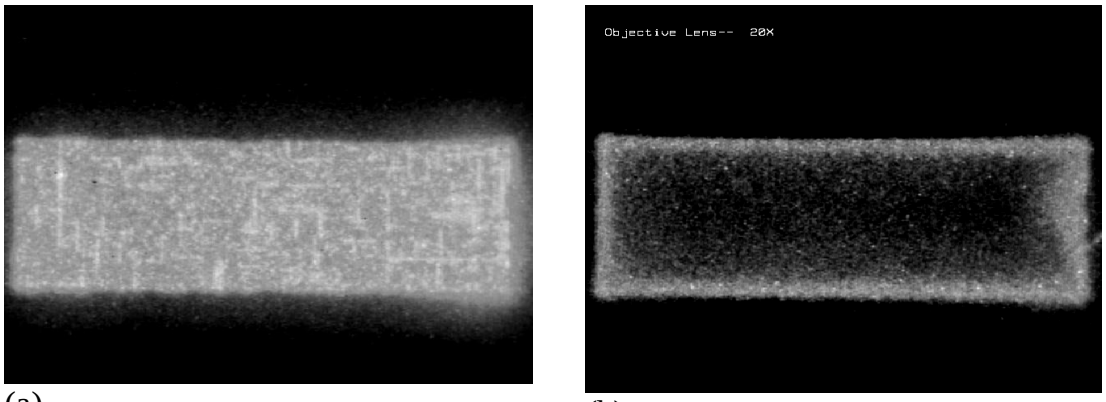

(a) (b)

Fig. 7.2. EMMI images of wafer fragments of 10^5 μm^2 area in 300 nm SRB (a), and (b) substrate Si, after [86].

An image of the emission microscopy (EMMI) obtained on the 300 nm SRB of the non-metallized SSi wafer [86] is illustrated in Fig.7.2a, where a lateral projection of the dislocation net can be observed, implying formation of the disordered structure of the fractal type, relatively to that of perfect Si crystal substrate (Fig.7.2b).

Table 7.1. Dislocation densities calculated from the etch-pits in the non-metallized SRB samples.

Sample	*TDs*	*PUDs*	*MDs*
D07	3E+06	2000	0
D08	1E+07	200	0
D09	>1E+09	n/a	n/a
D10	1 E+07	200	100

The threading and misfit dislocations can be recognized as the minute details in the SRBs in EMMI image (Fig. 7.2) those form a macroscopic net. The characteristic densities of threading (TD), pile –up dislocations (PUD) and misfit (MD) dislocations are listed in Table 7.1 for non-metallized samples.

Another batch of investigated materials contained two sets of germanium samples. First set of Ge samples was devoted to investigation of deep level after implantation of different metals as Ti, Cr, Fe, Co and Ni. The samples of 175 μm thick wafer pieces of the Cz grown n-type Sb doped 33 – 38 Ωcm resistivity Ge material have been examined to reveal the metallic contamination impact on properties of Ge and on their modification after temperature treatment. Samples have been annealed for 1 – 60 min at 350 – 700 ^{o}C temperature after implantation by energy of 90 keV for two implantation fluences 5×10^{13} and 5×10^{14} cm^{-2}. A peak of implants density in the range of 4×10^{18} – 5×10^{20} cm^{-3} was concentrated at 43 nm depth as deduced from the SIMS profiling (Fig.7.3). Investigated samples were passivated by iodine containing varnish to diminish an influence of mechanically induced surface defects. Carrier decay MW-PC transients have been measured to evaluate the influence of different species of metals implantation to minority carrier lifetime. Also, time resolved photo-ionization spectroscopy measurements have been performed to identify electrical parameters of prevailing deep levels.

The third batch of Ge samples contained the Cz and FZ grown Ge wafers obtained from different vendors. Samples of different thickness, surface treatment and geometry have been investigated in order to reveal surface recombination peculiarities, more detail parameters are listed in Table 7.2.

Also, Ge materials of different conductivity type and resistivity, varying in the range of 0.01 to 40 Ωcm, have been examined to reveal minority carrier lifetime peculiarities with doping concentration. Latter parameter, measured at low excitation regime, differ from SRH model at high doping region.

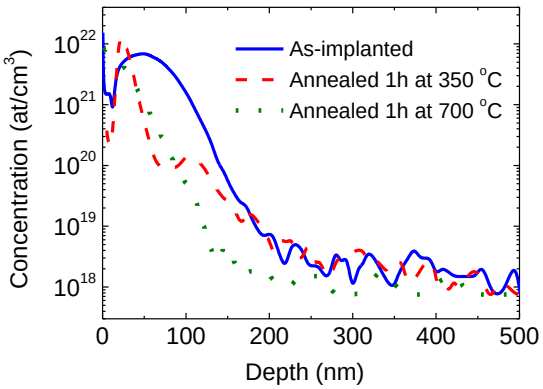

Fig. 7.3. SIMS profile of Ni distribution in Ge sample after Ni implantation of 5×10^{20} cm^{-3} concentration and after annealing for 1h at 350 °C or 700 °C.

Table 7.2. Characteristics of Ge samples containing different doping

Samples	Cz p-Ge & n-Ge	Cz p-Ge	FZ p-Ge	Cz p-Ge	optical-grade
Resistivity (Ω cm)	p: 28, 22 & 0.01 n: 37, 21 & 0.15	35, 19, 0.4, 0.1 & 0.07	40	3	
Thickness (mm)	0.175 & 0.55	2-4 & wedge	0.1-8	3×5×20	3
Surface preparation	polished & passivated	grinded & polished	cleaved & polished	Polished	Anti-refl. coat.
Structure	wafer	wafer	wafer		Ge IR filter & AGA lens

The fourth batch of samples contained three sets of n-type Cz grown Si diodes, two of them with Ge doping concentrations of about 10^{19} cm^{-3} (GCz) and 10^{20} cm^{-3} (GGCz) and the third one without Ge doping (Cz).

7.2. Strain determined characteristics in Si-Ge structures

Formation of the strained silicon layers on a strain-relaxed SiGe buffer (SRB) is one of the modern techniques to enhance the carrier mobility for the strongly reduced channel lengths in advanced nano-electronics devices [87]. However, relaxation of the SRB also results in creation of the threading and misfit dislocations chaotic networks. Therefore, the issue of the significant impact of dislocations on the carrier recombination and transport properties remains of concern, when dislocations may cause a disordered structure with the specific carrier trapping and asymmetric diffusion phenomena.

The microwave probed photoconductivity (MW-PC) transients measured in the 250/350 nm SRB samples containing p^+/n junctions are illustrated in Fig. 7.4, and qualitatively the same character of carrier decay variations have been determined in both p^+/n and n^+/p junctions. The decays are clearly two-componential for 532 and 355 nm wavelength excitation, while the bulk-excitation transient contains only a very small transitional constituent or it is single-componential. The asymptotic decay rate is nearly the same at bulk and near-surface excitation, which indicates the surface recombination regime in the SRB-Si substrate structure. However, the asymptotic decay shape transforms to the hyperbolic-like one at ultraviolet (UV) excitation, when the photo response comes from the top SRB layers. The asymptotic constituent in the latter case is clearly longer relatively to those for bulk and of near-surface excitation regimes. A longer transient relaxation is observed at the short wavelength excitation in the p-well structure compared with the n-well structure. The initial component of the excess carrier decay at UV excitation manifests the rate of recombination processes of the top layers of the investigated structures. The effective carrier lifetimes evaluated from this component in the metalized structures are listed in Table 7.3. These values are in the nanosecond time scale and slightly depend on the top SRB layer thickness (different in D16 and D12 groups) and on doping type of a well.

Table 7.3. Effective lifetimes attributed to the top structure of the metallized samples, measured at UV excitation.

Sample	Thickness (nm)	Well	τ_{in} (ns)
D16	350	n	27 – 170
D12	250	n	80 – 270
D16	350	p	300 – 530
D12	250	p	600 – 900

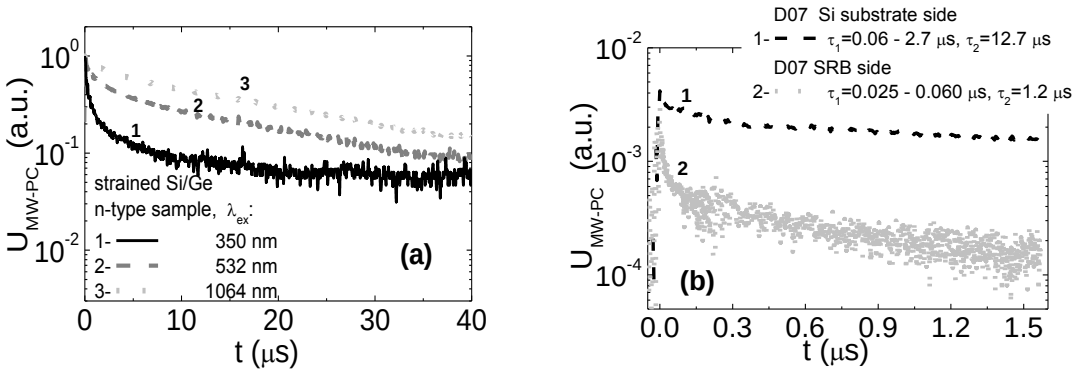

Fig. 7.4. MW-PC transients in layered structure fabricated on a 350 nm SRB wafer, varying wavelength of excitation (a). Comparison of MW-PC relaxation in Si substrate with that obtained in SRB layer, measured after 355 nm wavelength excitation (b).

Investigations of the non-metallized wafers (second set) were concentrated by exploiting the regime of the UV excitation. The MW-PC transients recorded at the same 30 ps-pulsed excitation intensity are illustrated in Fig. 7.4b for the sample D07, comparing the decays obtained for the substrate surface (curve 1) and the top SRB layer (curve 2). The decay shapes differ for SRB and Si surfaces. The small initial component can be explained by considering that the excess carrier density caused a modulation of the Debye length of the surface states on bare Si. However, the MW-PC transient integrated over the SRB layers acquires the hyperbolic shape. This indicates a stretched-exponential relaxation process inherent for disordered structures. The initial and asymptotic decay effective lifetimes, and relative amplitudes of these components vary with excitation intensity, as shown in Fig. 7.5. The effective decay rate in the Si substrate is nearly independent of the UV excitation intensity (curves 1 and

2). In contrast, the initial decay lifetime for the SRB layer decreases with increasing excitation intensity, but the relative amplitude and effective lifetime of the asymptotic decay are increased with excitation density and become longer (curves 5 to 3 of Fig. 7.5) than those for the Si substrate. Those observations can be also understood by diffusion limited carrier trapping process within disordered structure, when carrier motion is realized through random-walk of free carriers. The enhancement of photo-excited carriers density leads to an increase of the density of trapped carriers and to the consequent increase of the measured MW-PC signal within rearward part (ascribed to the dominant trapping process) of the transient. Existence of high density of dislocations can be a reason in formation of disordered structure.

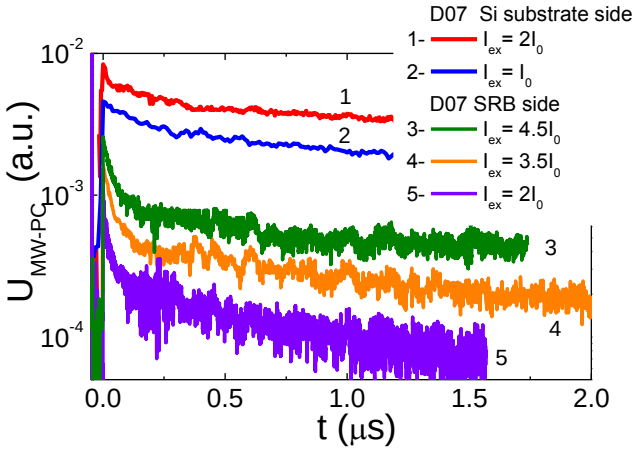

Fig. 7.5. Variations of MW-PC transients with excitation intensity.

The reciprocal recombination lifetimes as a function of dislocations density (N_{DD}) are presented in Fig. 7.6 for the as-grown SRBs. It can be seen that threading dislocations serve as recombination centres, and recombination lifetime decreases with their density. The density of dislocations attributed to recombination centres can be estimated as $N_D = N_{DD}/C$ [88], where C is the spacing between the broken bonds in a dislocation. This density N_D is hereby evaluated to be equivalent to $4\times10^{13} - 2\times10^{16}$ cm^{-3} for dislocation densities $N_{DD} = 2\times10^{6} - 10^{9}$ cm^{-2}. Assuming an effective cross- section being of the order of 10^{-15} cm^2 [88], the value of microscopic recombination lifetime $\tau_{R\infty}$, attributed

to high injection level, is estimated to be in the range of 0.005– 2.5 μs at room temperature. This estimation is in good agreement with the effective lifetimes measured by MW-PC technique in the initial decay stages. However, the hyperbolic like asymptotic decay implies multi-trapping effects in the disordered structure.

The influence of the multi-trapping is mostly inherent for the asymptotic decay, after significant concentrations of excess carriers are captured into trapping levels attributed to threading dislocations. Since a cross–section for carriers capture and activation energy of these traps depend on their occupation and varies during relaxation of the excess carriers, the distribution of the traps within Cottrell sphere of a dislocation cluster is random. The multi-trapping process seems to be more ductile to slower carrier diffusive transport in the disordered structure caused by dislocations. In the case of competing recombination and trapping processes, the excess carrier decay is characterized by instantaneous lifetimes τ_{inst}, expressed through a trapping coefficient K_{tr} as $\tau_{inst} = \tau_{R\infty}K_{tr}(\tau_{tr})$, see Ch.3 A simplified estimation of K_{tr} can be made by extrapolating $\tau_{R\infty}$ and taking the ratio $\tau_{inst}/\tau_{R\infty}$. The extracted K_{tr} values were found to be rather large, K_{tr} >10.

The recombination and transport rates were also examined by employing the photo-induced dynamic reflection grating technique (DRG) [85] which enable us to resolve gratings erasure effective times τ_{ge} measured by varying discretely the grating spacing in the range of Λ = 2 – 19 μm. Values of τ_{ge} were found to be in the time scale of 700–1500 ps for grating periods in the range of Λ = 2 – 19 μm. Then, the effective recombination lifetime is $\tau_{eff} = 2\tau_{ge}$, and its values, being of the order of magnitude 2 – 3 ns, correlate well with the time scale of the initial stages in the MW-PC transients. The reflection grating erasure times in different samples as a function of $\Lambda^2/4\pi^2$ are plotted in Fig. 7.7. Variation of the estimated grating erasure times with grating period is relatively slow. Thus, in can be inferred that the recombination processes dominate in the grating erasure rate in agreement with MW-PC results.

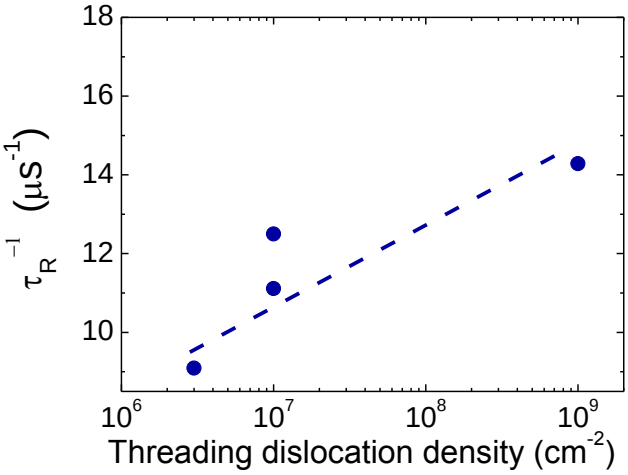

Fig. 7.6. Variation of the reciprocal recombination lifetime as a function of density of the threading dislocations in SRB layers.

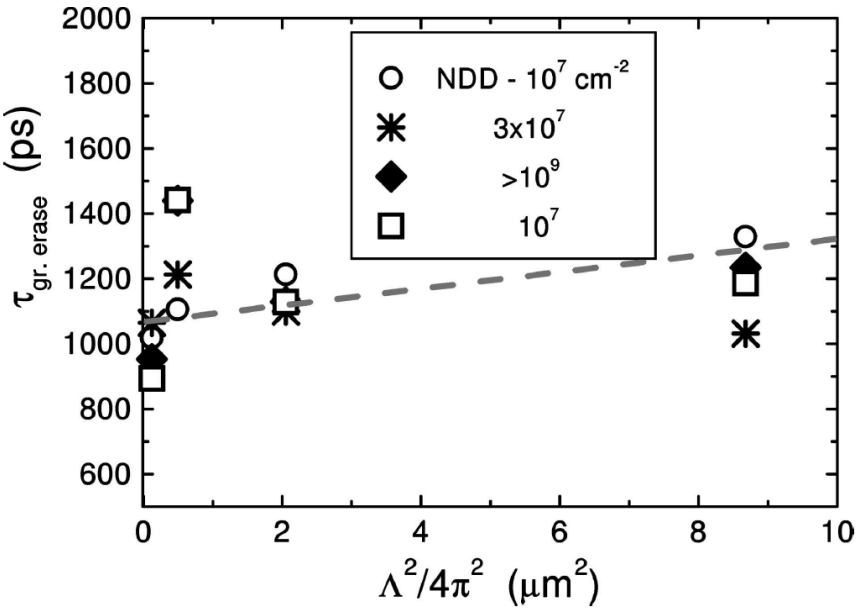

Fig. 7.7. Variation of reflection dynamic grating erasure time in SRB layers containing different dislocation density.

In addition, the diffusion constituent in the grating erasure does not exceed the range of the experimental dispersion of the τ_{ge} values. The carrier ambipolar diffusion coefficient $D_a \leq 0.13$ cm^2/s can be only estimated from these $\tau_{ge} = f(\Lambda^2)$ plots in Fig. 7.7. The estimated D_a value is less than that for crystalline Si and Ge, at least by an order of magnitude (e.g. $D_a \approx 16$ cm^2/s in Si). Dislocations can be supposed to be screened at high excitation level, while

small D_a values <<1 cm^2/s, inherent for amorphous materials [89], can be explained by the disorder of dislocations network. Thus, even in the case of the moderate dislocations density, when distances between dislocations are ≤ 6 μm, the crystalline carrier motion concept is hardly acceptable, since the distribution of dislocations is inhomogeneous. Thus, the DRG characteristics imply that the role of the diffusion in excess carriers decay is relatively small in the dislocation-rich SRB layers.

The combined techniques for recording the MW-PC and DRG transients for contactless measurements of carrier recombination, trapping and transport parameters appeared to be a consistent tool to resolve and to separate the recombination and trapping processes within complicated layered structures with inherent disorder features.

7.3. Surface recombination characteristics in Ge

Germanium layers are used in advanced silicon devices to take advantage of the high carrier mobility. Therefore, it is important to determine the recombination lifetime variations in different resistivity and various technology germanium for the design of novel structures based on the use of Ge.

To examine role of surface preparation and parameters of surface recombination, samples of different geometry (wafers, wedge bars, convex lens), thicknesses (0.1 – 8 mm) and surface state (cleaved, grounded, polished, passivating coatings covered) from the third batch of Ge substrates were investigated. To monitor lifetime variations with doping concentration, n- and p-type Ge material of resistivity from 0.01 to 40 Ωcm was studied.

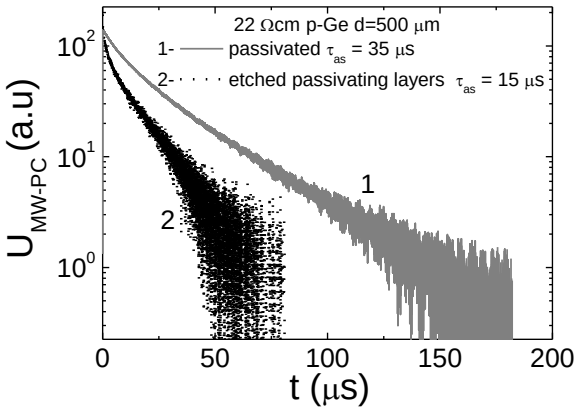

Fig. 7.8. Comparison of MW-PC transients for the passivated and etched samples of the same Ge ingot.

An influence of the surface recombination is unavoidable even in the iodine varnish passivated samples, as shown in Fig. 7.8. An initial fast component can be observed within the carrier decays, which is attributed to the processes caused by surface recombination higher modes (discussed in Ch.3). Asymptotic lifetimes differ for the passivated and the etched samples due to difference in surface recombination velocity (*s*). Values of *s* increase with worsening surface passivation (sp) state when comparing grinded (g), freshly cleaved (c) and polished (pl) surfaces of the same material and sample in such a qualitative sequence: $s_{sp}<s_c<s_{pl}<s_g$. Surface recombination has influence on the effective carrier decay lifetime up to moderately doped material.

Variations of carrier decay transients recorded varying thickness are illustrated in Fig. 7.9a. The effective lifetime as a function of sample thickness in n- and p-type Ge passivated and grinded samples is plotted in Fig. 7.9b. The effective lifetime τ_{eff} of the main decay mode can be approximated by relation $\tau_{eff} = [1/\tau_b + 1/(\tau_s + \tau_D)]^{-1}$, resulted by bulk τ_b and surface components. The latter component is determined by diffusion $\tau_D = d_{eff}^2/\pi^2 D$ and recombination on surface $\tau_s = d_{eff}/s$ constituents. Surface recombination is dominant for the bare surface and moderately doped samples, therefore a smaller slope being

proportional to *1/s* is observed within $\tau_{eff} = f(d_{eff})$ characteristics when comparing those to that obtained for the surface passivated samples.

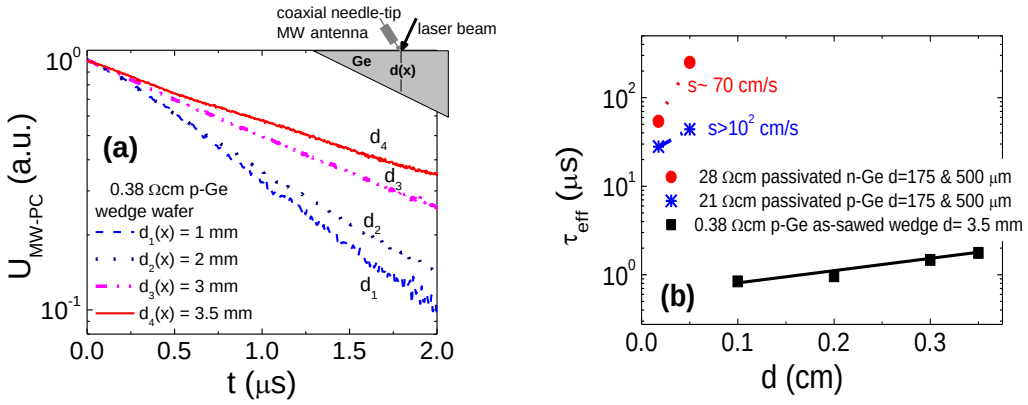

Fig. 7.9. MW-PC transient variation with sample thickness (a), and evaluation of surface velocity in different resistivity of n- and p- type Ge samples (b).

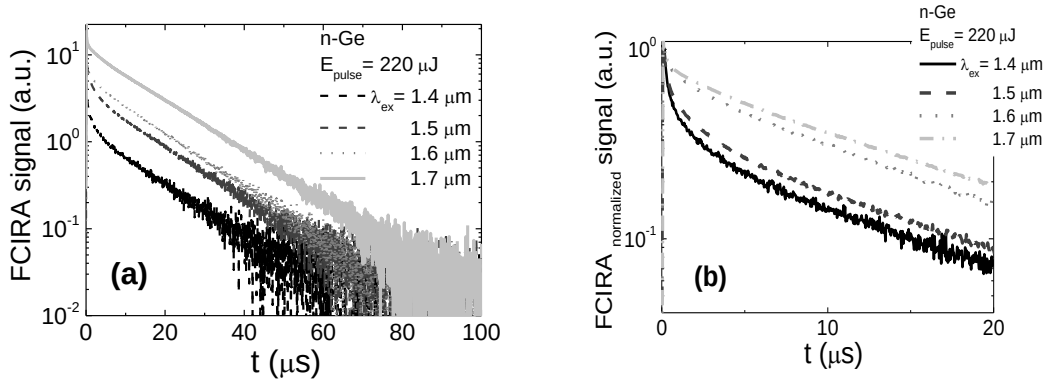

Fig. 7.10. Excitation wavelength dependent variations of FCIRA transients in a 1500 μm thick n-Ge wafer illustrating the effect of surface recombination (a) and normalized decay amplitudes (b).

Surface recombination velocity can be the carrier density dependent quantity, similarly like the bulk lifetime determined by single type levels within Shockley-Read-Hall (S-R-H) model [21]. To examine features of surface recombination in the range of high excitation levels, the free-carrier

infrared absorption (FCIRA) technique is preferential. Complementarily, analysis of variations of the normalized amplitude of the main decay mode within a system of distributed parameters (see Ch.3) can be more precise in evaluation of the surface recombination velocity. The mentioned experimental arrangement using optical parametric oscillator (OPO) as a tuneable light source of excitation wavelengths combined with control of the amplitude of the main decay mode has been implemented in this work to additionally examine surface recombination in Ge. Evaluation of the impact of the surface recombination in Ge at high excitation densities is an auxiliary task in evaluation of parameters of the non-linear recombination in Ge. For instance, parameters of the Auger type recombination had been determined in Ge with insufficient precision for practical applications in design of power Ge devices.

Free carrier infrared absorption measurements have been performed in high resistivity passivated Ge varying excitation wavelength in the range of 1.2 – 3 μm. Absorption coefficient in Ge decreases from 10^4 to 10^{-2} cm^{-1} within this wavelength region. Therefore distribution of the photo-excited carriers is inhomogeneous for the rather thick sample under test, especially for the shorter wavelengths. The surfaces of the Ge samples were passivated by iodine varnish but, the impact of surface recombination is still clearly observable (Fig. 7.10) when inhomogeneous excitation is applied at wavelengths, shorter than 1.8 μm. A specific feature of the surface recombination manifestation in FCIRA transients is the decrease of the amplitude of the main carrier decay mode within the asymptotic component with shortening of excitation wavelength [14]. The impact of excitation density is verified by control of the effective decay rate within asymptotic part of the transient. It can be easily seen in Fig. 7.10, that this asymptotic decay appears to be invariant and approximately independent of excitation density, determined by varied absorption coefficient when the same excitation light flux is kept. Thereby, validity of the methodology using the graphical analysis of A_1- sd/D (Ch.3) dependence for different values of αd is ensured. Then changes of A_1 are due to fast and

significant reduction of excess carriers during the initial carrier decay component, caused by a very inhomogeneous initial carrier distribution profile. This is smoothened by surface recombination while the carrier distribution depth-profile covers all over the sample thickness. Increasing the excitation wavelength homogenizes the excess carrier distribution profile across the sample thickness, and the amplitude of the initial decay component significantly decreases relatively to the asymptotic component leading to a single exponential decay. This can be deduced from Fig.7.10 for transient recorded at 1.7 μm excitation wavelength when comparing it to FCIRA transients recorded at shorter excitation wavelengths.

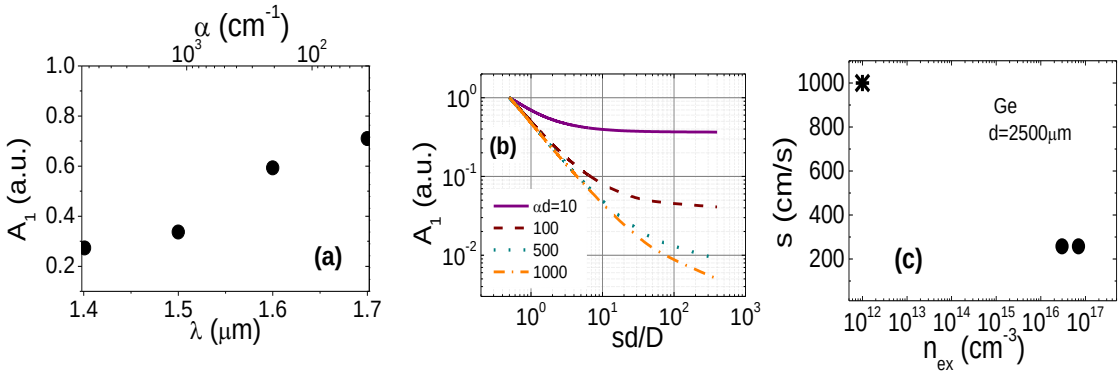

Fig. 7.11. A sketch of methodology for extraction of the surface recombination velocity which includes measurements of A_1-αd (a) to verify reduction caused by narrowing the domain of the initial carrier distribution and the graphical association of $A_1|_{\alpha d}$ to sd/D (b), to get sd/D value. Then, s value is calculated using sample thickness d and carrier ambipolar diffusion D quantities evaluated independently or taken from literature data. Values of s obtained by FCIRA technique at high excitation density can be compared with those measured by MW-PC at low excitation density (c).

A methodical procedure of extraction of value of the surface recombination velocity s is sketched in Fig. 7.11. Value of s= 300 cm/s has been obtained by this analysis for high excitation density. This is considerably smaller than that s=10^3 cm/s extracted at low excitation density measured by MW-PC technique on the same material samples (Fig. 7.9b) of thickness in the range of 2 – 5 mm with identical surface preparation conditions. This means that surface

recombination is controlled by filling of surface recombination centres. Such a result is appropriate for examination of non-linear recombination processes, as surface recombination can drastically change the initial decay component. Surface passivation and enhancement of sample thickness are the alternative means to reduce a role of surface in the investigations of non-linear recombination processes.

7.4. Auger recombination parameters in Ge

Auger recombination is a limiting factor for the carrier bulk lifetime, diffusion length values in materials that determine the operational characteristics of semiconductor devices.

Experiments which are designed to evaluate Auger recombination parameters should satisfy high excitation (n_{ex}~10^{19} cm^{-3}) condition because Auger process is three particle interaction event, therefore, it strongly depends on free carrier concentration and manifests at high free carrier density. Also excitation homogeneity is essential in order to avoid carrier surface recombination and other non-linear carrier density decay effects. There are two possibilities of experiment setup for Auger parameters evaluation: i) varying sample conductivity or ii) excitation density. Measurements made on set of samples with varying doping level [90] are complicated due to simultaneous change in the density of the recombination defects [91]. Therefore, it is difficult to separate the bulk lifetime changes due to defects and the Auger processes. Optical techniques are also complicated due to carrier diffusion and other non-linearities [92-94] caused by inhomogeneous excitation, especially of Ge material due to lack of high intensity laser source at 1.8 μm wavelength. Experiments based on contacting methods to record photoconductivity dynamics [95-97], require pure materials and perfect electrodes in order to be able to create an extremely high density of carriers and to get resolvable changes in effective bulk carrier decay lifetimes.

In this work, a transient technique based on infrared absorption (FCIRA) by free carriers has been applied to clarify the processes of non-linear Auger recombination and to extract more precisely values of the Auger recombination coefficient $\gamma_{A,Ge}$. Excitation wavelengths in the range from 1.2 to 2.5 μm were applied using 100 fs laser pulses generated by an optical parametric oscillator to reduce inhomogeneity effects. A set of samples of the Czochralski (Cz) grown 35 – 26 Ωcm resistivity with thicknesses varying from 150 to 5000 μm have been examined using the same experimental conditions to clarify the role of inhomogeneities and to eliminate their impact.

For extraction of the Auger recombination parameters, the impact of surface recombination should be minimized. Therefore, the analysis of Auger recombination parameters has been performed by examination of FCIRA transients measured for excitation wavelengths well above 1.8 μm. According to literature data [67, 98], the absorption depth approaches 1.4 mm in Ge for excitation wavelengths above 1.8 μm, therefore quasi-homogeneous excitation then can be assumed.

The excitation intensity dependent FCIRA transients at quasi-homogeneous excitation at 1.8 μm wavelength have been used for a rough estimation of the order of magnitude of the Auger recombination coefficient. The instantaneous lifetimes (τ_{in}) within the initial transient segment can be used for that purpose. The extracted values of the reciprocal lifetime τ_{in}^{-1}, attributed to Auger recombination, as a function of a square of the initial excess carrier density (n_0^2) are shown in Fig.7.12a. A linear approximation of this $\tau_{in}^{-1} = f(n_0^2)$ characteristic leads to a first estimate of $\gamma_{A,Ge} \approx 2\times10^{-31}$ cm^6/s, which is very close to that in Si.

The excitation density dependent variation of FCIRA transients in the n-Ge wafer are shown in Fig. 7.12b for a 1.8 μm wavelength, after corrections due to excitation inhomogeneity, by using the discussed in Ch.3 relation (3.5), as

$$\Delta\alpha_{FC}(t) = \frac{1}{d}\ln\frac{1}{[1-\frac{\Delta I_{FC}(t)}{I_{tr,pr}(\Delta\alpha=0)}]}. \qquad (7.1)$$

These transients have been simulated by using a solution (3.7) for Auger and linear recombination, simultaneously acting to decrease carrier density

$$n(t) = \frac{n_0 e^{-t/\tau_R}}{\sqrt{1+\frac{1}{2}\gamma n_0^2 \tau_R (1-e^{-2t/\tau_R})}}. \qquad (7.2)$$

Auger recombination coefficient is the only free parameter in these simulations, while values of n_0 and of τ_R are obtained from analysis of the absorption and linear recombination (Ch.7.3) characteristics and from calibration measurements. The solid lines in Fig. 7.12b show the simulated transients.

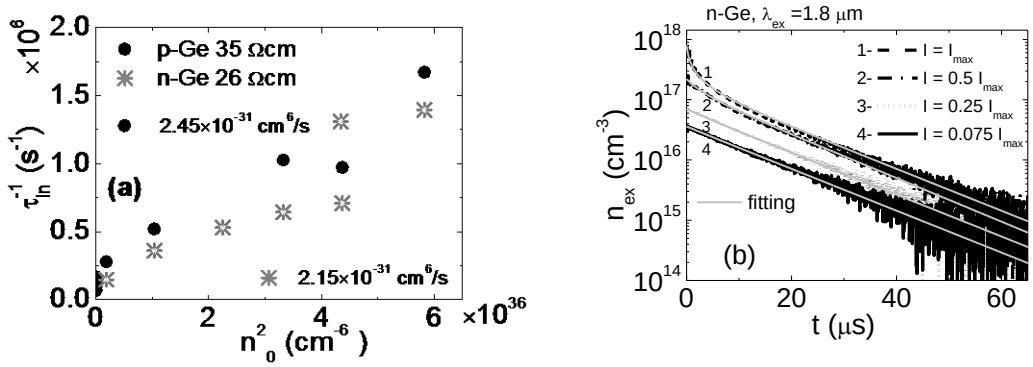

Fig. 7.12. a- Reciprocal instantaneous lifetime τ_{in}^{-1}, associated with Auger recombination, as a function of the square of the initial excess carrier density (n_0^2). The latter n_0 quantity was determined from the calibration measurements of the excitation energy per pulse, per excitation spot area and of the absorption coefficient for each excitation wavelength. b- The simulated curves were obtained using Eqs. 7.1 and 7.2 to fit the FCIRA transients measured on the n-Ge wafer for quasi-homogeneous excitation using a 1.8 μm wavelength probing beam with varying excitation intensity.

The experimental transients were fitted using the same set of γ_A and τ_R values and varying the n_0 densities in agreement with the excitation energy per 100 fs pulse. Using this approach, a value of γ_A is extracted from a whole set of FCIRA transients. Based on the fits illustrated in Fig. 7.12b, a value $\gamma_{A,Ge}$= (8±3)×10^{-31} cm^6/s is obtained. The uncertainty due to the spectral width of the laser-OPO 100 fs pulse is included in the calculation. The obtained $\gamma_{A,Ge}$ value

exceeds that obtained directly from the effective decay lifetime associated with the initial component of the FCIRA transient, Fig.7.12a, using a rough estimation method. Thus, combined fitting procedure using a dynamic range of excitation densities covering range of more that an order of magnitude enable to increase precision within extraction of the $\gamma_{A,Ge}$ value.

7.5. Doping dependent bulk recombination characteristics in Ge

Values of the effective (asymptotic) lifetimes significantly vary with excitation density, as illustrated in Fig. 7.13. MW-PC transient at low excitation is compared with those measured by contact photoconductivity (CPC) technique, varying excitation density on the same, moderately doped sample. The CPC technique is considerably more sensitive relatively to the contactless techniques. Therefore, the photo-conductivity signals can be registered at the lower excitation density values. At the lowest excitation densities of pure material, the τ_{eff} slightly decreases with additional broad-band steady-state illumination, and this implies existence of recombination and trapping centres. In moderately doped material τ_{eff} increases with excitation density, as illustrated in Fig 7.13. This increase can be explained by recombination centres (of density M) filling effect [59], when excess carrier concentration approaches or exceeds M. Value of M, estimated for 3 Ωcm p-Ge by utilizing averaged excitation density for appearance of trap filling, is found to be $M \geq 10^{16}$ cm^{-3}.

The effective carrier decay lifetime is also significantly determined by the bulk recombination. The latter is mostly changed by material fabrication technology and its resistivity. The decay transients measured in different materials are illustrated in Fig. 7.14. The longest decays were obtained in FZ high resistivity cleaved sample (in the range of 2 ms). Also long asymptotic lifetime was measured for optical- grade Ge, as in the latter material clear two-componential decay is observed. The latter component is governed by trapping, and trap filling manifestation is therefore observed. Effective lifetime in pure

Cz Ge decreases from several hundreds of μs to several nanoseconds when resistivity decrease from 35 to 0.01 Ω cm. Due to surface recombination influence, values of bulk lifetime is estimated to be $\tau_b \geq$ 500 μs in FZ ~40 Ωcm p-Ge, $\tau_b \geq$ 260 μs in Cz pure (~20-30 Ωcm) n- and p-Ge material, while it is found to be $\tau_b \sim$ 30 ns in 0.01 Ωcm resistivity p-Ge material.

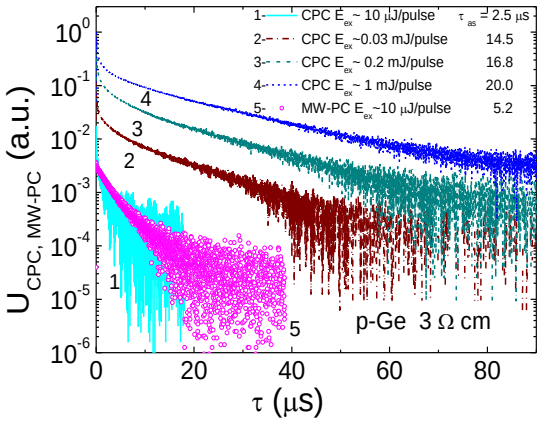

Fig. 7.13. Variation of photo-response transients with excitation energy of 1064 nm laser light measured by CPC and MW-PC techniques in Cz p-Ge of 3 Ωcm resistivity.

Recombination lifetime values determined in different resistivity Ge samples are generalized and plotted in Fig. 7.15 together with data from references [96, 97]. Lines in Fig. 7.15 represent the recombination lifetime variation, simulated using S-R-H model, with doping and trap activation parameters specific for our samples and in the range close to those published in [98]. Dopants concentration was evaluated from Irvin's curves [67, 99] where Ge resistivity is related with doping density. Values of recombination lifetime were measured at the lowest possible excitation densities to better fulfil the S-H-R model requirements. Measurements were also performed under bias illumination for low conductivity material to exclude trapping effects. Inevitably, excitation density was properly increased for the heavily doped materials to keep the same injection level. In the most conductive materials, excess carrier concentrations (n_{ex}) were close to equilibrium value n_0 at room temperature.

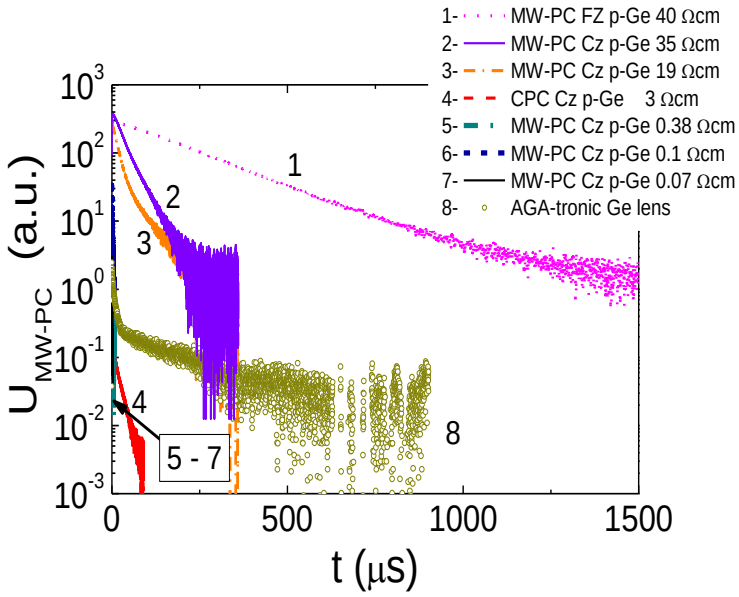

Fig. 7.14. MW-PC transients measured in Ge samples made of various technology and doping material.

The measured variation of τ_R as a function of dopants concentration n_{dop} agrees well that dependence $\tau_{S\text{-}R\text{-}H}$ - n_{dop} calculated using S-R-H approach and activation energy ascribed to deeper traps than those used in [98]. Experimental values of τ_R can be fitted by simulated $\tau_{S\text{-}R\text{-}H}$ ones up to doping values of $n_{dop} \sim 10^{16}$ cm^{-3}. An invariant concentration of the recombination centres can be assumed for doping concentrations below 10^{16} cm^{-3}. The observed further decrease of lifetime for $n_{dop} > 10^{16}$ cm^{-3} can be attributed to an increase of the recombination centres concentration, assumed to be proportional to the dopants density. In this case, the lifetime variation can be roughly approximated by $1/n_{dop}$ dependence and, in general, by the approximation:

$$\tau_R = \tau_{S\text{-}R\text{-}H} /(1 + n_{dop}/ n_{thr}) \ . \qquad (7.3)$$

Assuming a threshold doping density n_{thr} starting from which the generation of traps, related to the dopants introduction, becomes important. The lines (1,2) in Fig. 7.15 represent the low excitation level S–R–H

recombination lifetimes [59] as a function of dopant concentration calculated neglecting (1) and taking into account (2) the generalized approximation (7.3), respectively. Line 2 in Fig. 7.15, simulated with $n_{thr} = 4\times10^{16}$ cm^{-3} and keeping the same, as used for curve 1, other parameters is obtained being in agreement with experimental results. This is also in agreement with value of $n_{ex} \sim 10^{16}$ cm^{-3} estimated for 3 Ωcm Ge sample, evaluated from the trap filling effect dependent on excitation level. Curves (3–8) illustrate the simulated lifetime dependencies on excitation level and on doping, when assuming of a linear increase of excess carrier density with doping ($n_{ex} = k \cdot n_{dop}$), i.e. keeping the invariant excitation level k along simulation of a single curve, when n_{dop} changes. The excitation density is varied in the experiments by changing of IR light energy per pulse. Curves (3–8) are simulated using expression (7.3) at the same threshold doping density of $n_{thr} = 4\times10^{16}$ cm^{-3}, as in simulations of curve 2, but varying k from 0.01 to 100. Curves (3–8) were simulated using a less trap concentration value of 1.25×10^{12} cm^{-3}, relatively to that of 5×10^{13} cm^{-3} exploited in simulations of curves (1, 2), to approximately fit our experimental data at low excitation level (curve 3).

The lifetime values, simulated including n_{ex} variations, increase with excitation level (fixed by k), and the simulated curve (6) at $k = 1$ seems to be in reasonable agreement with the experimental data of Refs. [96, 97], when variations of excitation level are taken into account. Moreover, curves (5–8), simulated for k in the range of 0.5–100 of high excitation level, cover most of the experimental values published in [96, 97]. This implies that data in [96, 97] were obtained at elevated excess carrier densities to induce an observable photoconductivity signal. An increase of the lifetime values with excitation was also observed in our experiments as the trap filling effect which can only be revealed using short excitation pulses, but which cannot be observed in experiments with long excitation pulses, applied in [96, 100]. Thus, reliability of the estimated trap parameters (e.g. elevated recombination centres density values at low excitation level (curve 2 relatively to 3–8 ones in Fig. 7.15) or

decreased ones at high excitation if n_{ex} is neglected) depends on the adequacy of the model to the appropriately controlled experimental conditions and correlation of the results among different experiments.

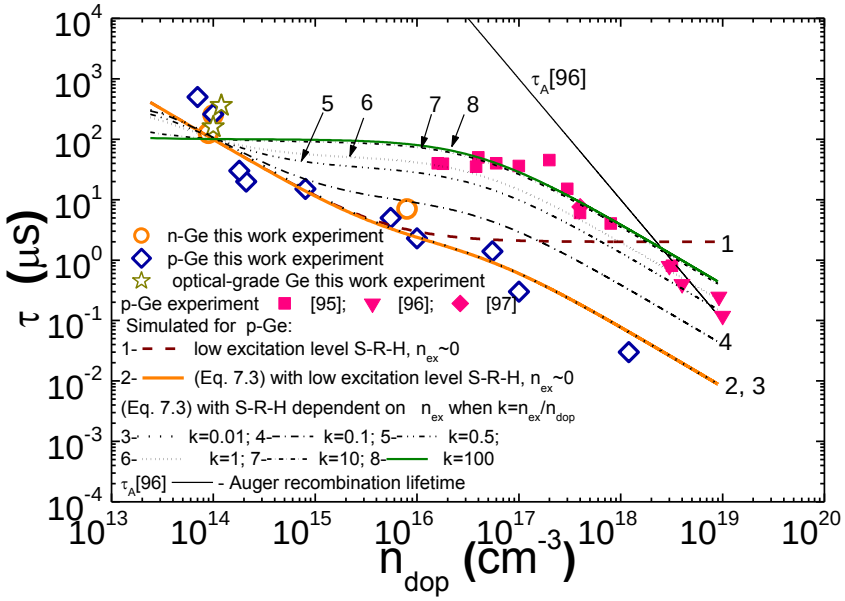

Fig. 7.15. Variation of recombination lifetime as a function of dopant concentration estimated from the material resistivity. Symbols and attribution of curves is denoted in the legend.

Correlation obtained for p-Ge over the wide range of n_{dop} is rather reasonable, taking into account errors of the n_{ex}/n_{dop} estimation. However, deviations of the experimental values for n-Ge, for optical-grade Ge and high purity FZ p-Ge from those simulated for p-Ge ones are noticeable. This implies specific defects inherent for different materials. This is also corroborated by a different character of the carrier decays obtained for optical-grade Ge material in our experiments. For doping densities above n_{thr}, the simple S–R–H model is insufficient, and this is taken into account by the term $(1+n_{dop}/n_{thr})^{-1}$ in expression (7.1). The nonlinear Auger recombination, shown schematically by the τ_A [100] line in Fig. 7.15, seems to be negligible in the investigated n_{dop} range, while the Auger coefficient is smaller than 10^{-30} cm^6/s. Moreover, a role of excess carriers should also be included at increased n_{ex} when estimating of the Auger coefficient values. In the case of a sharp excitation profile, surface

defects can also be the reason for the variation of the absolute τ values and the deviation from the expected bulk lifetime dependence on doping.

Thereby, the proposed approximation of the carrier recombination lifetime changes in Ge dependent on doping density and on excitation level describes well the experimental results in wide range of doping densities. The estimated value of the Auger recombination coefficient for the impact ionization processes involving equilibrium and excess carriers is in good agreement with that evaluated for the Auger process governed by the excess carrier interactions.

7.6. Metal implants caused variations of Ge recombination characteristics

Introduction of metal impurities by implantation leads to a decrease of carrier lifetime values compared to those in the as-grown material, as shown in Fig. 7.16. Here, measurements of carrier lifetime values were performed by MW-PC technique using VUTEG-4 instrument and keeping the same regime. This 7.16 figure also shows that the values of carrier lifetime in the as-implanted samples significantly depend on the implanted metal element. This dependence measured for the same excitation density roughly indicates the efficiency of the metal induced traps in changing the minority carrier lifetime. Clear decrease of lifetime values is qualitatively observed going from Ni through Cr, Ti and Fe, respectively, to Co. The largest lifetime values, obtained in Cr and Ni implanted *n*-Ge, are less than those measured in the initial material.

Notably, the recombination lifetime increases with implantation dose (Fig. 7.16). This enhancement can be explained by a metal implantation induced change in conductivity type within the near surface layer. Thus the formed junction passivates the surface recombination component and, therefore, the depth integrated recombination lifetime increases.

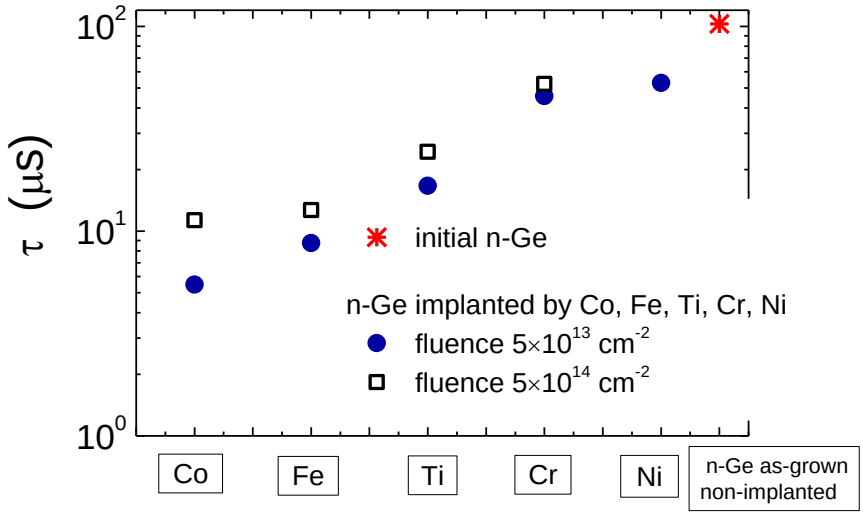

Fig. 7.16. Variation of carrier lifetime in *n*-Ge with implantation of different metals.

Examination of the lifetime dependences on injection level can be useful for estimation of the character of traps and evaluation of the ratio of the capture cross-sections for minority and majority carriers. The simplified idea is based on determination of high level lifetime τ_∞ , which is determined by the microscopic lifetimes τ_{n0} and τ_{p0} for electrons and holes, respectively, as $\tau_\infty = \tau_{n0} + \tau_{p0}$. The low level lifetime τ_0 is estimated from the lifetime value when approaching to zero injection. The latter τ_0 is approximately equal to $\tau_{0,\,minority}$ for deep levels and for moderate doping $<10^{16}$ cm^{-3}. Then, in *n*-type material $\tau_{0,minority} = \tau_{p0}$ [21]. From the ratio of the lifetimes $\tau_\infty/\tau_0 = (1 + \tau_{n0}/\tau_{p0})$ the ratio of the capture cross-sections $\tau_\infty/\tau_0 \approx \sigma_p/\sigma_n$ is evaluated. The acceptor-like character is established for the most of implanted metals (Fe, Co, Ni) in Ge. The acceptor-like trap in the upper band-gap side is known as the second-type recombination centre, using terms assumed in [59, 100]. From the $\tau_\infty/\tau_0 \approx \sigma_p/\sigma_n$ ratio a character (increase or decrease) of lifetime dependence on injection level can be foreseen for acceptors (increase) and donors (decrease), respectively.

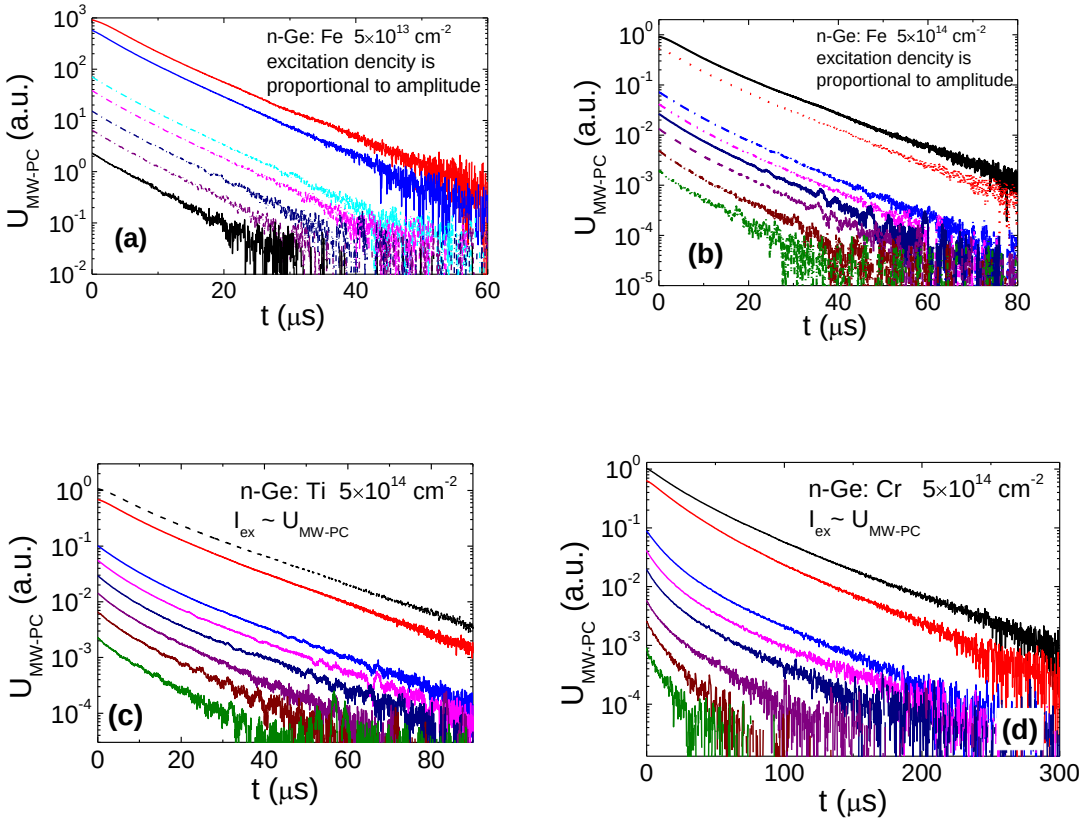

Fig. 7.17. MW-PC transients measured in *n*-Ge, implanted by Fe ions, at low (a) and high implantation fluence (b), respectively, as well as for Ti (c) and Cr (d) implanted *n*-Ge samples with fluence 5×10^{14} cm^{-2}. Excitation density in these plots is proportional to the MW-PC amplitude $U_{MW\text{-}PC}$.

The experimental MW-PC transients, measured in Fe, Co, Ti and Cr implanted *n*-Ge varying excitation density, are illustrated in Fig. 7.17.

Table 7.4. Ratio of the cross-sections of minority and majority carriers estimated for different implants and fluences.

σ_p/σ_n for different implants //implantation fluence	Co	Fe	Ti	Cr
5×10^{13} cm^{-2}	<1	~1	>1	>1
5×10^{14} cm^{-2}	~1	>1	>2	>4

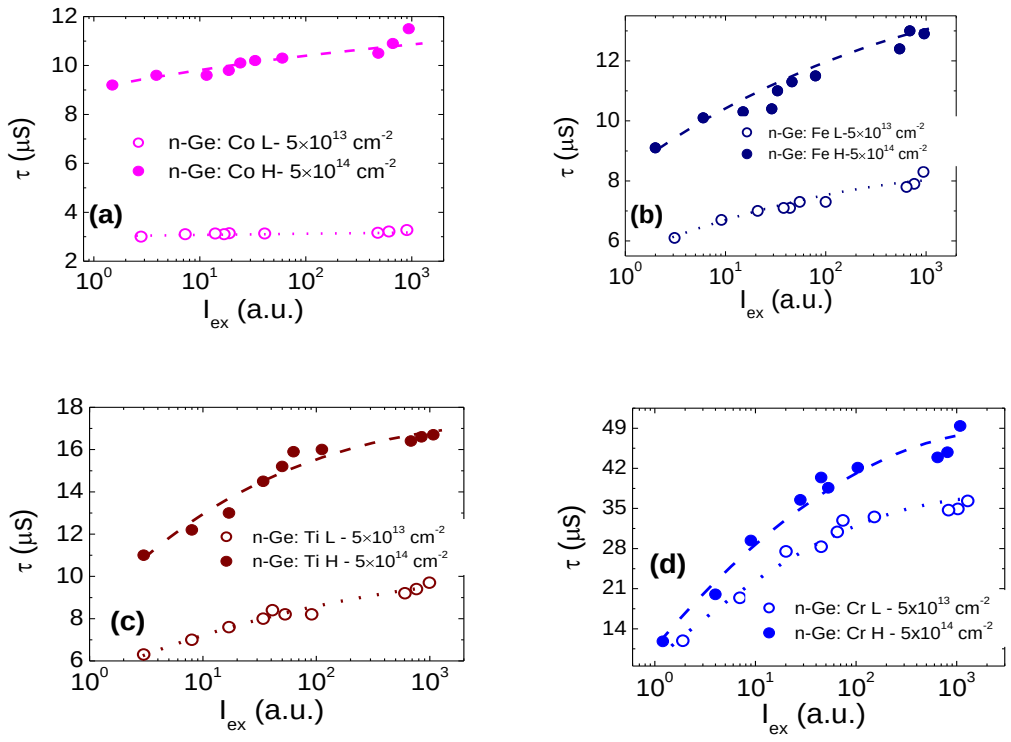

Fig. 7.18. Variation of carrier lifetime with excitation density in n-Ge implanted by Co (a), Fe (b), Ti (c) and Cr (d), respectively, with doses of 5×10^{13} and 5×10^{14}cm^{-2}.

Variations of the lifetime values with excitation density are presented using the semi-log scale in Fig. 7.18. The increase of lifetime with excitation density dominates in these dependences. Such lifetime increase with injection level is more pronounced for the samples with larger doses implantation of metals. Also, these lifetime variations are more pronounced for Fe and Cr implants. Such lifetime variation with excitation density corroborates an assumption that these implants in the Ge matrix are acceptors. Estimation the ratio of capture cross-sections for minority and majority carriers (σ_p/σ_n) was determined from recombination lifetime measured at low and high excitation condition (τ_∞/τ_0). These dependencies imply that σ_p/σ_n >1, which is an indication of acceptor-like behaviour of the traps induced by implanted metals. Existence of the acceptor–like traps is also supported by the σ_p/σ_n ratio behaviour as a function of metal implantation fluence. The estimates σ_p/σ_n values are also listed in Table 7.4. The clearest lifetime changes as a function of excitation had been

obtained in the Fe, Ti and Cr implanted samples as can be seen in Fig. 7.18. Implants of Fe and Co are the most effective minority carrier lifetime killers in n-Ge while Cr has the least influence.

7.7. Radiation defects in Si doped with Ge induced by 2 MeV electrons

Defect engineering by specific doping and irradiation technologies is one of the possibilities to improve and modify specific parameters of semiconductors devices [101, 102]. It is known that Ge doping of Si during the Czochralski (Cz) growth process has a beneficial effect on reduction of dislocation nucleation and being an isovalent impurity it does not introduce electrically active deep centres [103, 104]. Therefore, it is a promising dopant for the expedient manipulation both of the internal gettering capacity and of the intrinsic point defect incorporation during crystal growth. Radiation hardness of the n-type Cz grown Si diodes is discussed in this paragraph by analyzing Si samples doped with Ge of 10^{19} cm^{-3} (GCz) and of 10^{20} cm^{-3} (GGCz) in comparison with those undoped (Cz).

The carrier recombination lifetime considerably decreases with increasing 2 MeV electron irradiation fluence due to the increased density of deep centres, as can be directly observed from MW-PC transients (Fig. 7.19a) when analyzing the increase of carrier decay rate. The values of recombination lifetime, measured directly by MW-PC tehnique correlate well with those calculated from the space charge generation time measured by the I-V technique, as shown in Fig. 7.19b. Correlation between the directly measured recombination lifetime and that estimated from the generation lifetime, using simple S-R-H model, implies that the same type of radiation induced deep centres dominates, those act as the carrier capture and generation traps, in the irradiated material. Then, radiation induced defects prevail over thermal donors in redistribution of carrier flows. Therefore, generation lifetimes (shown in Fig. 7.19b) are very similar as well as their dependence on irradiation fluence for both Cz and GCz materials.

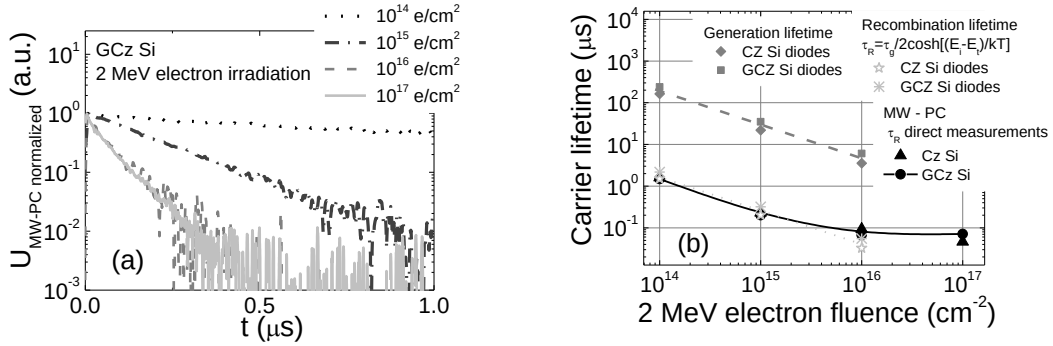

Fig. 7.19. a- Variation of MW-PC transients in GCz Si dependent on 2 MeV electron irradiation fluence. b- Carrier generation and recombination lifetimes as a function of electrons irradiation fluence evaluated by I-V and MW-PC techniques.

Radiation induced deep traps have been identified by using the capacitance deep level transient spectroscopy, i.e. C-DLTS. Typical DLTS spectra obtained on Si diodes with and without Ge doping after 2 MeV electron irradiation with a 10^{15} cm^{-2} electron fluence, are illustrated in Fig. 7.20.

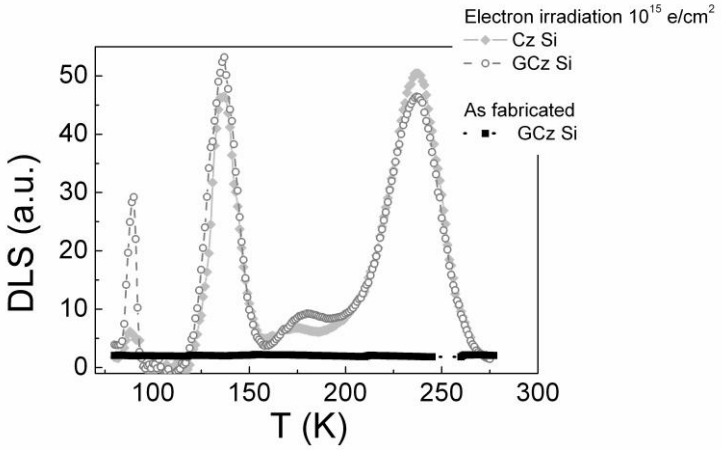

Fig. 7.20. DLTS spectra obtained on CZ and GCz Si diodes irradiated with 10^{15} cm^{-2} 2 MeV electrons.

Four peaks related to the radiation induced defects, which act as majority carrier trap centres, have been observed in both samples in the temperature range of 80 to 280 K. The peak at 85 K is attributed to the V-O centre, $V_2^{2-/-}$ is situated at 137 K, the peak at 175 K is associated with multivacancy complexes

while the divacancy ($V_2^{-/0}$) in its single charged state is observed at 240 K. Fig. 7.20 shows that the densities of the deep centres are close for both Cz and GCz materials, excepted for the V-O centre, which is the most sensitive to Ge doping. As Ge suppresses formation of thermal donors, the density of V-O centres in the irradiated GCz material is larger than that in the Cz material, due to the larger concentration of oxygen in the GCz material.

Thus, measurements of carrier lifetime by the MW-PC contactless technique allows rapid revealing of an impact of radiation defects. The obtained carrier lifetime changes reproduce well those extracted from I-V characteristics, which can be controlled only on proper electrodes containing samples.

Summary of the main results described in the chapter

[A2-A4, A7, A10-A13, A18- A20]

Contactless MW-PC and DRG techniques have been combined and approved for direct measurements of the carrier recombination and transport characteristics in ultra-thin layered structures. Recombination lifetimes from tens to hundreds of nanoseconds were determined in the SRB layers containing different density of dislocations. A hyperbolic-like excess carrier relaxation within asymptotic carrier decay part has been unveiled in the SRB layers, and this carrier density relaxation behaviour is ascribed to multi-trapping processes characterized by trapping coefficient K_{tr}>10, which is attributed to disorder caused by dislocation network. Stochastic carrier transport play important role for carrier diffusion and the value of the lateral carrier diffusion coefficient $D_a \leq 0.13$ cm^2/s is inherent for dislocated structures.

The value of surface recombination velocity increases with worsening a quality of surface passivation on Ge samples when comparing of grinded, freshly cleaved and polished surfaces of the same material. Carrier lifetime variations with doping in Ge had been determined at low and elevated excitation levels. It was inferred that this lifetime dependence on doping

density can be approximated by S–R–H model in low and moderately doped material, while lifetime decreases linearly with $1/n_{dop}$ for dopant concentrations above $n_{thr} = 4\times10^{16}$ cm^{-3}. This behaviour can be attributed to an increase of the doping technology introduced recombination centres, which density is proportional to the dopants concentration.

The native Ge defects act together with implantation induced impurities causing complicated recombination characteristics dependent on excitation and annealing conditions. Fe and Co are the most effective lifetime killers in Ge while Cr has the least influence.

Value of the Auger recombination coefficient $\gamma_{A,Ge}= (8\pm3)\times10^{-31}$ cm^6/s has been evaluated.

Small influence of Si doping with Ge in the range of $10^{19} – 10^{20}$ cm^{-3} has been observed for radiation defects formation.

VIII. Growth and irradiation dependent characteristics of GaN

8.1. Samples and structure investigated

A set of bare layers or junction structures made on either on ~2 or 12 μm thick semi-insulating GaN epi-layers has been investigated. Thin films of GaN were grown on a sapphire substrate by metal-organic chemical vapour deposition (MOCVD) employing trimethylgallium (TMG) as precursors. Quality of the films depend on the rate of TMG flow, therefore PL spectroscopy and photoconductivity transient techniques have been adopted to control defects manifestation. For comparison the free standing GaN as-grown samples of 500 μm thickness, fabricated by hydride vapour phase epitaxy (HVPE) have been also investigated. The top Schottky junction with guard rings has been deposited using Ti/Al metallization. The latter structures have been exploited as radiation and particle detectors. These structures were irradiated with penetrative hadrons – 23 GeV/c protons and neutrons at CERN and TRIGA reactor at Ljubljana, respectively. Variation of defects density and of recombination flows competition between radiation and grown-in defects were investigated after irradiation in the range of 10^{14} – 10^{16} cm^{-2} of neutrons or protons fluences.

8.2. Growth technology determined variations of decay lifetime

Photoluminescence (PL) spectra measured at the same excitation conditions consist of three bands (Fig. 8.1). These spectra have been analyzed by comparing spectrum structure obtained on MOCVD as-grown GaN layers of different thickness, by comparing the data recorded for samples fabricated varying growth regimes and technologies (TMG flow rate, MOCVD vs. HVPE). An ultraviolet (UV) band peaked at 3.42 eV is attributed to the band-to-band recombination. The latter two blue (B at 2.85eV) and yellow (Y at 2.18eV) bands probably represent deep centres related luminescence. The structure of the PL spectrum featuring a B band is inherent for GaN containing a high density of dislocations [104]. The Y band in PL spectra can be ascribed

to point defects, e.g. complexes of Ga vacancy [104-106]. Intensity of the latter Y- and B- bands depends on the flow rate of trimethylgallium (TMG) (curves 1 and 2, Fig. 8.1), when the density of the point defects increase with TMG flow rate. Contrary, in the thicker layer, concentration of these defects is diminished, when comparing the PL intensities for spectra 1 and 3 of Fig. 8.1. Synchronous enhancement of the intensity of UV band, with well expressed edge luminescence structure, is observed together with decrease of defect attributed PL bands (curves 1 to 3, Fig.8.1). It can be understood assuming that the larger excess carrier density annihilates via band-to-band recombination, when varying the TMG flow rate and layer thickness.

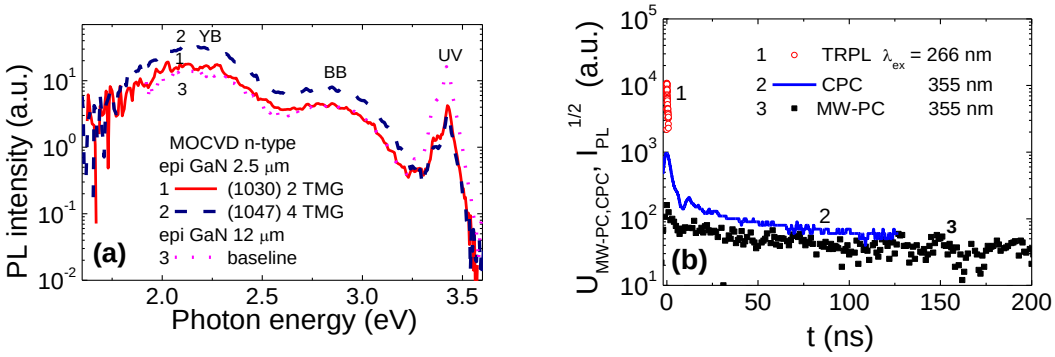

Fig. 8.1.(a) – PL spectra obtained on different thickness and on samples obtained by varying TMG flow of the MOCVD grown GaN epi-layers (b) – TRPL decay (1) collated with the initial stages of CPC (2) and MW-PC (3) transients in the as-grown GaN epi-layer of 2.5 μm thickness.

The contact photoconductivity (CPC) transients shown in Fig. 1b represent the variation of the free-carrier density with time due to fast carrier capture dominance within the initial decay stage followed by a long non-exponential asymptotic relaxation component. The ratio of the amplitude of the initial decay to that of the asymptotic one varies with defects density. The fast decay component is determined by the radiative recombination, as demonstrated by the short time-resolved PL transient (curve 1 Fig. 8.1b.). The excess-carrier decays, revealed in the MW-PC and CPC transients of the as-grown material (curves 2 and 3, Fig. 8.1b) contain also an initial stage with a fast component

of a few nanoseconds dependent on the excitation density. The initial instantaneous lifetimes of the MW-PC decays are close to that estimated from the time-resolved photoluminescence (TRPL) signal relaxation rate. The saturation effect of the asymptotic decay amplitude was found to be dependent on defect structure and concentration. The long tail component is ascribed to excess carrier trapping processes at dislocations, those comprise disordered network within epi-layer.

8.3. Simultaneously probed photoluminescence and photoconductivity

It has been revealed from combined CPC& MW-PC decays compared with TRPL transients (Ch.8.2), that the initial photoconductivity decay stage correlates well with radiative recombination kinetics. This result implies that micro-volumes of multi-crystalline GaN layer, for which fast photoconductivity and PL transients are inherent, coincide. Thus, it can be assumed that slow MW-PC component appears due to carriers brought to periphery of monocrystalline columns within GaN epi-layer. The dislocations are namely located within these periphery areas surrounding crystalline columns. Excess carriers, brought to the periphery areas with space charge regions within Cottrell spheres of dislocations, are separated by space charge field, and their recombination is only mediated by diffusion, caused by excess carrier density gradients. Thereby, different (fast and slow) carrier decay components should be ascribed to different micro-areas of epi-GaN material. It is really confirmed by PL microscopy, that PL signal contains a granular structure. Thus, the simultaneous control of photoconductivity (ascribed to integrated over excitation beam spot area) and photoluminescence (associated with micro-crystalline volumes) spectrum and time resolved signals can be a tool to resolve an impact of different layer micro-volumes to carrier decay.

A sketch of experimental arrangement, proposed in this work for simultaneous MW-PC and PL spectrum and time resolved measurements is shown in Fig. 8.2.

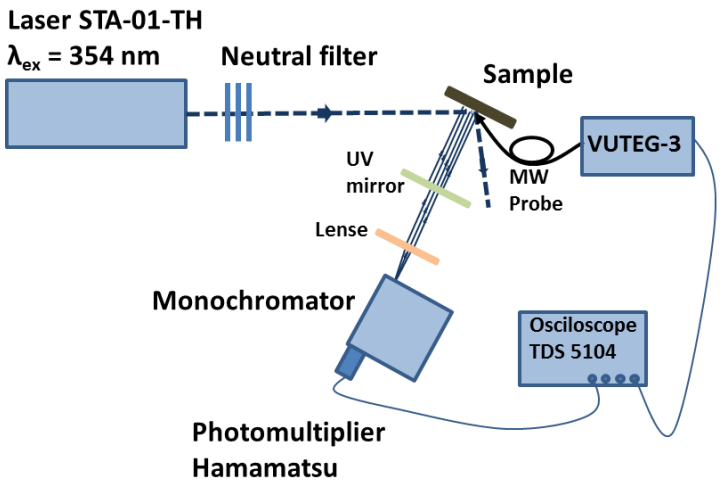

Fig. 8.2. Setup of instrumentation for the simultaneous measurements of the MW-PC and PL spectrum resolved transients.

Transient signals of the MW-PC and of PL have been synchronously measured from the same UV (354 nm) excitation beam spot, generated by a micro-chip laser STA-1-TH employed for pulsed (500 ps) excitation of the excess carriers. Intensity of excitation is varied by spectrally neutral optical filters. The MW-PC response has been detected by using coaxial needle-tip probe and instrument VUTEG-3. The registered signal is transferred from VUTEG-3 to a digital 1GHz oscilloscope TDS-5104, equipped with PC computer, where MW-PC transient is displayed and processed. The PL light is collected from the area with normal directed towards bisector between the incident and reflected UV light beams. The UV filtered PL beam is focused onto a slit of monochromator. The PL light is displayed using grating within monochromator and PL pulsed signal is detected by Hamamatsu H10721 photomultiplier. This PL signal is also transferred to another channel of the digital oscilloscope TDS-5104, where PL transient is displayed and processed together with MW-PC transient.

The registered PL amplitudes as a function of PL quantum energy $h\nu$ is plotted in Fig. 8.3. Several PL bands can be resolved within PL spectrum, namely, excitons ascribed UV-PL band edge for $h\nu$>3.2 eV, blue B-PL bands for 2.5<$h\nu$ <3.0 eV and yellow Y-PL with $h\nu$<2.4 eV. It can be deduced from

comparison of these spectra measured at different excitation densities, that intensity of UV- PL band increases with excitation density, while intensity of B-PL band is nearly invariant, but intensity of Y-PL increases with reduction of excitation density. This clearly indicates that Y-PL is sharpened with reduction of excess carrier density, and it can be associated with trapping centres.

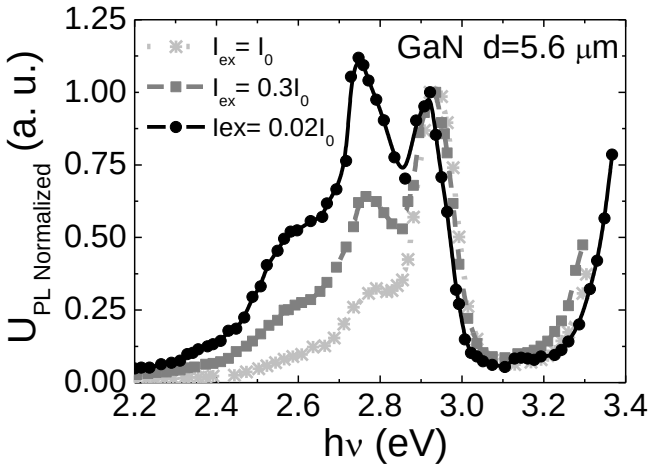

Fig. 8.3. Spectral variations of the amplitude of PL transients measured at different excitation densities.

In most of epi-GaN samples, the initial component of the MW-PC transients is of the same time scale as those of PL transients measured for different PL wavelengths, keeping the rather large excitation density, curves 1-4 in Fig. 8.4a. A reduction of UV excitation density leads to a decrease of amplitude of the asymptotic component within MW-PC transients, as illustrated in Fig. 8.4 b. This excitation reduction also determines shortening of the initial MW-PC decay component. While, a reduction of UV excitation density causes an increase of Y-PL asymptotic decay amplitude and of its duration, as can be inferred looking at curve 5 in Fig. 8.4a. These observations can be understood by prevailing of MW-PC & PL signals collected from the crystalline volumes of epi-layer, when responses are averaged over excitation spot. The UV- and B-PL exhibits these volumes where carrier decay happens

rapidly. This is confirmed by sharpening and shortening of the initial MW-PC component, with reduction of excitation density, Fig. 8.4b. It is explained by a reduced the whole excess carrier density and the diminished role of the inter-microcrystalline areas. While within rather short time domain, relatively to that for MW-PC in Fig. 8.4b, carrier density is sufficient to detect asymptotic decay within MW-PC and PL transients (Fig. 8.4a). There, an increase of the Y-PL amplitude and of its duration can be clarified in curve 5 in Fig. 8.4a. These observations imply again that Y-PL is associated with PL within inter-microcrystalline areas where trapping assisted diffusion of carriers leads to long-tail MW-PC transient. In several GaN epi-layers, these Y-PL amplitude and duration changes can be clearly observed, as in Fig. 8.5. There, amplitude of Y-PL increases with reduction of UV excitation density. In Fig 8.5, a small initial component within Y-PL transients can be noticed. This can be explained by a fast inflow of excess carriers from the microcrystalline volumes into inter-microcrystalline areas.

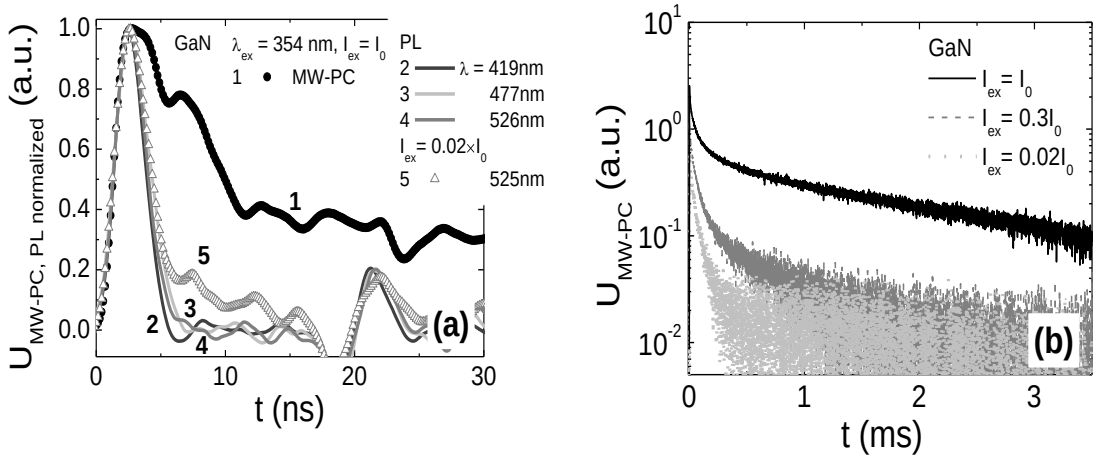

Fig. 8.4. a- The initial part of the MW-PC decay transient (1) compared with simultaneously registered PL transients (2-4) at different PL wavelengths when using the same UV excitation pulsed light intensity (1-4) and PL transient (5) measured at 525 nm wavelength with 50-times less UV excitation intensity. b- MW-PC decay transients measured varying UV excitation density.

The increase of microcrystalline volumes is probable with thickness of epi-GaN layers, due to coalescence of these microcrystalline volumes and consequent reduction of areas of dislocations-rich material.

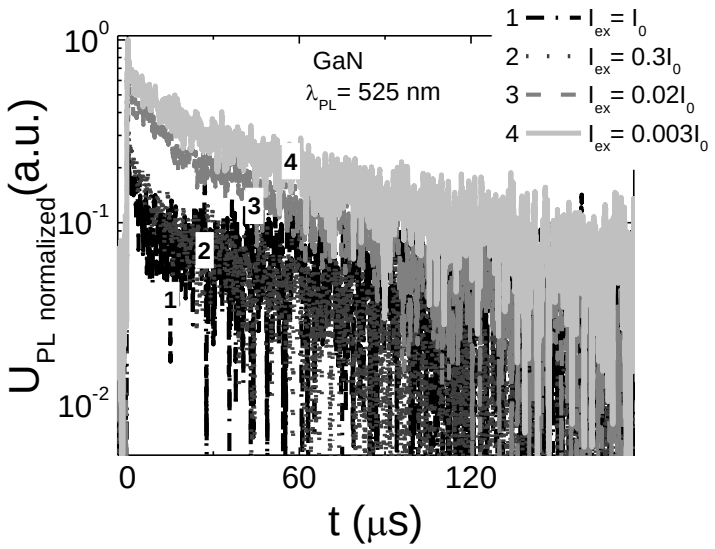

Fig. 8.5. The PL decay transients measured at 525 nm wavelength varying excitation densities.

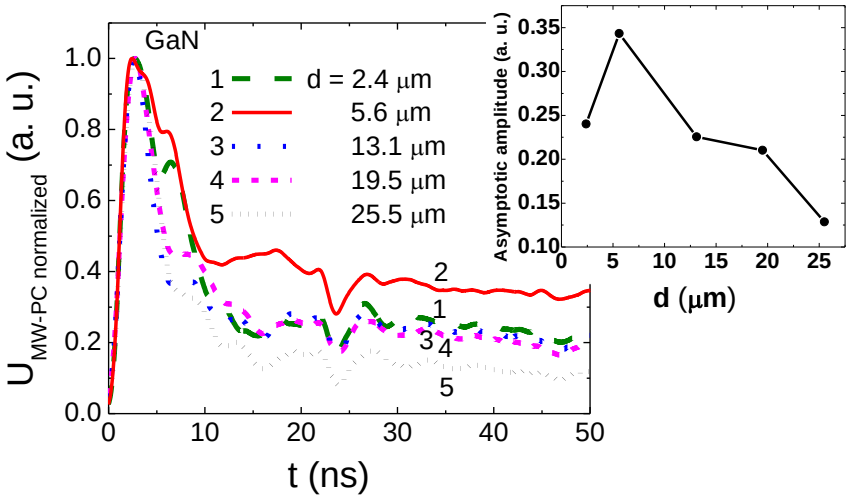

Fig. 8.6. The initial part of the MW-PC decay transients measured on samples of different thickness grown by the same MOCVD regime. In the inset, - the amplitude of the trapping component as a function of epi-GaN layer thickness.

These predictions have been confirmed by analyzing the amplitudes of the MW-PC asymptotic components as a function of epi-layer thickness, illustrated in Fig. 8.6b. The amplitude of the asymptotic component decreases with enhancement of layer thickness. Simultaneously, a reduction of duration of the MW-PC initial component is revealed. These observations can be simply considered as surface recombination on micro-crystalline volume boundaries.

Mathematical model of surface recombination in disordered material with imbedded micro-crystalline volumes of a cylinder shape can be solved in the cylindrical coordinates. The equation of carrier diffusion towards dislocation-rich regions within a crystalline cylinder of radius r_0 can be written as follows:

$$\frac{\partial n(r,t)}{\partial t} = D\left[\frac{\partial^2 n}{\partial r^2} + \frac{1}{r}\frac{\partial n}{\partial r}\right] = D\frac{1}{r}\frac{\partial}{\partial r}\left[r\frac{\partial n}{\partial r}\right],\ 0 \le r < r_0,\ 0 \le t < \infty, \tag{8.1}$$

Taking into account homogeneous excess carrier distribution just after excitation (t=0) as $n(r,0)=n_0$, $0 \le r < r_0$. Boundary condition describing carrier recombination at the cylinder boundary determined by surface recombination velocity s is presented as follows:

$$\left.\frac{\partial n}{\partial t}\right|_{r=r_0} = -\frac{s_{disl}}{D}n, \qquad \left.\frac{\partial n}{\partial t}\right|_{z=0,d} = -\frac{s_{0,d}}{D}n. \tag{8.2}$$

Solution of continuity equation (8.1) is expressed by infinite series as

$$n(r,t) = \sum_{j=1}^{\infty} A_j \exp\left(-\frac{\eta_j^2 D}{r_0^2}t\right) J_0\left(\frac{\eta_j r}{r_0}\right) \quad , \tag{8.3}$$

where J_0 is a Bessel function, η_j - space frequency and A_j denotes the amplitude of spatial modes, expressed as:

$$A_j = \frac{2\eta_j^2}{r_0^2\left[\eta_j^2 + \left(\frac{s}{D}\right)^2 r_0^2\right] J_0^2(\eta_j)} \int_0^{r_0} r J_0\left(\frac{\eta_j r}{r_0}\right) dr \tag{8.4}$$

For the three-dimensional carrier diffusion, including that along the cylinder height (z coordinate), carrier distribution is expressed by a product $n(z,r,t) = n(z,t) \times n(r,t)$ with

$$n(z,t) = \sum_{m=1}^{\infty} C_m e^{-\nu_m^2 Dt} \sin\left(\nu_m^2 z\right) \tag{8.5}$$

containing an additional space frequency v_m. Coefficients C_m are defined like in solution for the one-dimensional diffusion (3.18).

The experimentally measured MW-PC signal is an average integrated over the excitation beam spot of radius R_0. Thus, this solution acquires a more complicated expression:

$$\left\langle n(r,z,t)\right\rangle_{R_0,d} = \frac{1}{d}\frac{1}{\pi R_0^2}\int_0^d \int_0^{R_0} \sum_{m,j=1}^{\infty} A_j C_m \exp\left[-\left(\nu_m^2 + \frac{\eta_j^2}{r_0^2}\right)Dt\right]\sin(\nu_m z)\int_0^{r_0} rJ_0\left(\frac{\eta_j r}{r_0}\right)drRdRdz\,, \quad (8.6a)$$

with spatial frequencies defined from the transcendental equations as

$$\eta J_0^{'}(\eta) + \frac{s_{disl}}{D} r_0 J_0(\eta) = 0\,,$$

(8.6b)

$$ctg\,\nu d = \frac{s_0}{s_0 + s_d}\left(\frac{D\nu}{s_0} - \frac{s_d}{D\nu}\right).$$

Nevertheless, this analytical solution is sufficient to notice the main features of decays. It can be inferred that the non-exponential decay should be observed when surface recombination is prevailing. Such features can be deduced from Figs. 8.5 and 8.6. For the depth-inhomogenous excitation, only the asymptotic decay component of surface recombination determined transient holds a single-exponential shape. For a narrow dynamic diapason of excess carrier density relaxation, only the initial decay component often shows a detectable signal. But this signal is inappropriate for extraction of the parameters of surface and bulk recombination, as it represents appearance of the highest decay modes, those are nearly impossible to separate. Then, only decays containing a clear two-exponential behaviour are acceptable for evaluation of surface recombination on micro-crystalline boundaries. The situation appears to be even more complicated when disorder features of dislocations network become important.

8.4. Irradiations determined changes of recombination characteristics

Photoluminescence spectra obtained at room temperature for as-grown and the irradiated samples, both with protons and neutrons, exhibit again three bands (Fig. 8.7a), while the amplitude of the spectral peaks depends on the fluence of irradiation. The most significant decrease of PL intensity with irradiation fluence is observed for YB luminescence, and this band disappears in the samples irradiated with the highest fluences.

The CPC transients exhibit a hyperbolic-like shape for the initial material and irradiated with the lowest fluences. An initial fast decay component and its partial amplitude increases with irradiation fluence. Meanwhile trapping caused long tail component is shortened most significantly with irradiation fluence, as illustrated in Fig. 8.7b, and for large fluence of hadrons irradiation in the range of 10^{16} cm^{-2} the asymptotic decay component is non-resolvable. This can be explained by the enhancement of the recombination rate within crystallites material with increase of the radiation defects density. The activation energy of about 0.3 eV [107] was deduced from the temperature dependences of the initial as well as of asymptotic decay lifetimes measured by MW-PC in the as-grown material.

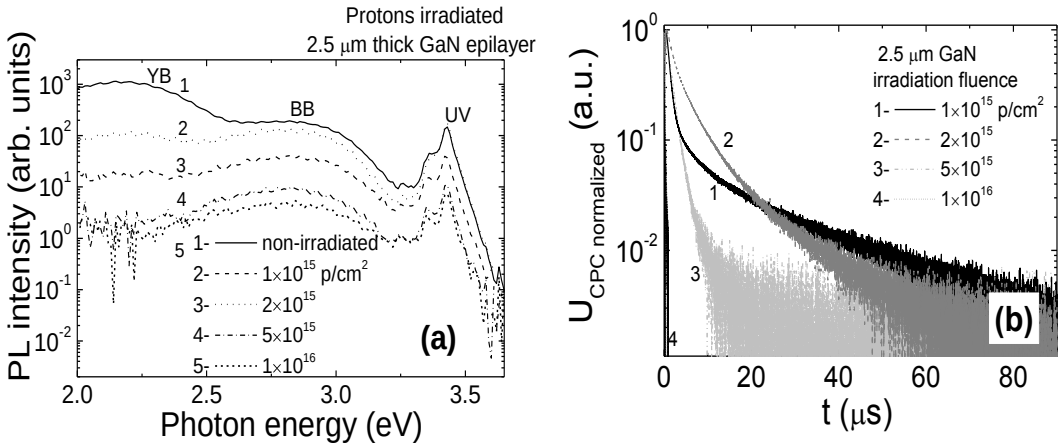

Fig. 8.7. Evolution of the PL spectra (a) and of CPC transients (b) in the 2.5 μm thick GaN epi-layers as function of proton irradiation fluence.

The inverse lifetime and the inverse intensity of the PL bands are proportional to the variations of the concentration of radiation induced traps. The inverse recombination lifetime (Fig. 8.8a) shows nearly linear increase with protons and neutrons irradiation fluence. However, the larger lifetime decrease has been obtained for the thinner layers. Variation of the inverse intensity of the YB-PL, which is ascribed to point defects [104, 108], can be linearized only for the range of fluences below 2×10^{15} cm^{-2}, and above which the saturation of this dependence appears. These variations of CPC and PL characteristics can be explained either by a heal of YB-PL centres due to formation of complexes of the native and radiation induced defects or by redistribution of carrier capture flows between YB-PL levels and radiation induced non-radiative centres, as density of those increases nearly linearly, as deduced from CPC measurements.

The increase of the asymptotic carrier decay rate (τ_{as}^{-1}) is nearly the same in protons as neutrons irradiated samples (Fig. 8.8b). However, it increases with fluence significantly faster than the PL intensity decreases for all the observed PL bands. Really, the asymptotic decay is non-exponential due to dislocation networks attributed trapping (Fig. 8.7), and instantaneous lifetime τ_{as} is only an indication of the redistribution between recombination and trapping flows. The initial trapping processes revealed in the MW-PC and CPC transients of the moderately irradiated and as-grown material can be explained by the rapid hole capture into dislocation-attributed defects, since in the n-type material no potential barrier for holes exists [88]. The capture rate is determined by the lateral diffusion towards dislocations [88] within asymptotic, trapping dominant, decay part. Therefore, duration of this trapping/ asymptotic decay process is decreased with density of radiation defects induced by hadrons relatively to that in the as-grown material. Since the capture cross-section of non-radiative traps depends on their occupation and varies during relaxation of the excess carriers, the distribution of the trap depth within a cluster of dislocations is random. This causes a wide spectrum of traps [109]. The

asymptotic non-exponential decay component (which can be linearized in a logarithmic scale of the representation of carrier density vs t^{α} dependence [105–107]) is also sensitive to defect density. This cluster determines the multi-trapping processes which decreases the rate of a direct carrier recombination process. The multi-trapping inherent behaviour of decay rate changes tends to the stretched-exponent decay, when $I_{CPC\&MW\text{-}PC}\ (t)$ fits [105, 106] a stretched exponent $exp[(-t/t)^{\alpha}]$ function [81].

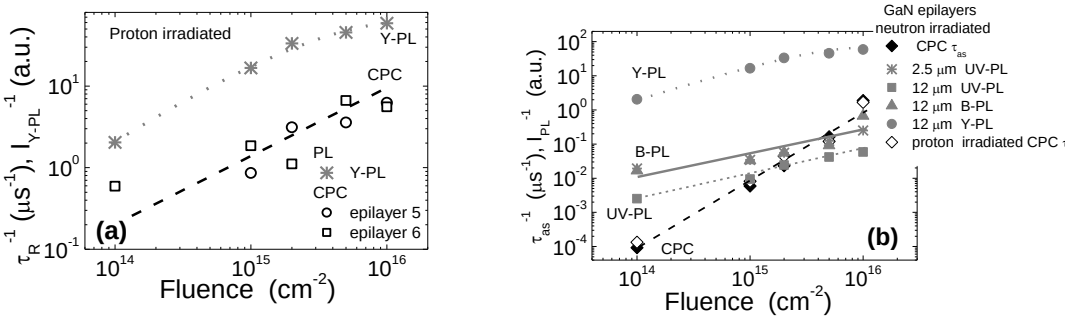

Fig. 8.8. Inverse recombination (a) and asymptotic decay (b) lifetimes as a function of irradiation fluence. Fluence dependent variations of the inverse intensity of Y-PL band under protons irradiation (a), as well as variations of the inverse intensities of Y-PL, B-PL and UV-PL bands in neutrons (solid symbols) and protons (open symbols) irradiated GaN epilayers of different thickness.

For the *i*-th single-step carrier one-direction shift X_i within its random-walk, a function of probability density for this shift can be defined using Dirac's delta functions $\delta(x)$ as

$$P_{X_i} = \frac{1}{3}\left(\delta(x+\Delta) + \delta(x) + \delta(x-\Delta)\right), \tag{8.7}$$

which leads to a characteristic function of probability density which is expressed as

$$f_{X_i} = \int_{-\infty}^{\infty} dx\, e^{ikx} P_{X_i} = \frac{1}{3}\left(e^{ik\Delta} + 1 + e^{-ik\Delta}\right) = \frac{1}{3}\left(1 + 2\cos(k\Delta)\right). \tag{8.8a}$$

The latter function of N steps is transformed as follows:

$$f_X = \frac{1}{3^N}\left(1 + 2\cos(k\Delta)\right)^N. \tag{8.8b}$$

Assuming approach to a quasi-continuous process limit $\Delta \to 0$, $\tau \to 0$ and $t = N\tau$, it can be obtained

$$f_X\left(k,(N+1)\tau\right) - f_X\left(k,N\tau\right) = \left(-\frac{k^2\Delta^2}{3} + \ldots\right) f_X\left(k,N\tau\right) = -Dk^2 f_X\left(k,t\right), \quad (8.9)$$

with $D = \Delta^2/3\tau$. Then, the rate equations for Fourier image (f_X) and for a function of probability density (P_X), respectively, can be written as follows:

$$\begin{aligned} \frac{\partial f_X\left(k,t\right)}{\partial t} &= -Dk^2 f_X\left(k,t\right) \\ \frac{\partial P_X\left(x,t\right)}{\partial t} &= D\frac{\partial^2 P_X\left(x,t\right)}{\partial^2 x} \end{aligned}, \quad (8.10)$$

with boundary conditions

$$P_X\left(x,0\right) = \delta\left(x\right) \to, f_X\left(k,0\right) = 1. \quad (8.11)$$

Then, relating a mean-square shift in four dimensional time-space as

$$\left\langle x^2(t)\right\rangle = Dt \quad , \quad (8.12)$$

and for a mean–square shift for random-walk [110] as

$$\left\langle x^2(t)\right\rangle \sim t^{\frac{2}{d_w}}, \quad (8.13)$$

value for a coefficient of carrier diffusion, limited by trapping, is expressed as

$$D = C_D t^{\frac{2}{d_w}-1}. \quad (8.14)$$

Thereby solutions of the rate equations (8.10) with boundary condition (8.11) are obtained as

$$f_X\left(k,t\right) = \exp\left(-\frac{1}{2} d_w C_D t^{\frac{2}{d_w}} k^2\right) \quad , \quad (8.15)$$

and

$$P_X\left(x,t\right) = \sqrt{\frac{1}{4\pi C_D t^{2/d_w}}} \exp\left(-\frac{x^2}{4C_D t^{2/d_w}}\right).$$

The latter solution is obtained in the form of stretched-exponent, and it is related to a Hausdorff and fractal dimension d_w [110] for the random-walk within a disordered structure.

The as-grown material and the irradiated samples exhibited different values of time-stretching factor equal to 0.7 and 0.3, respectively. Change of values of the fracton dimension from 4.7 to 0.86 for as-grown and irradiated material, respectively, indicates that such a cluster of dislocation net is fragmented into finite fractons [110]. Disorder facilitates capture of carriers into relatively shallow levels, thus reducing the occupation of the recombination-active centres and affecting the efficiency of radiative recombination when trapping processes prevail in the as-grown and moderately irradiated material. While, in the samples heavily irradiated by neutrons and protons of fluence 10^{16} cm^{-2}, the radiation induced recombination and scattering centres within crystallites reduce the carrier lifetime and trapping limited diffusion of carriers.

The MW-PC measurements are performed at low excitation levels, thus material properties close to equilibrium are observed. At high excitation densities, the trapping limited processes might be excluded if excess carrier densities considerably exceed the density of traps, when clusters surrounding fields are screened.

Summary of the main results described in the chapter

[A1, A2, A6, P2, P3]

The excess-carrier decays, revealed in the MW-PC transients of the as-grown material contain also an initial stage with a fast component of a few nanoseconds dependent on the excitation density. The initial instantaneous lifetimes of the MW-PC decays are close to that estimated from the time-resolved photoluminescence signal relaxation rate. The saturation effect of the asymptotic decay amplitude was found to be dependent on defect structure and concentration. The long tail component is ascribed to excess carrier trapping processes at dislocations, those comprise disordered network within epi-layer.

The experimental arrangement has been proposed and approved in this work for simultaneous MW-PC and PL spectrum and time resolved measurements.

The increase of microcrystalline volumes is probable with thickness of epi-GaN layers, due to coalescence of these microcrystalline volumes and consequent reduction of areas of dislocations-rich material. The amplitude of the asymptotic component decreases with enhancement of GaN layer thickness. Simultaneously, a reduction of duration of the MW-PC initial component is revealed. These observations can be simply considered as surface recombination on micro-crystalline volume boundaries. A mathematical model of surface recombination in disordered material with imbedded micro-crystalline volumes has been proposed.

Trapping caused long tail component in GaN layers is shortened most significantly with hadrons irradiation fluence, and for large fluence of hadrons irradiation in the range of 10^{16} cm^{-2} the asymptotic decay component is non-resolvable. This has been explained by the enhancement of the recombination rate within crystalline material with increase of the radiation defects density.

The MOCVD as-grown GaN material and the irradiated samples exhibited different values of time-stretching factor equal to 0.7 and 0.3, respectively. Change of values of the fracton dimension indicates that such a cluster of dislocation net is fragmented into finite fractons.

Summary of the main dissertation results and conclusions

1. The models appropriate for extraction of carrier recombination parameters by contactless measurements of carrier decay transients using effects of the microwave and infrared absorption by free carriers have been accommodated to validate the combined measurement techniques in wide dynamic range (from 10^{11} to 10^{19} cm^{-3}) of excess carrier densities. It has been proposed and approved the methodology for extraction of bulk and surface recombination parameters, for separation of the impact of carrier recombination and trapping effects, for carrier lifetime profiling within its lateral and depth variations. The combined measurement regimes have been approved. The portable instruments VUTEG-3 and VUTEG-4, based on the designed measurement regimes, have been manufactured, calibrated and employed in multi-functional applications for monitoring of technological and radiation defects.
2. The techniques of time resolved spectroscopy of deep levels, based on photo-ionization and photoconductivity quenching effects, have been proposed and approved for characterization of deep levels in Si and Ge structures. Several deep levels ascribed to radiation defects in Si have been identified by using time resolved photo-ionization spectroscopy. Photo-activation energy values of these defects are close to those identified by other spectral techniques such as DLTS.
3. Combined analysis of the photo-ionization and photoconductivity quenching (PCQ) spectral characteristics allows separating of carrier capture flow redistribution in the intricate systems of interacting centres. Coexistence of slow and fast recombination centres, which interplay leads to appearance of the PCQ effect. The acceptor-like behaviour has been ascribed to slow centres while donor-type defects should be attributed to fast ones.
4. The linear bulk recombination lifetime decrease with enhancement of hadrons irradiation fluence has been revealed. This lifetime characteristic

shows the same absolute values of carrier lifetime ascribed to definite irradiation fluence values, irrespective to material growth technology and structure, nearly the same for wafer samples and particle detectors.

5. Depth profiling of the carrier lifetime distribution enabled to infer that penetrative hadrons induce homogeneous distribution of radiation defects within Si samples of thickness ≤ 300 μm. It has been demonstrated that lateral and depth-dependent carrier lifetime profiling reproduce rather well the proton beam spot contour and stopping range of the implanted protons, respectively.
6. The temperature and anneal dependent variations of trapping lifetime enable one to reveal fluence governed formation of cluster defects. The clusters related recombination and trapping centres cause complicated changes of the recombination-trapping characteristics which are explained by variation of distance between clusters, dependent on irradiation fluence.
7. A comprehensive instrument based on MW probed photoconductivity transients control has been designed, fabricated and approved for the remote and *in-situ* monitoring of defects evolution during irradiation by protons. This instrument has been installed within accelerator facilities at proton accelerators of Helsinki University and of the Centre of Physical and Technology Sciences in Vilnius.
8. The different rates of the production of the dominant recombination centres have been clarified during penetrative protons irradiation. The defect production rate has been found to be dependent on irradiation temperature and on the pre-irradiation conditions of Si material. The models of cluster formation impact on the carrier lifetime reduction rate during irradiation and of surface recombination on cluster boundary have been proposed. These models have been employed to prove the prevailing of the radiation induced cluster defects, acting as the dominant carrier recombination centres, while cluster surrounding space charge sphere determines carrier

trapping effects. The activation energy of carrier trapping centres has been extracted by using temperature scans of the asymptotic decay lifetimes.

9. The fluence-dependent $\tau_{Rs} \sim \Phi^{-1/2}$ carrier lifetime variations have been revealed under stopped protons implantation, when τ_{Rs} actually averages carrier lifetime variations within the proton projectile range, and explained by variation of density of the extended radiation defects. The increase of the radiation defect density determines a reduction of distances (L) among the defects, and it leads to the proportionality relations as: $\tau_{Rs} \sim 1/N_{cl} \sim L^2 \sim \Phi^{-1/2}$.
10. Contactless microwave probed photoconductivity and dynamic reflection grating techniques have been combined and approved for the direct measurements of the carrier recombination and transport characteristics in ultra-thin layered structures. Recombination lifetimes from tenths to hundreds of nanoseconds were determined in the SRB layers containing different density of dislocations. A hyperbolic-like excess carrier relaxation within asymptotic carrier decay part has been unveiled in the SRB layers, and this carrier density relaxation behaviour is ascribed to multi-trapping processes characterized by trapping coefficient $K_{tr}>10$, which is attributed to disorder caused by dislocation network. Stochastic carrier transport play important role for carrier diffusion and the value of the lateral carrier diffusion coefficient $D_a \leq 0.13$ cm^2/s is inherent for dislocated structures.
11. Carrier lifetime variations with doping in Ge has been determined at low and elevated excitation levels. It was inferred that this lifetime dependence on doping density can be approximated by S–R–H model in low and moderately doped material, while lifetime decreases linearly with $1/n_{dop}$ for dopant concentrations above $n_{thr} = 4\times10^{16}$ cm^{-3}. This behaviour can be attributed to an increase of the doping technology introduced recombination centres, which density is proportional to the dopants concentration.

12. The experimental arrangement has been proposed and tested in this work of PL spectroscopy and simultaneous measurements of microwave probed photoconductivity transient and time resolved photoluminescence.
13. The excess-carrier decays, revealed in the MW-PC transients of the as-grown GaN material, contain an initial stage with a fast component of a few nanoseconds dependent on the excitation density. The initial instantaneous lifetimes of the MW-PC decays are close to that estimated from the time-resolved photoluminescence signal relaxation rate. The long tail component of carrier density decay is ascribed to excess carrier trapping processes at dislocations, those comprise disordered network within GaN epi-layer.
14. Trapping caused long tail carrier decay component in GaN layers is shortened most significantly with hadrons irradiation fluence and, for large fluence of hadrons irradiation in the range of 10^{16} cm^{-2}, the asymptotic decay component is non-resolvable. This has been explained by the enhancement of the recombination rate within crystalline material with increase of the radiation defects density. The MOCVD as-grown GaN material and the irradiated samples exhibited different values of time-stretching factor equal to 0.7 and 0.3, respectively.

References

[1] J. Robertson, Eur. Phys. J. Appl. Phys. **28** (2004) 265.

[2] J.M. Hartmann et. al., J. Cryst. Growth **274** (2005) 90.

[3] J.-S. Park, et al., Appl. Phys. Lett. **90** (2007) 052113.

[4] E.A. Fitzgerald, and N. Chand, J. Electron. Mater. **20** (1991) 839.

[5] O. Ambacher, J. Phys. D: Appl. Phys. **31** (1998) 2653.

[6] L. Tarnawska, P. Zaumseil, M. A. Schubert, S. Okur, U. Ozgur, H. Morkoc, R. Paszkiewicz, P. Storck, and T. Schroeder, J. Appl. Phys. **111** (2012) 073509.

[7] M. Albrecht, J. L. Weyher, B. Lucznik, I. Grzegory, and S. Porowski, Appl. Phys. Lett. **92** (2008) 231909.

[8] G. Lutz, *Semiconductor radiation detectors* (Springer, 2007).

[9] C. A. Londos, A. Andriakis, V. Emtsev, and H. Ohyama, J. Appl. Phys. **105** (2009) 123508.

[10] H. Yamada, A. Chayahara, Y. Mokuno, N. Tsubouchi, S. Shikata, and N. Fujimori, Diamond&Related Materials **20** (2011) 616.

[11] Z. Li, et al., Nucl. Instr. and Meth. A **583** (2007) 139.

[12] D.V. Lang, J. Appl. Phys. **45** (1974) 3023.

[13] A. Chantre, G. Vincent, and D. Bios, Phys. Rev. B **23** (1981) 5335.

[14] A. Armstrong, A. R. Arehart, and S. A. Ringel, J. Appl. Phys. **97** (2005) 083529.

[15] C.T. Sah, L. Forbes, L.L. Rosier, and A.F. Tasch, Solid-State Electron. **13** (1970) 759.

[16] A.H. Kalma, and J.C. Corelli, Phys. Rev. **173**, No. 3 (1968).

[17] H. Lefevre, and M. Schulz, Appl. Phys. **12** (1977) 45.

[18] I. Pintilie, E. Fretwurst, G. Lindstroem, and J. Stahl, Appl. Phys. Lett. **82** (2003) 2169.

[19] I. Pintilie, C. Tivarus, L. Pintilie, M. Moll, E. Fretwurst, and G. Lindstroem, Nucl. Instr. and Meth. A **476** (2002) 652.

[20] M. Moll, E. Fretwurst, M. Kuhnke, and G. Lindström, Nucl. Instr. and Meth. B **186** (2002) 1.

[21] D.K. Schroder, *Semiconductor Material and Device Characterization* (Wiley, New York, 1998).

[22] Y. Murakami, et. al., J. Appl. Phys. **75** (1994) 3548.

[23] J. Vanhellemont, E. Simoen, and C. Claeys, Appl. Phys. Lett. **66** (1995) 2894.

[24] A. Poyai, E. Simoen, C. Claeys, E. Gaubas, A. Huber, and D. Graf, Material Science Eng. B **102** (2003) 189.

[25] A. Chilingarov, H. Feick, E. Fretwurst, G. Lindström, S. Roe, and T. Schulz, Nucl. Instr. and Meth. A **360** (1995) 1.

[26] E. Gaubas, T. Čeponis, and J. Vaitkus, J. Appl. Phys. **110** (2011) 033719.

[27] P. Blood and J. W. Orton, *The Electrical Characterization of Semiconductors: Majority Carriers and Electron State* (Academic Press, New York, 1992).

[28] D. H. Dickey, The Electrochem. Soc. **12** (1963) 151.

[29] S. Lanyi, and M. Hruskovic, J. Phys. D **36** (2003) 5.

[30] C.C. Williams, Ann. Rev. Mater. Sci. **29** (1999) 471.

[31] L.I. Murin, V.P. Markevich, J.L. Lindstrom, and M. Kleverman, Physica B **340** (2003) 1046.

[32] E.E. Haller, Mat. Res. Soc. Symp. Proc. Vol. **378** (1995) 547.

[33] G. D. Watkins, and J. W. Corbett, Phys. Rev. **138** (1965) A543.

[34] R.H. Bartram, *Structural analysis of point defects in solids* (Springer-Verlag, New York, 1992).

[35] R. Poirier, V. Avalos, S. Dannefaer, F. Schiettekatte, and S. Roorda, Nucl. Instrum. Methods Phys. Res. B **206** (2003) 85.

[36] T. E. M. Staab, M. Haugk, A. Sieck, T. Frauenheim, and H. S. Leipner, Physica B **273** (1999) 501.

[37] G. Davies, S. Hayama, L. Murin et. al., Phys. Rev. B **73** (2006) 165202.

[38] A. G. Tweet, J. Appl. Phys. **30** (1959) 2002.

[39] S. Rein, *Lifetime Spectroscopy* (Springer-Verlag, Berlin, 2005).

[40] V. Akhmetov, G. Kissinger, A. Fischer, G. Morgenstern, G. Ritter, and M. Kittler, J Mater Sci: Mater Electron., **19** (2008) S36.

[41] K. Jarašiunas, T. Malinauskas, K. Neimontas, V. Gudelis, and R. Aleksiejunas, Acta. Phys. Pol. A **110** (2006) 201.

[42] R.K. Jain, and M.B. Kein, *Degenerate four wave mixing in semiconductors* (Acad. Press., New York, 1983).

[43] K. Neimontas, T. Malinauskas, R. Aleksiejunas et. al., Semicond. Sci. Technol. **21** (2006) 952.

[44] M. Sudzius, A. Kadys, K. Jarasiunas, in: Z.G. Wang, Y.H. Chen, X.L. Ye (Eds.), SIMC-XIII Proceedings (2004) 11.

[45] M. Sheik-Bahae, et. al., Opt. Eng. **30** (1990) 1228.

[46] B. Grundig-Wendrock, M. Jurisch, and J.R. Niklas, Mater, Sci. Eng. B **91** (2002) 371.

[47] M.B. Vinogradova, O.V. Rudenko, and A.P. Sukhorukov, *Teorija voln* (Moskva, Nauka, 1979).

[48] E. Gaubas, Lith. J. Phys. **43** (2003) 145.

[49] T. Oteradian, Solid-State Electron. **36** (1993) 153.

[50] M. Kunst, and G. Beck, J. Appl. Phys. **60** (1986) 3558.

[51] E. Gaubas, and A. Kaniava, RSI, **67**(6) (1996) 2339.

[52] M. Kunst, and G. Beck, J. Appl. Phys. **63**(4) (1988) 1093.

[53] S.M. Anlage, V.V. Talanov, and A.R. Schwartz, in *Scanning Probe Microscopy: Electrical and Electromechanical Phenomena at the Nanoscale*, S. Kalinin, and A. Gruverman, Eds. (New York: Springer Sci., 2007).

[54] M. Tabib-Azar and D. Akinwande, Rev. Sci. Instrum. **71** (2000) 1460.

[55] M. Tabib-Azar, D. Akinwande, G. E. Ponchak, and S. R. LeClair, Rev. Sci. Instrum. **70** (1999) 3083.

[56] S. V. Kalinin, A. Gruverman, *Scanning Probe Microscopy of Functional Materials* (Springer, New York, 2011).

[57] W. Shockley and W.T. Read, Phys. Rev. **87** (1952) 835.

[58] P.T. Landsberg, *Recombination in semiconductors* (Cambridge University Press, 1991).

[59] J.S. Blakemore, *Semiconductor statistics* (Pergamon Press, Oxford, 1962).

[60] E. Gaubas, *Recombination processes amd light – induced gradiental phenomena in silicon and III-V group compounds*, Habilitation thesis (Vilnius, 2002).

[61] E. Gaubas and J. Vanhellemont, J. Appl. Phys. **80** (1996) 6293.

[62] E. Gaubas, J. Vaitkus, E. Simoen, C. Claeys, J. Vanhellemont, Mat. Sci. Semicond. Proc. **4** (2001) 1.

[63] B-03026 Report No. B-08 „Jonizuojanciai radiacijai jautrių ir atsparių medžiagų tyrimas ir defektu modifikavimas“.

[64] G. Lucovsky, Solid State Commun. **3** (1965) 299.

[65] A.A. Kopylov, and A.N. Pikhtin, Sov. Phys. Semicond. **10** (1976) 7.

[66] K. Huang, and A. Rhys, Proc. RSA **204** (1950) 406.

[67] A. Dargys, J. Kundrotas, *Handbook on physical properties of Ge, Si, GaAs and InP* (Science and Encyclopedia Publishers, Vilnius, 1994).

[68] Presentations of B. Svensson and I. Pintilie at rd50/WODEAN workshop, see http://wwwiexp.desy.de/seminare/defect.analysis.workshop.august.2006.html.

[69] E. Gaubas, J. Vanhellemont, E. Simoen, I. Romandic, W. Geens and P. Clauws. Physica B **401** (2007) 222.

[70] S. Forment, J. Vanhellemont, P. Clauws, J. Van Steenbergen, S. Sioncke, M. Meuris, et al., Mater. Sci. Semicond. Process. **9** (2006) 559.

[71] P. Clauws, E. Simoen, Mater. Sci. Semicond. Process. **9** (2006) 546.

[72] E. Simoen, C. Claeys, S. Sioncke, J. Van Steenbergen, M. Meuris, S. Forment, J. Vanhellemont, P. Clauws and A. Theuwis, J. Mater. Sci. Mater. Electron. **18** (2007) 799.

[73] S.T. Pantelides, Rev. Mod. Phys. **50** (1978) 797.

[74] H. Goto, Y. Adachi, T. Ikoma, Phys. Rev. B **22** (1980) 782.

[75] C. Claeys, E. Simoen, *Radiation Effects in Advanced Semiconductor Materials and Device* (Springer, Berlin, 2002).

[76] M. Huhtinen, Nucl. Instr. and Meth. A **491** (2002) 194.

[77] R.M. Fleming, C.H. Seager, D.V. Lang, P.J. Cooper, E. Bielejec, J.M. Campbell, J. Appl. Phys. **102** (2007) 043711.

[78] P.F. Ermolov, D.E. Karmanov, A.K. Leflat, V.M. Manankov, M.M. Merkin, E.K. Shabalina, Semiconductors **36** (2002) 1114.

[79] G. Davies, S. Hayama, L. Murin, R. Krause-Rehberg, V. Bondarenko, A. Sengupta, C. Davia, and A. Karpenko, Phys. Rev. B **73** (2006) 165202.

[80] B. MacEvoy, and G. Hall, Mater. Sci. Semicond. Process. **3** (2000) 243.

[81] L. Pavesi, J. Appl. Phys. **80** (1996) 216.

[82] http://www.srim.org/.

[83] E. Gaubas, T. Ceponis, A. Uleckas, J. Vaitkus, and J. Raisanen, Nucl. Instrum. Methods A **612** (2010) 559.

[84] E. Gaubas, J. Vaitkus, E. Simoen, C. Claeys, and J. Vanhellemont, Mater. Sci. Semicond. Processing **4** (2001) 125.

[85] Ю.Вайткус, Э.Гаубас, А.Рудайтис, Светонаведенные отражательные . дифракционные решетки на поверхности кремния. Лит.Физ.Сборн., т.29, в.5 (1989) 578.

[86] G Eneman, E Simoen, R Delhougne, et al. J. Phys.: Condens. Matter. **17** (2005) 1.

[87] W. Van Den Daele, C. Le Royer, E. Augendre, J. Mitard, G. Ghibaudo, S. Cristoloveanu, Solid-State Electron. **59** (2011) 25.

[88] H.F. Mataré, *Defect Electronics in Semiconductors* (Wiley-Interscience, New York, 1971).

[89] K. Jarasiunas, J. Vaitkus, E. Gaubas, L. Jonikas, R. Pranaitis, and L. Subacius, IEEE J. Quant. Electron. **22** (1986) 1298.

[90] D. Poelman, P. Clauws and B. Depuydt, Solar Energy Mat. and Solar Cells **76** (2003) 167.

[91] E. Gaubas and J. Vanhellemont, Appl. Phys. Lett. **89** (2006) 142106.

[92] D.H. Auston, C.V. Shank and P. LeFur, Phys. Rev. Let. **35** (1975) 1022.

[93] A.L. Smirl, S.C. Moss and J.R. Lindle, Phys. Rev. B **25** (1982) 2645.

[94] G. Nilsson, Physica Scripta **8** (1973) 165.

[95] S.G. Kalashnikov, J. Phys. Chem. Solids **8** (1959) 52.

[96] I.V. Karpova and S.G. Kalashnikov, in Proc. Int. Conf. Phys. Semicond., Exeter, (1962) 880.

[97] R. Conradt and J. Aengenheister, Solid State Commun. **10** (1972) 321.

[98] R.N. Hall, Phys. Rev. **87** (1952) 387.

[99] S.M. Sze, J.C. Irvin, Solid-State Electron. **11** (1968) 599.

[100] S.M. Ryvkin, *Photoelectronic effects in semiconductors* (Consulting Bureau, New York, 1964).

[101] J. Vanhellemont, J. Chen, W. Xu, D. Yang, J. M. Rafí, H. Ohyama, and E. Simoen, J. Cryst. Growth **317** (2011) 8.

[102] J.M. Rafi, J. Vanhellemont, E. Simoen, J. Chen, M. Zabala, F. Campabadal, Physica B **404** (2009) 4723.

[103] C.A. Londos, A. Andrianakis, V.V. Emtsev, H. Ohyama, Semicond. Sci. Technol. **24** (2009) 075002.

[104] J. Vanhellemont, J. Chen, J. Lauwaert, H. Vrielinck, W. Xu, D. Yang, J.M. Rafı´, H. Ohyama, E. Simoen, J. Cryst. Growth **317** (2011) 8.

[104] M. Albrecht, H.P. Strunk, J.L. Weyher, I. Grezgory, S. Porowski, and T. Wosinski, J. Appl. Phys. **92** (2002) 2000.

[105] E. Gaubas, S. Juršėnas, S. Miasojedovas, J. Vaitkus, A. Žukauskas, J. Appl. Phys. **96** (2004) 4326.

[106] E. Gaubas, K. Kazlauskas, R. Tomašiūnas, J. Vaitkus, A. Žukauskas, Appl. Phys. Lett. **84** (2004) 5258.

[107] J. Vaitkus, W. Cunningham, E. Gaubas, M. Rahman, S. Sakai, K.M. Smith, T. Wang, Nucl. Instr. and Meth. A **509** (2003) 60.

[108] M.A. Reshchikov, and H. Morkoc, J.Appl. Phys. **97** (2005) 061301.

[109] G. Pfister, H. Sher, Adv. Phys. **27** (1978) 747.

[110] S. Havlin and D. Ben-Avraham, Adv. Phys. **51** (2002) 187.